A Pulsed NMR Study of ^{3}He Adsorbed on Bare and ^{4}He Preplated MCM-41 using DC SQUID Detection

by

Ben Yager

A thesis submitted for the degree of
Doctor of Philosophy

Royal Holloway, University of London
2010

Declaration of Authorship

I Ben Yager hereby declare that this thesis and the work presented in it is entirely my own. Where I have consulted the work of others, this is always clearly stated.

Signature:. . . . . .

Date: . . . . . .

Abstract

This thesis describes two low field NMR and vapour pressure experiments of helium adsorbed in the pores of the mesoporous powder substrate MCM-41 at temperatures down to 1.5 K. A sensitive broadband DC SQUID based spectrometer was developed to facilitate these measurements with a coupled energy sensitivity of 30 h at 1.5 K. NMR relaxation times T_1 and T_2^* were measured as a function of temperature for frequencies from 80 to 240 kHz.

MCM-41 is an amorphous silica formed of a hexagonal array of straight regular pores. For our sample the pore diameter is 2.3 nm and length is ~ 300 nm, equal to the grain size. The substrate was characterised by ^{4}He vapour pressure isotherms performed using an in-situ pressure gauge with a resolution of 1 μbar. Layer completion and full pores were determined from the isothermal compressibility of the adsorbed film.

In the first NMR experiment ^{3}He was adsorbed onto the bare pore walls of MCM-41 from coverages approaching monolayer completion up to full pores. The adsorbed helium was found to form a 2D film which exhibited significant motional narrowing of the NMR line at low temperatures due to quantum tunnelling.

In the second experiment the substrate was initially preplated with just over a monolayer of ^{4}He before a low ^{3}He coverage of 0.01 monolayer was added. Subsequently the preplating coverage was varied whilst the ^{3}He coverage was held constant at 0.02 monolayer. Under these stringent conditions a transition to a quasi-1D state is expected to occur at temperatures below 100 mK where Luttinger liquid behaviour is predicted. Nuclear magnetic resonance is a powerful tool for probing the necessary dynamic and magnetic properties of systems to determine the Luttinger liquid parameters.

The ^{3}He in this helium mixtures experiment was also found to behave as a 2D film, where at these low coverages the relaxation times were independent of the ^{3}He

density. A correlation was found between the relaxation times and the isothermal compressibility of the film.

The results of the NMR experiments have been used to make proposals on the design and fabrication of a new experiment with a coolable cell capable of reaching temperatures low enough to observe a transition to 1D. Cooling this substrate to temperatures far below 1 K is not trivial and low resonant frequencies are required to avoid excessively heating the sample during NMR pulsing.

Contents

List of Figures

List of Tables

Chapter 1

Introduction

1D systems are an area of current interest. Recent advances in technology and experimental techniques have meant that over the past few decades one-dimensional (1D) systems have changed from purely theoretical systems to realisable systems with important "real life" applications. There are a variety of different systems which have been realised experimentally including cold atoms confined in optical lattices [1], edge states in a two-dimensional electron gas [2], tunneling between long ballistic wires in GaAs/AlGaAs heterostructures [3] and ^{3}He adsorbed in nanotubes [4, 5].

The group of N. Wada at Nagoya University have published a number of papers [4–11] regarding $^3\mathrm{He} - ^4$ He mixture systems adsorbed in FSM-16 nanopores of different diameters. FMS-16 is structurally similar to the MCM-41 substrate used in this work and a number of comparisons are made between the results of Wada and the work outlined in this thesis. Their measurements are by the complimentary methods of pressure, heat capacity measurements and torsional oscillator experi-

ments. They have found that a superfluid ^{4}He film can form inside the nanopores, and the superfluid transition is observable in the pressure and oscillator results.

An apparent 1D system by Wada et al was created by preplating a substrate with a 28 Å pore size with a 4.9 Å (1.47 monolayer) superfluid ^{4}He film. In this system 3.5×10^{-3} monolayers of ^{3}He gave a 1D interparticle spacing of 33 Å. The heat capacity results at low temperatures are consistent with 1D motion, and a Schottky peak is observed on warming indicating a dimensional crossover from 1D to the 2D state. At higher temperatures the heat capacity is consistent with a 2D film. We would like to perform a similar experiment using NMR as the experimental probe, however for this there are additional challenges in cooling the sample to the required temperatures.

This thesis describes the characterisation of a system of helium adsorbed in the mesopores of MCM-41 zeolite. It is intended to facilitate the design of a future experiment capable of obtaining lower temperatures whilst developing a range of experimental techniques.

In chapter 2 the MCM-41 substrate is described and the energetics and stringent constraints for creating a 1D system are explained. In particular a low spin density ~ 0.01 monolayer is necessary to observe a dimensional crossover from 2D to 1D.

Chapters 4 and 5 describe the design and construction of the instrumentation used to perform the experiments. This includes a low temperature pressure gauge with a resolution of 1.2 μbar, which was used to characterise the system through thermodynamic measurements, and a low field NMR spectrometer with DC SQUID detection which was used to provide information on the dynamics of the system.

The results of the vapour pressure measurements are presented in chapter 6. A summary of the initial sample characterisation measurements by Chan and Bharat is given with explanations of the methods used to calculate the various parameters. These are used to make comparisons between our measurements and those of Wada's group. The experimental technique was improved throughout this work, as explained in this section, resulting in an improved characterisation and a method which can be carried forward to future experiments.

The NMR results for the pure ^{3}He and the ^{3}He-^{4}He mixtures experiments are presented in chapter 7. The evolution of the experimental technique is explained, where new noise sources became important as the number of spins was reduced. Relaxation times and magnetisation were measured as a function of temperature, frequency and coverage.

A summary of the achievements from the work in this thesis is given in chapter 8. A design concept for a future experimental cell is given with consideration to the signal-to-noise, given the results of chapter 7.

Chapter 2

System

2.1 Introduction

In this section the experimental motivation for the experiment will be outlined. The structure and fabrication of the substrate will be discussed briefly and the conditions which are expected to cause a dimensional crossover to a 1D system are explained.

2.2 MCM-41 Substrate

The experimental substrate is a *Mobil Composition of Matter* (MCM-41) powder as described in [12, 13]. This inorganic structure is amorphous silica possessing long range order and is formed by a liquid crystal templating mechanism where surfactant molecules act as templates. The resultant structure is a mesoporous molecular sieve formed of a uniform array of straight hexagonal pores.

The surfactants are self aligning amphiphiles, long molecules which have a hydrophilic head and hydrophobic tail, such as $C_{\mathrm{n}}H_{2\mathrm{n}+1}(CH_3)N^+$ $(n = 8 - 22)$. The pore diameter is essentially determined by n such that samples are commonly referred to as $C8$ for $n = 8$ etc, although this can be modified by altering the fabrication procedure.

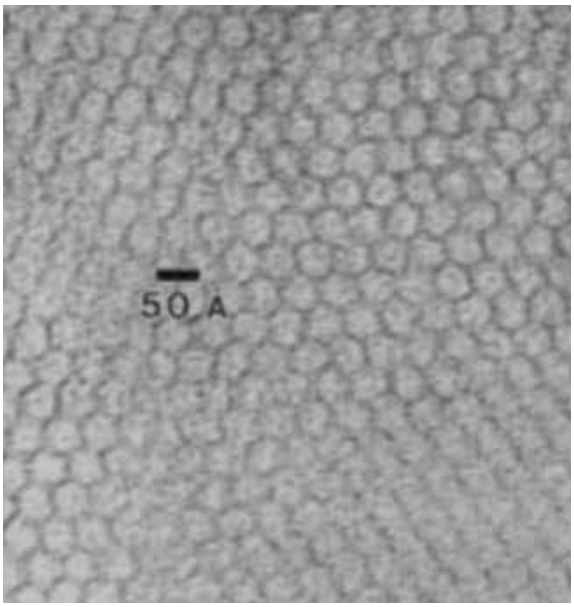

Figure 2.1: A TEM image of MCM-41 taken from [13]

The length of the resultant pores are equal to the grain size $\sim 3000\,\text{Å}$. The pore diameter is tunable between 16 Å and 100 Å during fabrication covering the microporous ($< 20\,\text{Å}$) and mesoporous (20-500 Å) ranges as defined in [14]. Two MCM-41 samples were available for this experiment fabricated by B.L. Newalker of Pennsylvania State University labelled BC1 and BC2. The initial characterisation of these two samples in section 6.2 shows the pore diameters of the substrates to be $(23 \pm 1)\,\text{Å}$ and $\sim$27 Å. The better characterised BC1 substrate with the smaller pore diameter was chosen for this experiment.

2.3 Creating a 1D Quantum System

The ultimate aim of this experiment is to create a 1-dimensional (1D) quantum system consisting of interacting ^{3}He fermions inside the bore of the mesopores. A dimensional cross-over to 1D should occur when the energy levels for two of the three degrees of motional freedom are restricted to the quantum ground state. The approximate cylindrical symmetry of this system makes it is appropriate to consider the energy levels associated with the radial (ρ), azimuthal (ϕ) and axial (z) motion within the pores. Due to the high aspect ratio of the pores there is a separation of energy scales between the axial excitation energies and the radial and azimuthal excitation energies. At low enough temperatures it should be possible to freeze out the radial and azimuthal excitations restricting them to the quantum ground state, while the axial energy levels of the ^{3}He atoms will be quasi-continuous.

2.3.1 Quantum States

The full numerical energy level solutions to the Schrödinger equation have not been calculated explicitly in this work as they have been obtained previously by the group of N. Wada for a similar system. The results of that calculation are described in section 2.4 and the resultant energy levels shown in figure 2.4. In this section the appropriate form of the Schrödinger equation is given, with an explanation of the effects of preplating the pores with ^{4}He. It is illustrative to consider some approximate methods of determining the energy levels shown in figure 2.4 and considering the extreme cases of no preplating and for a thick preplating film.

To determine the energy levels of the ^{3}He atoms in the pore we consider the time-

independent Schrödinger equation $\hat{H}\Psi = E\Psi$, where the Hamiltonian operator $\hat{H}$ is given by

$$\hat{H} = \frac{-\hbar^2}{2m_3}\nabla^2 + V \tag{2.1}$$

The symmetry of the pores means that it is appropriate to use cylindrical polar coordinates, where the Laplacian operator can be expressed as

$$\nabla^2 = \frac{1}{\rho}\frac{\partial}{\partial\rho}\left(\rho\frac{\partial}{\partial\rho}\right) + \frac{1}{\rho^2}\frac{\partial^2}{\partial\phi^2} + \frac{\partial^2}{\partial z^2} \tag{2.2}$$

leading to the eigenfunctions of Stan and Cole [15] in the form

$$\psi_{lkm} = f_{lm}(\rho)e^{ikz}e^{im\phi} \tag{2.3}$$

where the radial quantum numbers ($l = 1, 2, \ldots$) and azimuthal quantum numbers ($m = 0, \pm1, \ldots$) are discrete and the axial quantum numbers k are quasi-continuous. As the potential inside the pore is purely a function of the radial distance from the wall it is immediately clear from the form of equation 2.2 that the Schrödinger equation is separable into an axial component and the radial and azimuthal components. The energy eigenvalues are then given by $E_{lkm} = E_{lm} + \hbar^2k^2/2m$ and from Stan and Cole the radial function, $f_{lm}(\rho)$, obeys the equation

$$\frac{d^2f}{d\rho^2} + \frac{1}{\rho}\frac{df}{d\rho} + \left\{\frac{2m_3}{\hbar^2}[E_{lm} - V(\rho) - \frac{m^2}{\rho^2}\right\} f = 0 \tag{2.4}$$

The potential inside the pores is due to the van der Waals potential between the substrate atoms and adatoms. Therefore the description of the potential is simplified by a change of variable to $r = R - \rho$, shown in figure 2.3. For large pores the substrate potential can be modelled as a Leonard-Jones 6-12 potential between the substrate

atoms and adatoms, where the power dependence is for a flat substrate. Integrating over a homogeneous, semi-infinite substrate leads to a potential of the form

$$V_{3-9}(r) = \frac{3\sqrt{3}}{2}\epsilon\left[\left(\frac{\sigma}{r}\right)^9 - \left(\frac{\sigma}{r}\right)^3\right] \tag{2.5}$$

where ϵ is the depth of the potential well and σ is the finite distance at which the potential by the adatoms due to the substrate is zero. In a semiclassical description of the system this is equal to the hard-core radius of the adatom. The radial position of potential minimum is at $a = 3^{1/6}\sigma \approx 1.20\sigma$. As $(3^{1/6})^9 = 3\sqrt{3}$ and $(3^{1/6})^3 = \sqrt{3}$, equation 2.5 can be rewritten as

$$V_{3-9}(r) = \frac{\epsilon}{2}\left[\left(\frac{a}{r}\right)^9 - 3\left(\frac{a}{r}\right)^3\right] \tag{2.6}$$

For this potential we adopt the adsorption coefficients $\epsilon = 100\,\mathrm{K}$ and $a = 2.05\,\text{Å}$ of M. Boninsegni [16]. For a flat structureless substrate this is equivalent to the adatoms having hard core radius of 1.71 Å.

For distances $r > a$ we can assume the simplified potential as Cheng and Cole [17]

$$V(r) = -\frac{\Gamma}{r^3} \tag{2.7}$$

where $\Gamma = 1100\,\mathrm{K\,Å}^3$, the value for glass, is used for the energy level calculations [5] in section 2.4. The equivalent value for the Boninsegni coefficients is $\Gamma = 1292\,\mathrm{K\,Å}^3$. For small pores it is necessary to consider the curvature of the pore. A model where the potential inside a carbon nanotube is given as the summation of the pair interactions between individual substrate atoms and the adatoms has been proposed by Stan and Cole [15]. The potential contribution due to adatoms in neighbouring

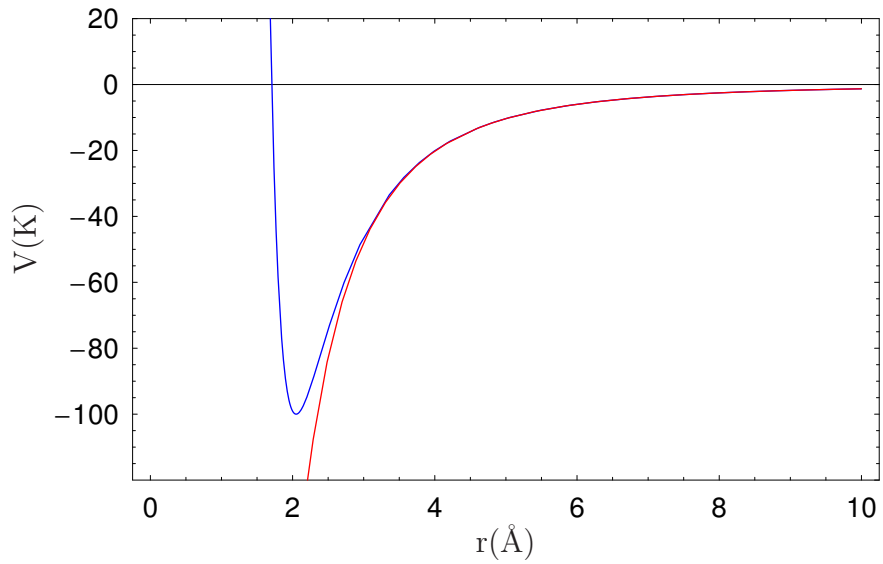

Figure 2.2: Adatom-Substrate binding potentials for (blue) 3-9 Lennard-Jones potential and (red)r^{-3} potential valid for $r > a$.

pores may also contribute to the potential as the pore walls are thin when compared with the pore diameter.

2.3.2 Effect of Preplating

The binding potential between the substrate and the ^{3}He adatom can be decreased by preplating the substrate with an inert film of thickness, δ, which has a weaker van der Waals interaction. This also has the effect of decreasing the effective pore diameter, making the pores more one-dimensional.

For coverages above monolayer the dominant interaction potential is that between the preplating atoms and the adatoms. Using equation 2.7 the combined potential from the underlying substrate and the preplating can be approximated as

$$V(r) = \frac{\Gamma_{\mathrm{He}}}{(r-\delta)^3} + \frac{\Gamma_{\mathrm{sub}} - \Gamma_{\mathrm{He}}}{r^3} \tag{2.8}$$

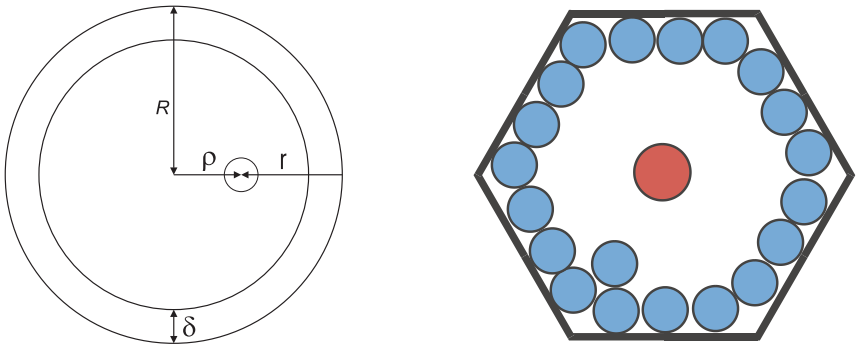

(a) (b)

Figure 2.3: (a) Reduced pore dimensions. R is the bare pore radius, ρ is the radial distance to the ^{3}He adatom, $r = R - \rho$ is the radial distance between ^{3}He adatom and substrate and δ is the ^{4}He preplating thickness. (b) A representation of ^{3}He atoms (red) in the ^{4}He preplated (blue) pores of MCM-41.

where Γ_{He} and Γ_{sub} relate to the attractive part of the van der Waals binding potential due to the ^{4}He preplating and substrate respectively. Here the substrate can be considered infinite as the contribution from atoms far from the surface is small.

2.4 Wada Energy Levels

The group of N. Wada have been working on the similar system of helium adsorbed in the mesopores of FSM-16, which is structurally similar to MCM-41. They have calculated the difference in energy between the ground state and first excited radial and azimuthal states for a range of pore diameters including 22 Å pores which are similar to our system. Details of this numerical calculation are given in reference [5].

Using the notation of Wada the total energy of a particle in the pore is given by $E_{klm} = E_{lm} + \hbar^2 k^2 / 2m_3$ where l and m are the number of nodes in the radial and azimuthal wavefunctions respectively. The energy gap from the ground state to state lm is given by $\Delta_{\mathrm{lm}} = \mathrm{E_{lm}} - \mathrm{E_{00}}$ where E_{00} is the ground state. In figure 2.4,

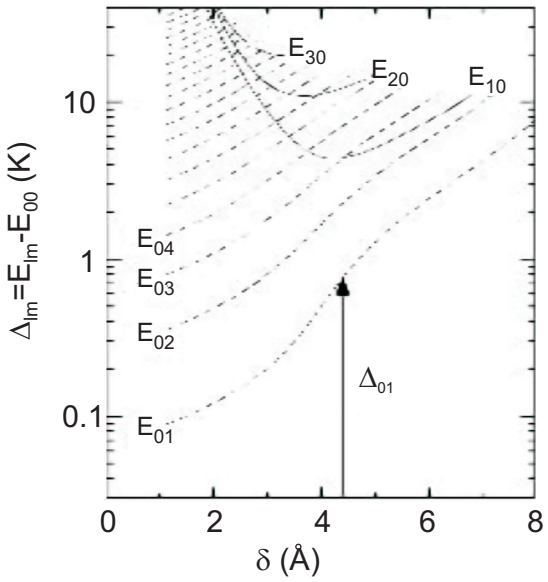

Figure 2.4: Azimuthal, E_{0m}, and radial, E_{l0}, energy levels of ^{3}He in the 22 Å diameter pores, as a function of film thickness, δ.

taken from reference [5], we see that the smallest energy gap is to the first excited azimuthal state $E_{01} - E_{00} = \Delta_{01}$. The energy gap increases monotonically with the film thickness δ and the general 1D condition is satisfied when

$$T + T_{\mathrm{F}}^{(1\mathrm{D})} \ll \Delta_{01}/k_{\mathrm{B}} \tag{2.9}$$

where $T_{\mathrm{F}}^{(1\mathrm{D})}$ is the one-dimensional Fermi temperature. This means that a cross-over to a 1D state is expected to occur at temperatures significantly below 1 K. $T_{\mathrm{F}}^{(1\mathrm{D})}$ is calculated in section 2.5.

The energy gap to the first radially excited state, Δ_{10}, initially decreases with increasing δ. For thicker preplating coverages, slightly above monolayer preplating thickness, Δ_{10} begins to increase with increasing δ. Approximations to the energy levels in the limiting cases of no preplating and thick preplating films are calculated in the following sections, 2.4.1 and 2.4.2.

2.4.1 Thin Films

For thin films ($\delta \to 0$) the azimuthal energy levels have the lowest excitation energy gaps, and as $\rho \to R$ the excitation energies approach [4, 5]

$$E_{0n} = \frac{\hbar^2}{2m_3}\left(\frac{n}{\rho}\right)^2 \tag{2.10}$$

where n is the number of nodes in the azimuthal wave function. This result is similar to that for the model system of a particle confined to a ring, where ρ is considered a constant. In that case the Schrödinger equation reduces to

$$\frac{-\hbar^2}{2m_3}\frac{1}{\rho^2}\frac{\partial^2}{\partial\phi^2}\Phi(\phi) = E\Phi(\phi) \tag{2.11}$$

Here the potential for constant ρ is also constant and, as we are interested in the energy gap, this is ignored. The solutions are of the form

$$\Phi(\phi) = e^{im\phi} \tag{2.12}$$

where

$$m^2 = \frac{2m_3\rho^2 E}{\hbar^2} \tag{2.13}$$

where $m = 0, \pm1, \pm2, \ldots$ to ensure that the wavefunction is single valued.

For our 23 Å pores the position of the minimum of the radial potential in equation 2.5 of 2.05 Å gives a value $\rho = 9.45$ Å. Therefore for $\delta = 0$ we find $\Delta_{01} = 9$ mK which is in agreement with the energy levels in figure 2.4.

2.4.2 Infinite Cylinder

As the preplating thickness increases the contribution to the potential from the MCM-41 substrate becomes negligible. The potential will be dominated by the ^{4}He preplating, where the potential is small compared with the energy due to confinement. In the case the problem is reduced to that of a particle in an infinite cylinder and can be described by the Schrödinger equation

$$-\frac{\hbar^2}{2m_3}\left(\frac{\partial^2}{\partial\rho^2}+\frac{1}{\rho}\frac{\partial}{\partial r}+\frac{1}{\rho^2}\frac{\partial^2}{\partial\phi^2}+\frac{\partial^2}{\partial z^2}\right)\Psi\left(\rho,\phi,z\right)=E\Psi\left(\rho,\phi,z\right) \tag{2.14}$$

Which is separable into radial, azimuthal and axial components where $\Psi(\rho,\phi,z) = R\left(\rho\right)\Phi\left(\phi\right)Z\left(z\right)$, so that

$$\left[\frac{1}{R}\frac{d^2R}{d\rho^2}+\frac{1}{\rho R}\frac{dR}{d\rho}+\frac{1}{\rho^2}\frac{1}{\Phi}\frac{d^2\Phi}{d\phi^2}+\frac{1}{Z}\frac{d^2Z}{dz^2}\right]=-\frac{2m_3E}{\hbar^2} \tag{2.15}$$

Putting

$$\frac{1}{\Phi}\frac{d^2\Phi}{d\phi^2}=-m^2 \qquad\qquad \frac{1}{Z}\frac{d^2Z}{dz^2}=k_{\mathrm{z}}^2$$

where $\Phi = \exp[im\phi]$ $(m = 0, \pm1, \ldots)$ and $Z = \exp[ik_{\mathrm{z}}z]$ $(k_{\mathrm{z}} = \pm1, \pm2, \ldots)$ and making the substitution

$$E=\frac{\hbar^2}{2m_3}\left(\kappa^2+k_{\mathrm{z}}^2\right)$$

where $E_{lm} = \hbar^2\kappa^2/2m_3$ gives Bessel's equation

$$\rho^2\frac{d^2R}{d\rho^2}+\rho\frac{dR}{d\rho}+\left(\kappa^2\rho^2-m^2\right)R=0 \tag{2.16}$$

which has solutions $R(\rho) = C_1J_m(\kappa\rho) + C_2Y_m(\kappa\rho)$ where J_m and Y_m are ordinary Bessel functions of the first and second kind respectively. $C_2 = 0$ as the solution

to the Schrödinger equation are required to be finite over all space and Y_m has a singularity at $\rho = 0$, so that the allowed solutions are of the form

$$R(\rho) = J_m(\kappa\rho) \tag{2.17}$$

The wavefunction must also be continuous over all space, requiring that it goes to zero at the wall, where $\rho = a$, so that we must have

$$\kappa a = j_{mn} \tag{2.18}$$

here j_{mn} is the n^{th} zero of $J_m(ka)$ and the lowest energy state has $m = 0$ and $n = 1$. Since the $n = 1$ state has no nodes this is equivalent to $l = 0$ in Wada's notation, so that the ground state energy in the cylinder is

$$E_{00} = \frac{\hbar^2}{2m_3}\left(\frac{j_{01}}{a}\right)^2 \tag{2.19}$$

For a preplating thickness of 8 Å this gives an energy gap from the ground state to the first excited state of $\Delta_{01} = 7.94\,\text{K}$ which is in agreement with the energies calculated by Wada shown in figure 2.4.

Table 2.1: Table showing j_{mn}, the n^{th} zero of the $J_m(\kappa\rho)$

j_{mn}	j_{0n}	j_{1n}	j_{2n}	j_{3n}
j_{m1}	2.405	5.520	8.654	11.7915
j_{m2}	3.832	7.016	10.17	13.32
j_{m3}	5.136	8.417	11.62	14.79
j_{m4}	6.380	9.761	13.02	16.22
j_{m5}	7.588	11.07	14.37	17.62

2.5 Fermi Energy in 1D

To create a 1D system we must satisfy $T + T_{\mathrm{F}}^{(1\mathrm{D})} \ll \Delta_{01}/k_{\mathrm{B}}$, equation 2.9. In 1D the Fermi temperature for free particles of mass m obeying the dispersion relation $E_{\mathrm{z}} = \hbar^2 k^2/2m$ is given by

$$T_{\mathrm{F}}^{(1\mathrm{D})} = \frac{\hbar^2}{2m}\left(\frac{\pi n_{1\mathrm{D}}}{2}\right)^2 \tag{2.20}$$

The 1D line density is given by $n_{1\mathrm{D}} = 2\pi RN/S$, where R is the pore radius N is the number of fermion adatoms and S is the adsorption surface area. It is convenient to describe the total adsorption number density as a fraction of the monolayer completion number density, $N/S = X_3 n_1$, where X_3 is the fractional monolayer coverage and n_1 is the number density at monolayer completion.

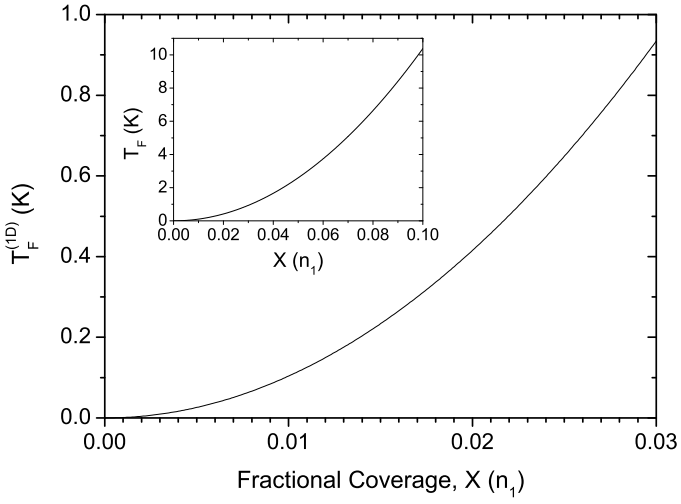

Figure 2.5: 1D Fermi Temperature as a function of ^{3}He coverage

The Fermi energy as a function of ^{3}He coverage is given in figure 2.5, which shows that very low ^{3}He coverages are necessary to achieve a sufficiently low $T_{\mathrm{F}}^{(1\mathrm{D})}$. Figure 2.4 shows that for a preplating thickness of 4.4 Å the energy gap to the first excited azimuthal state is $\Delta_{01} \approx 1\,\mathrm{K}$. In order for the energy of the system to be

significantly below this we would like $T + T_{\mathrm{F}}^{(1\mathrm{D})} \leq 100\,\mathrm{mK}$. This means that for a future experiment with an achievable base temperature of 50 mK we would like $T_{\mathrm{F}}^{(1\mathrm{D})} \leq 50\,\mathrm{mK}$ which is equivalent to $X_3 = 0.007$.

A further constraint is that the 1D interparticle spacing $d_{1\mathrm{D}} = 1/n_{1\mathrm{D}}$ must be greater than the hard core radius of the ^{3}He atoms. Figure 2.6 shows that in order to satisfy this criterion the maximum ^{3}He coverage is $\sim 0.03\,\mathrm{n}_1$, however at this coverage $T_{\mathrm{F}}^{(1\mathrm{d})} \sim \Delta_{01}$.

Quantum effects become important when the thermal de Broglie wavelength, $\Lambda_{\mathrm{T}} = [h^2/2\pi m_3 k_{\mathrm{b}} T]^{1/2} > d_{1\mathrm{D}}$. The de Broglie wavelengths corresponding to significant temperatures are marked on figure 2.6. We note that for $T = 190\,\mathrm{mK}$, $\Lambda_{\mathrm{T}} = 23\,\text{Å}$, which is the bare pore diameter. For monolayer preplating the ^{4}He film thickness is $\delta > 3.5\,\text{Å}$ which reduces the effective pore diameter to 16 Å, where $\Lambda_{\mathrm{T}} = 16\,\text{Å}$ for $T = 395\,\mathrm{mK}$.

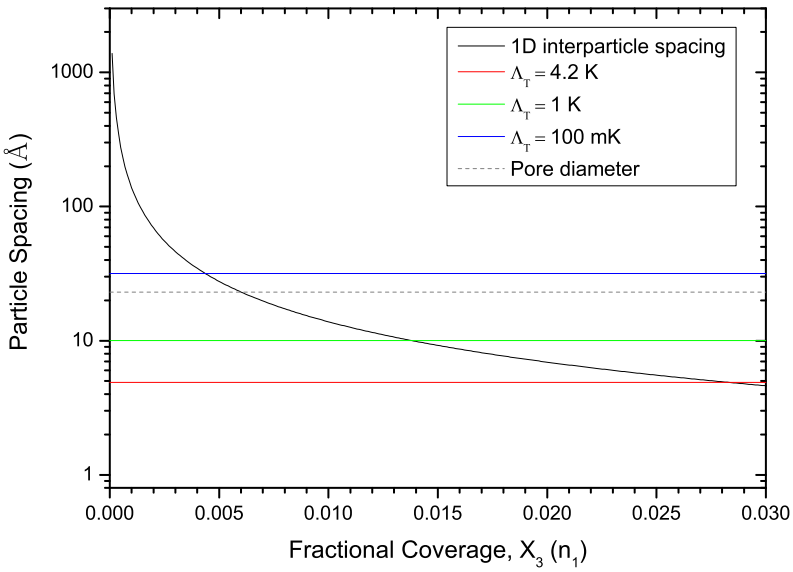

Figure 2.6: 1D interparticle spacing of ^{3}He atoms as a function coverage.

Chapter 3

Nuclear Magnetic Resonance and Relaxation

NMR is a powerful tool in the study of nuclear magnetism and spin dynamics of equilibrium systems. A brief overview of the principles of NMR relevant to this thesis is presented here. For a more complete description of the topic see for example [18–20].

3.1 Principles of Nuclear Magnetic Resonance

Many nuclear species have a non-zero intrinsic nuclear spin angular momentum, $\mathbf{S}$, and a spin quantum number, I, where the magnitude of $\mathbf{S}$ is quantised as

$$S^2 = I(I+1)\hbar^2 \tag{3.1}$$

and I is quantised in integer or half-integer values. The spin is associated with a collinear magnetic dipole moment

$$\boldsymbol{\mu}_{\mathrm{s}} = \gamma\hbar\mathbf{S} \tag{3.2}$$

where the constant of proportionality, γ, is the gyromagnetic ratio.

Dilute systems of nuclear spins are paramagnetic and it is the behaviour of spins in a magnetic field that we are interested in. We define a magnetic field $\mathbf{B} = B_0\hat{\mathbf{k}}$ where in Cartesian coordinates $\hat{\mathbf{k}}$ represents the unit vector in the z-direction. A spin interacting with this field will align itself such that the z-component takes on quantised values $S_{\mathrm{z}} = m\hbar$ where m goes from $+I$ to $-I$ in steps of unity. The Zeeman energy associated with a dipole in a magnetic field is given by

$$E_m = -\boldsymbol{\mu} \cdot \mathbf{B} = -\gamma m\hbar B_0 \tag{3.3}$$

which leads to an energy level splitting

$$\Delta E = \gamma\hbar B_0 \tag{3.4}$$

And hence a resonant transition between adjacent states can be driven if the frequency of radiation is

$$\omega_0 = \gamma B_0 \tag{3.5}$$

where ω_0 is the Larmor frequency.

3.2 Larmor Precession

A nuclear spin angular momentum of the form $\hat{\mathbf{S}}$ will necessarily have a component in the plane orthogonal to $\mathbf{B}$, and so will experience a torque, τ, given by

$$\tau = \mu_s \times \mathbf{B} = \hbar \dot{\mathbf{S}} \tag{3.6}$$

Substituting for $\mathbf{S}$ using 3.2 gives

$$\dot{\mu}_s = \gamma \mu_s \times \mathbf{B} \tag{3.7}$$

The spins precess about $\mathbf{B}$ with angular frequency ω_0, however as there is no energetically preferable direction the phase of the precession is random.

3.2.1 Rotating Frame and Effective Field

The further mathematics of the spin dynamics is simplified with no loss of generality by changing the frame of reference from the lab frame to one which rotates about the z-axis with angular frequency ω. In such a frame the spins experience an effective field, $B_{\text{eff}}(\omega)$ in the z-direction so that

$$\dot{\mu}_s = \gamma \mu_s \times (\mathbf{B} + \omega/\gamma) = \gamma \mu_s \times \mathbf{B}_{\text{eff}} \tag{3.8}$$

For a frame rotating at the Larmor frequency since $(\omega_{\mathbf{0}}) = -\gamma(\mathbf{B_0})$ we find that B_{eff} becomes zero and projection of the spin angular momentum in the xy-plane is constant.

3.2.2 Nuclear Paramagnetism

So far only the dynamic behaviour a single spin has been examined. Now a system consisting of a macroscopic number, N_{V}, of spin $I = 1/2$ ^{3}He particles will be considered where N_{V} is large enough to be considered a thermodynamic variable. Now the components of $\mathbf{S}$ in the xy-plane will average to zero and only the quantised S_{z}-component remains. For $I = 1/2$, $m = \pm 1/2$ and the equilibrium populations of spins aligned parallel, $N_{\uparrow}$, and anti-parallel, $N_{\downarrow}$, to $\mathbf{B}$ are described by the Boltzmann relation

$$\frac{N_{\uparrow}}{N_{\downarrow}} = \exp(\Delta \mathrm{E}/\mathrm{k_B T}) = \exp(\gamma \hbar \mathrm{B}_0/\mathrm{k_B T}) \tag{3.9}$$

At finite temperature $N_{\uparrow} \neq N_{\downarrow}$, resulting in a macroscopic magnetic moment given by

$$M_0 = \mu(N_{\uparrow} - N_{\downarrow}) \tag{3.10}$$

where $\mu = \mu_{\mathrm{s}} \cdot \hat{\mathbf{k}}$. In the low polarisation regime where $\hbar\gamma B_0 \ll 2k_{\mathrm{B}}T$ the populations of each energy level and hence $\mathbf{M_0}$ obey Curie's law, which since for a paramagnetic system the static susceptibility, $\chi_0 \ll 1$, can be expressed as

$$\mathbf{M_0} = \frac{\chi_0}{\mu_0}\mathbf{B_0} \tag{3.11}$$

where $\mu_0 = 4\pi \times 10^{-7}\ \mathrm{H\,m^{-1}}$ and χ_0 is given by

$$\chi_0 = \frac{N_{\mathrm{V}}\mu_0\gamma^2 S^2}{3k_{\mathrm{B}}T} \tag{3.12}$$

where $S^2 = 3\hbar^2/4$. For our system Curie law should be valid over the entire experimental range. Combining 3.7 and 3.10 allows us to talk about the dynamics of the macroscopic observable $\mathbf{M}$ rather than the microscopic μ_{s}.

3.2.3 Relaxation

This section deals with how the magnetisation returns to equilibrium after being displaced into a higher energy state. This relaxation is characterised by two time constants, T_1 which describes relaxation parallel to the applied field and T_2 which describes the relaxation in the plane orthogonal to the applied field. Here the non-equilibrium initial state is assumed.

Spin-Lattice Relaxation (T_1)

The thermodynamic picture of equation 3.9 conflicts with the quantum equation of motion 3.7 where spin precession occurs without dissipation and there is no mechanism for the system to come into equilibrium. In the quantum picture interactions with external degrees of freedom have been ignored. For a real system there are a variety of mechanisms through which the spins can exchange energy with their surroundings, these are collectively labelled as the Lattice. In the field of NMR the act of $\mathbf{M}$ returning from a perturbed state to its equilibrium value of $M_0\hat{\mathbf{k}}$ is termed relaxation. The rate at which a perturbed spin system returns to the equilibrium condition is characterised by the time constant T_1 where $\dot{M}_{\mathrm{z}} = (M_0 - M_{\mathrm{z}})/T_1$. Hence T_1 is a measure of how efficiently the spins can exchange energy with the Lattice.

Spin-Spin Relaxation (T_2)

Here we assume that in the initial state of the system we find $M_{\mathrm{xy}} \neq 0$. This is fundamental to pulsed NMR and section 3.3.1 shows how this can be achieved experimentally.

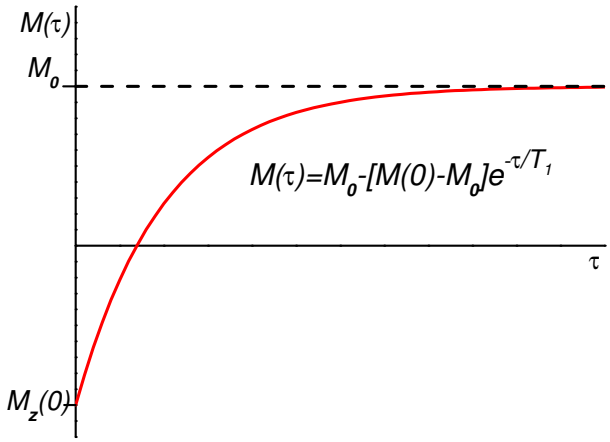

Figure 3.1: Recovery of the longitudinal relaxation with time-constant T_1.

From the definition of the rotating frame 3.8 we have $\dot{M}'_{\mathrm{xy}} = 0$, however this is making the assumption that every spin sees the same field B_0. In a real system B_0 has some temporal and spatial variation, which can be accounted for by introducing a local field b_{loc} such that $\mathbf{B}_{\mathrm{loc}} = (B_0 + b_{\mathrm{loc}})\,\hat{\mathbf{k}}$. We choose to define the local field so that $\langle b_{\mathrm{loc}} \rangle = 0$ over the system such that $\langle \mathbf{B}_{\mathrm{loc}} \rangle = \mathbf{B}$. This additional term causes each spin to process about the z'-axis in the rotating frame with a different local Larmor frequency ω_{loc}. For a macroscopic system of spins in the $x'y'$-plane this causes dephasing which will reduce $M_{\mathrm{x'y'}}$ to zero. A Gaussian distribution of b_{loc} leads to an exponential relaxation with $\dot{M}_{\mathrm{xy}} = M_{\mathrm{xy}}/T_2$.

An important contribution to the transverse relaxation is caused by spatial inhomogeneities in the applied NMR field. Temporal inhomogenieties are neglected as we use superconducting magnets operated in persistent mode. We define a relaxation time constant, T_2^*, to include this where

$$\frac{1}{T_2^*} = \frac{1}{T_2} + \frac{1}{T_{2,\mathrm{mag}}} = \frac{1}{T_2} + \gamma \Delta B \tag{3.13}$$

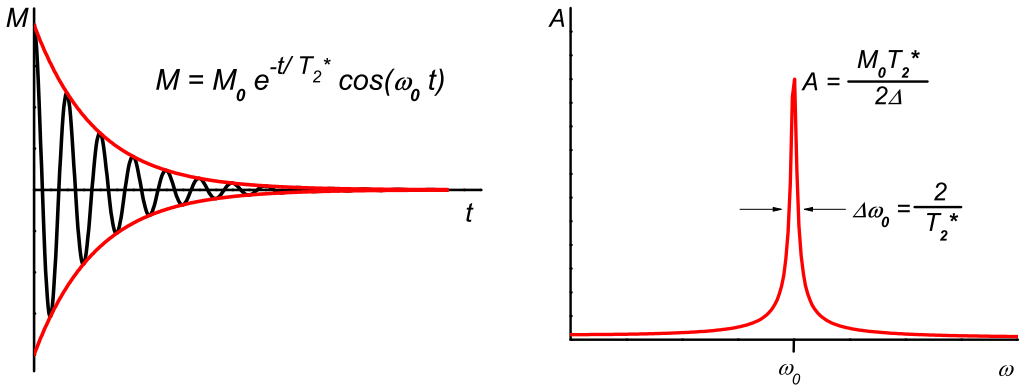

Figure 3.2: Relaxation of the transverse magnetisation showing exponential decay in the time-domain with time constant T_2^* and the resultant FFT spectrum in the Frequency-Domain

Here $T_{2,\mathrm{mag}}$ is the magnet contribution and $\gamma \Delta B = \Delta\omega$ is the spread of NMR frequencies caused by a magnet inhomogeneity ΔB. For a superconducting magnet $\Delta B / B_0$ is a constant. T_2 is the intrinsic transverse relaxation time of the system.

3.2.4 Bloch equations

The dynamic behaviour of the magnetisation can be expressed in the form of the Bloch equations

$$\begin{aligned} \dot{M}_\mathrm{x} &= \gamma \left|\mathbf{M} \times \mathbf{B}\right|_\mathrm{x} - M_\mathrm{x}/T_2 \\ \dot{M}_\mathrm{y} &= \gamma \left|\mathbf{M} \times \mathbf{B}\right|_\mathrm{y} - M_\mathrm{y}/T_2 \\ \dot{M}_\mathrm{z} &= \gamma \left|\mathbf{M} \times \mathbf{B}\right|_\mathrm{z} + \left(M_0 - M_\mathrm{z}\right)/T_1 \end{aligned} \tag{3.14}$$

The detection method used observes only the M_x component of the magnetisation. From equation 3.14 we see that this evolves as

$$M_\mathrm{x}\left(t\right) = M_\mathrm{x}\left(0\right) \cos(\omega_0 t) \exp(-t/T_2) \tag{3.15}$$

where we assume $M_{\mathrm{xy}}(0) = M_{\mathrm{x}}(0)$, i.e the initial magnetisation is in the x-direction. The observed magnetisation consists of an exponentially decaying envelope function modulated by a sinusoid at the Larmor frequency.

3.3 Pulsed NMR

3.3.1 Spin Tipping

In the rotating frame $B_{\mathrm{eff}} = 0$. If a field $B_1'\hat{\jmath}'$ is applied to the spins, where $\hat{\jmath}'$ is the unit vector in the y'-direction, a torque of the form 3.6 will cause $\mathbf{M}$ to rotate in the $z'x'$-plane by an angle θ given by

$$\theta = \gamma B_1' \tau = \omega_1 \tau \tag{3.16}$$

This means that the magnetisation can be tipped by an arbitrary angle by varying the pulse length, τ, of the B_1' field. In the lab frame B_1 must precess in the xy-plane at the Larmor frequency. In practice it is not possible to produce a constant magnitude B_1 field using a single coil as this necessitates the use of two orthogonal coils producing oscillating fields with a phase difference of $\pi/2$. Usually only a single transmitter coil is used to produce a field $B_1 \cos(\omega_0 t)\hat{\jmath}$. In the rotating frame it is useful to think of this as the superposition of two fields with equal magnitudes of B_1'; one which is constant in the y'-direction, whilst the other precesses about the z'-axis with angular frequency $2\omega_0$. In general we find that the $2\omega_0$ component is far enough away from resonance that it can safely be ignored and $2B_1 = B_1'$.

3.3.2 NMR Pulse sequences

It is only possible to observe M_{x} directly, however, by manipulating the spins using a series of NMR pulses we are able to measure M_{z}, T_1 and T_2.

Measuring T_2^* by $90° - \mathrm{FID}$

We can tip the spins by a 90° angle relative to the z-axis by applying a $\mathbf{B_1}'$ field for a time τ_{90} where $\gamma B_1 \tau_{90} = \pi/2$. Following the removal of $\mathbf{B_1}'$ the spins can precess freely in the B_0 field. The rate of decay of $M_{\mathrm{x}}(t)$ gives us the time constant T_2^* and $M_{\mathrm{x}}(0) = M_0$.

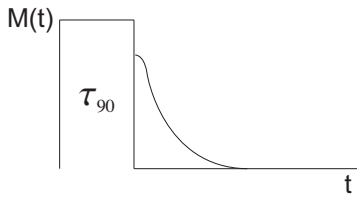

Figure 3.3: Pulse sequence diagram for $90° - \mathrm{FID}$ showing the preparatory pulse and resultant NMR response.

Whilst the spin tipping pulse is being applied the transverse relaxation occurs at a rate $T_2^*/2$. Therefore to extrapolate back to $t = 0$ for the calculation of M_0 we extrapolate back to the centre of the pulse. For short T_2^* this becomes important as the dead time is shorter for smaller values of B_1, but the signal size decreases exponentially in t. The pulse time is optimised for each system to achieve the optimum SNR, however as we apply our NMR pulses in integer numbers of cycles at ω_0 the available pulse times are quantised in units of $1/\nu_0$. The experiments described in this thesis were performed at low frequencies where $1/\nu_0$ is relatively

long compared to T_2^*. This meant that we could only apply a short number of cycles, for example a 50 µs pulse at 100 kHz is only 5 cycles.

Measuring T_1 by $180° - \tau - 90° -$ FID

It is possible to measure T_1 using a series of NMR pulses to prepare the system. For our system with short T_1 and T_2 a $180° - \tau - 90°$ sequence is most appropriate. Here an initial 180° pulse is applied which tips the spins so that $M_z(0) = -M_0$ and $M_{xy} = 0$. The magnetisation recovers according to equation 3.14 so that $M_z(t) = M_0 - [M_0 - M(0)]\exp(-t/T_1)$. After a time τ a 90° pulse is applied, tipping the spins into the xy-plane. The initial magnitude of the FID is $M_z(\tau)$, and by repeating the measurement over a range of τ the relaxation time T_1 can be determined. This pulse sequence is commonly referred to as the Inversion Recovery technique and is shown pictorially in figure 3.4.

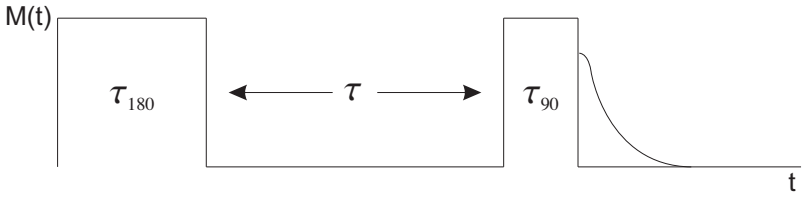

Figure 3.4: Pulse sequence diagram for $180° - \tau - 90° -$ FID. Here the pulse lengths τ_{90} and τ_{180} are assumed small compared to the recovery time τ so that following the 90 degree pulse the magnetisation will be $M_z(\tau)$.

Measuring T_2 by Spin Echo

For a localised spin system it is possible to reverse the effect of static field inhomogeneities on T_2^* and observe the intrinsic T_2 of the system by the method of spin

echoes. For such a spin in the $x'y'$-plane with precessional frequency $\omega_{\rm loc} = \gamma b_{\rm loc}$, if initially the spin is in the x'-direction, after a time t the spin will make an angle $\omega_{\rm loc}t$ to the x'-axis. If a 180° pulse is then applied in the x'-direction after a time τ its component magnetisation will undergo the transformation

$$\begin{aligned} \mu_{\rm x'} &\rightarrow \mu_{\rm x'} \\ \mu_{\rm y'} &\rightarrow -\mu_{\rm y'} \\ \mu_{\rm z'} &\rightarrow -\mu_{\rm z'} \end{aligned} \tag{3.17}$$

So that following this pulse the spin will be at an angle $-\omega_{loc}\tau + \omega_{loc}t'$ to the x'-axis, where t' is $t - \tau$, the time elapsed since the 180° pulse. Clearly when $t' = \tau$ the spin will be in the x'-direction, independent of the magnitude of ω_{loc} so that for a system with a macroscopic magnetisation the 180° pulse will re-phase $\mathbf{M_{xy}}$ with the decrease in magnitude of $M(2\tau)$ given by the intrinsic T_2 of the system. By varying the time τ the time constant T_2 can be established similarly to T_1 in the preceding section. This method of reading out the NMR response of the system is only possible when there is a separation in timescales so that $T_2^* \ll T_2$, as we must wait for the initial FID to decay sufficiently before applying the rephasing pulse in order to observe the echo. In this experiment the high homogeneity magnet without shim coils and short T_2 meant that in general $T_2 \approx T_2^*$ and echoes were not observable. However for the ^{4}He preplated experiment for higher coverages it was possible to make some spin echo measurements.

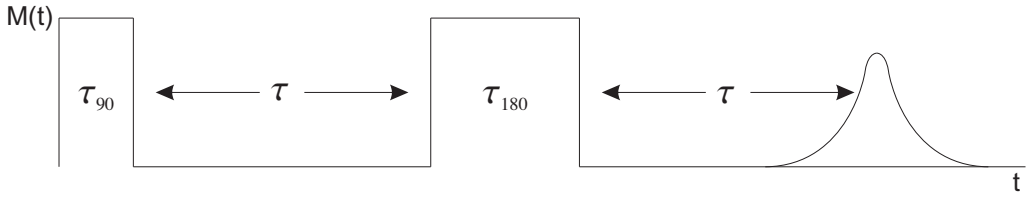

Figure 3.5: Pulse sequence diagram for $90° - \tau - 180° - \text{FID}$ showing the formation and decay of the spin echo

3.3.3 Relaxation in the Frequency Domain

Once captured we apply a fast Fourier transform (FFT) to the FID to obtain the frequency spectrum of the relaxation. The Fourier transform of an exponentially decaying magnetisation of the form given in equation 3.15 is Lorentzian in the frequency domain. The linewidth of the resonance, $\Delta\nu$, is related to the time domain relaxation rate by $\Delta\nu^* = 1/\pi T_2^*$ and the magnitude of the Lorentzian, H, is related to the initial FID amplitude, A_0, in the time domain by

$$H(\tau) = \frac{A_0 T_2^*}{2\Delta} \tag{3.18}$$

where $1/2\Delta$ is the Nyquist frequency. The decay of the transverse magnetisation begins when the readout pulse is initiated, however it is necessary to allow a dead time τ_d following the end of a transmitter pulse before data capture can begin. Therefore the experimentally observed FFT is for the magnetisation $M(\tau)$. For an FID obtained by a 90° readout pulse of duration τ_{90} to obtain true value of $M(0)$ we must extrapolate back by a time $\tau_d + \tau_{90}/2$.

Chapter 4

Instrumentation

4.1 The Cryostat

The experiments described in this thesis were performed between 1.5 K and 9 K using a conventional pumped ^{4}He-pot cryostat with continuous fill line. The insert was mounted in a Cryogenics Dewar with a super insulation outer vacuum can, OVC. The range of temperatures studied was determined by the base temperature of the cryostat and the critical temperature, T_c, of Niobium, Nb.

The insert consists of a single vacuum space, the IVC, containing three thermally isolated platforms from which various components were mounted. The brass outer body of the IVC is bolted directly onto the 4 K plate and sealed with an indium o-ring, providing a good vacuum over extended periods. The 1 K pot is mechanically supported from the 4 K plate by the thin-walled stainless steel pot pumping line, providing adequate thermal isolation. The SQUID plate houses the SQUID shield

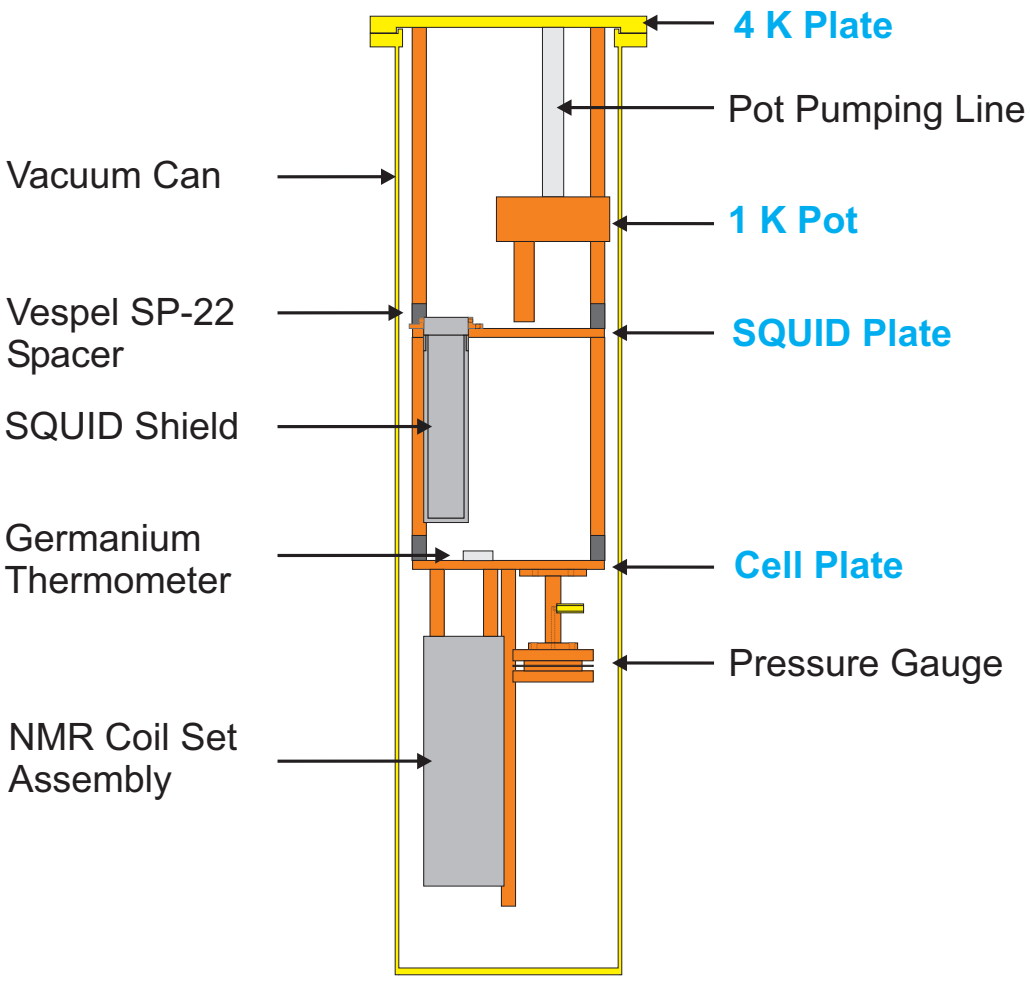

Figure 4.1: Scale Diagram of the insert below the 4 K plate

assembly and is suspended from the 4 K plate by three copper rods with insulating Vespel spacers. The cell plate is suspended from the SQUID plate by the same method and houses the NMR coil set, cell and *in situ* pressure gauge. A schematic diagram of the IVC is shown in figure 4.1. The SQUID plate and cell plate were thermally anchored to the pot with copper wire. The strengths of the thermal links were calculated such that the temperature of each plate could be adjusted independently.

4.1.1 Thermometry and Temperature Control

The primary thermometer for this experiment is a Lakeshore (Model GR-200A-500-CD-1.4D) germanium resistance thermometer mounted on the cell plate. This is calibrated by Lakeshore against the ITS90 temperature scale [21] from 1.4 K to 100 K covering the whole experimental range. The pot, SQUID plate and cell plate each had two additional secondary carbon resistance thermometers, one Allen Bradley type and one Speer type. These are independently calibrated against the germanium resistor during each cool down whilst the IVC contained exchange gas and are primarily used as a diagnostic aid. Resistances were monitored by an eight channel Picowatt AVS-47B bridge controlled remotely by a computer running LabVIEW. A summary of typical resistances for the various resistance thermometers and heaters at different temperatures is given in table 4.1. The resistances measured for the Speer and Allen Bradley resistors were observed to vary slightly during each cooldown and were calibrated each run at 77 K and 4.2 K

The temperature of the cell plate is controlled by an automated feedback technique, illustrated in figure 4.2. Here a resistance value corresponding to a target tempera-

Table 4.1: Resistance values of various devices for different temperatures. AB and Speer refer to Alan-Bradley and Speer type carbon resistors. Thermometer resistances are from 4-point measurements. All others include lead resistances.

Device	Resistance (Ω)		
	RT	77 K	4.2 K
Pot Speer	490.9	565.9	940.5
Pot AB	281.4	338.9	3306
SQUID Speer	496.2	571.9	981.3
SQUID AB	248.3	307.7	3226
Cell Speer	471.2	542.5	918.3
Cell AB	257.3	316.9	3216
Germanium	1.4017	1.7477	475
Pot Plate Heater	113.9	109.5	92.8
Cell Plate Heater	278.7	266.7	180.7
SQUID Plate Heater	215.1	208.2	183.7
Persistent Switch Heater	470.4	474	477
Magnet Current Leads	22.1	17.4	0.4
Potential Tap	294.4	291.5	283.1
Transmitter	367.4	343.1	1.4
Magnet Coil	16.44×10^3		
Magnet leads to Spot Welds	10.1		

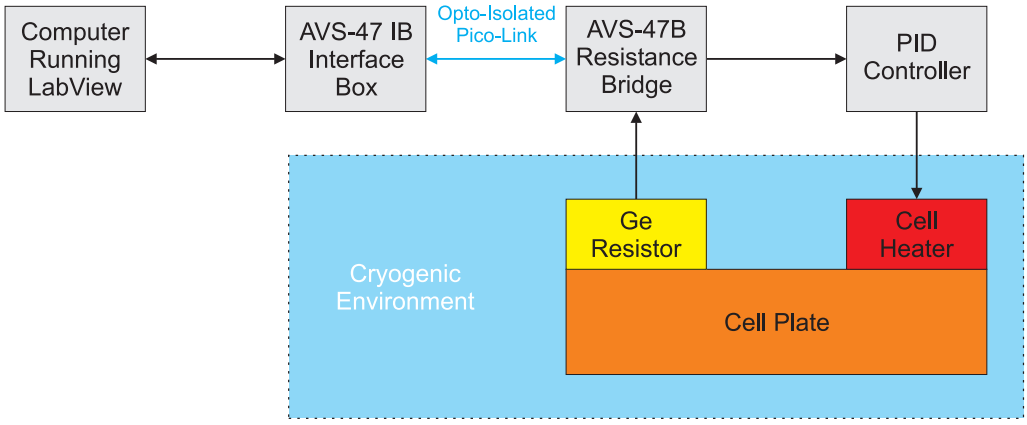

Figure 4.2: Computer controlled PID feedback temperature stabilisation

ture for the germanium resistor is input as a reference to the AVS bridges differential amplifier. The bridge outputs an error voltage proportional to the difference between the reference and measured resistances which is fed through a PID controller to the cell plate heater. The AVS-47A bridge is controlled remotely by a AVS-47IB computer interface using an opto-isolated PicoLink. This interface allows the reference resistance to be set and read out remotely using LabVIEW so that the temperature could be remotely controlled and temperature sweeps automated.

4.2 The Main Gas Handling System

A new Gas Handling System, GHS, was created for this experiment to store cleanly and conveniently the required range of adsorbates and provide a calibrated dosing volume. It incorporated designed features to facilitate automation of the isotherm process. A schematic diagram for the GHS in its initial configuration is shown in figure 4.3. Significant changes to the system were made between the pure ^{3}He adsorption experiment and the experiment in which the substrate was first preplated with ^{4}He.

Adsorbate gases are stored in cylinders 1, 2 and 3. For the experiments outlined in this work cylinder 1 was filled with ^{3}He at high pressure, cylinder 2 contained ^{4}He collected from the boil-off of a transport Dewar and cylinder 3 remained evacuated. As the ^{4}He cylinder was maintained at approximately atmospheric pressure the gas was replaced regularly to minimise any possible contamination.

Whilst performing isotherms a quantity of the required adsorbate was transferred from one of the main storage cylinders to the large manifold, MF. This volume was

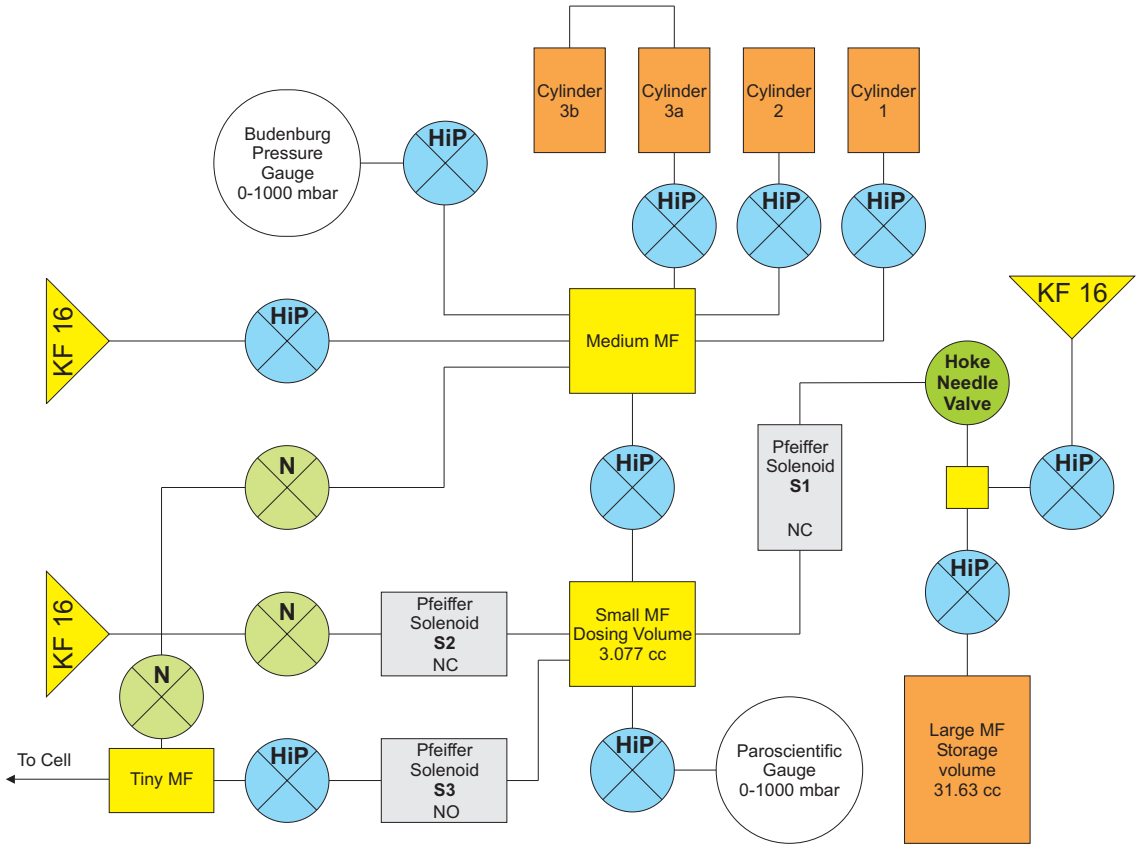

Figure 4.3: Schematic diagram of the main gas handling system. Manually operated valves are produced by High Pressure Equipment Company [22] (HiP), Swagelok [23] (N) witha metering valve by Hoke [24]. Remotely operated solenoid valves are by Pfeiffer Vacuum [25]

measured to be $(31.63 \pm 0.01)\,\mathrm{cm}^3$ by Dr. J. Nyéki. The calibrated dosing volume consists of the small MF and Paroscientific Digiquartz pressure gauge volumes. The volume was determined as $(3.077 \pm 0.001)\,\mathrm{cm}^3$ by pressure sharing with the large MF. The Digiquartz pressure transducer operates using two quartz crystal oscillators, the frequency of one is sensitive to pressure changes and the other sensitive to temperature. The temperature sensor is used to compensate for thermally induced changes in the frequency of the pressure sensor, but is also used to give an absolute ambient temperature reading. The two oscillators are read out using a Keithley 2000 DMM and scanner card operated remotely through LabVIEW.

4.2.1 Automation of the Gas Handling System

Adsorption isotherms can yield a great deal of thermodynamic information about physisorbed systems. For porous media it is interesting to perform both adsorption and desorption isotherms where observations of hysteresis can give information about the substrate including the shape of the pore entrances [26]. Performing desorption isotherms on MCM-41 type materials is highly labour intensive as the binding energy of the substrate at low temperatures is large. The gas handling system was designed to allow the automation of part of the adsorption and desorption processes. The concept was to program a computer running LabVIEW to control the isotherm process in an intelligent way. To enable this three remotely controlled Pfeiffer solenoid valves were installed as shown in figure 4.4, operated by a control box with a computer interface. The program would open valve S1 allowing the dosing volume to be filled from the Large MF storage volume. The Hoke metering valve regulated the gas flow rate such that the pressure increase in the dosing volume was slow enough to be able to control the final dosing amount. Once the pressure in the dosing volume had stabilised and been recorded valve S2 would be opened admitting the adsorbate to the cell. S3 lead to a turbomolecular pump through a low impedance LN_2 cold trap to evacuate the dosing volume in the case of overfilling or during the desorption process.

There were several advantages associated with the implementation of this system, however there were also number of technical issues. Full isotherm automation was never attempted, however the computer controlled activation of the valves enabled part of the isotherm process to be completed from a remote location. Using a computer to control the activation of the valves it was possible to limit the sequence in

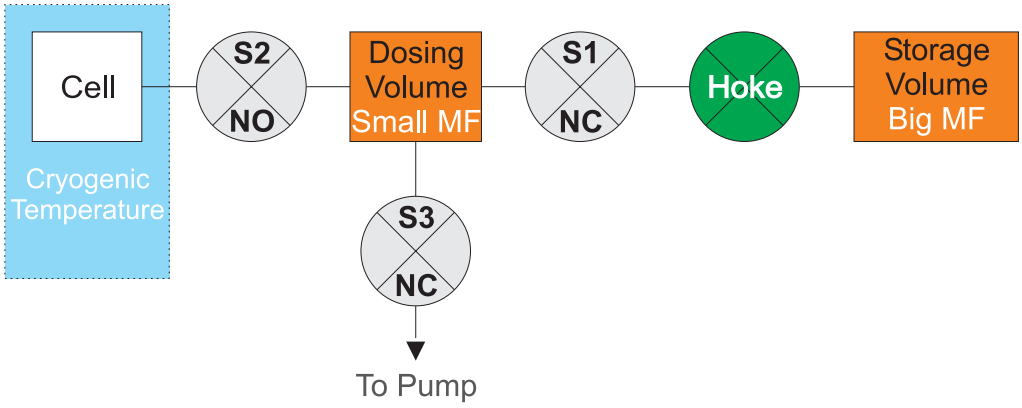

Figure 4.4: Schematic diagram of the dosing system. The grey valves labeled S1, S2 and S3 are the Pfeiffer solenoid valves. NO signifies that the valve is normally open and NC that it is normally closed. These are the states when the valves are not energised. The green valve is a Hoke metering needle valve.

which they could be opened, preventing the storage volume being opened directly to the cell. However, there was a serious issue found with this particular implementation of these valves. The equilibrium operating temperature of these valves when constantly energised was measured to be 80 °C using a thermocouple mounted on the body of S2. The configuration of the valves in figure 4.4 necessitated one of the valves to be energised to isolate the dosing volume, leading to thermal gradients across the dosing volume. This added uncertainty to our measurement of p/T used to calculate the adsorbate amount.

Automating the isotherm process appears to be worth pursuing. The most simple solution to the heating problem would be to replace the valve S2 which is normally open with one that is normally closed and adding additional heatsinking to all valves. This way the temperature gradients across the dosing volume may be eliminated. A more satisfactory solution would be to implement a pneumatic system of valves such that the state of the valve could be swapped without causing heating. In any case the safest option would be to have all valves closed when not energised to protect

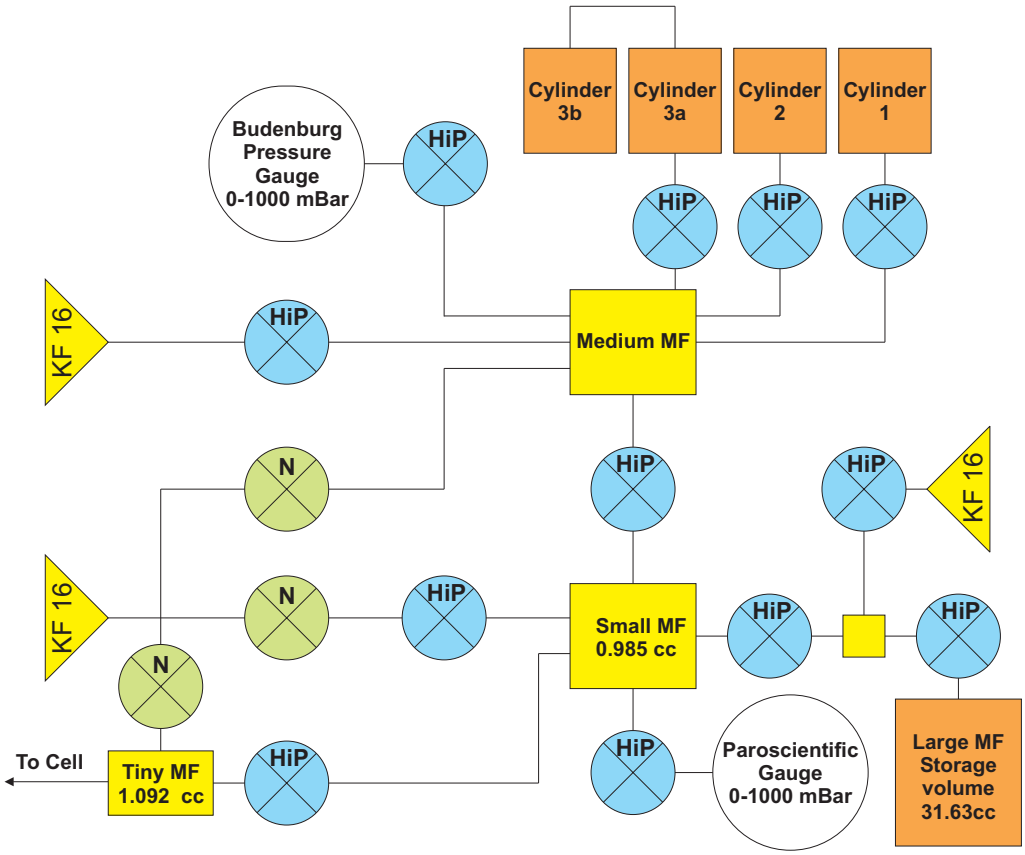

Figure 4.5: Schematic diagram of the main gas handling system after modification. The Pfeiffer solenoid valves have been replaced with HiP valves where necessary and the Hoke metering valve has been removed. The new dosing volume is $0.985\,\mathrm{cm}^3$.

the sample in case of power failure.

For the ^{4}He experiment the GHS was modified and the *in situ* pressure gauge was added. A schematic diagram of the redesign is shown in figure 4.5. The solenoid valves were removed and replaced with HiP valves where necessary. The metering valve was also removed to improve efficiency when pumping out the system. The small MF was replaced to accommodate the HiP flanges which changed the dosing volume to the new volume measured to be $(0.985 \pm 0.001)\,\mathrm{cm}^3$. This coupled with a change in isotherm technique greatly improved the quality of the isotherms produced.

4.3 *In-Situ* Pressure Gauge

A self-contained Straty-Adams type capacitive pressure transducer [27, 28] has been developed to perform *in-situ* pressure measurements which have been used to characterise thermodynamic properties of the adsorbed system. The gauge, designed by J. Nyeki, was mounted on the cell plate and provided μbar precision in the low pressure limit with a range of 10 mbar. This removed the need for thermomolecular pressure corrections associated with determining pressures at room temperature and greatly improved the sensitivity of the measurement. A schematic diagram of the pressure gauge is shown in figure 4.6 and photographs of the gauge at various stages of construction are shown in figure 4.7.

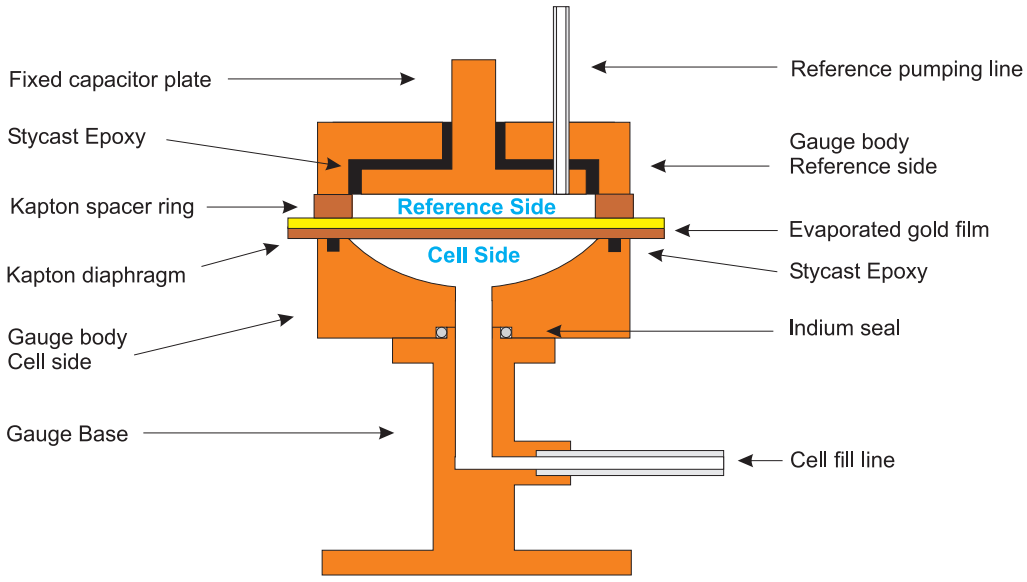

Figure 4.6: Schematic drawing of the Straty-Adams type pressure gauge used to perform *in situ* vapour pressure measurements

The pressure gauge consists of a capacitor formed of one fixed and one flexible plate. The volume between the plates is held at a good vacuum while the outside of the flexible plate is exposed to the cell pressure. A pressure differential across the

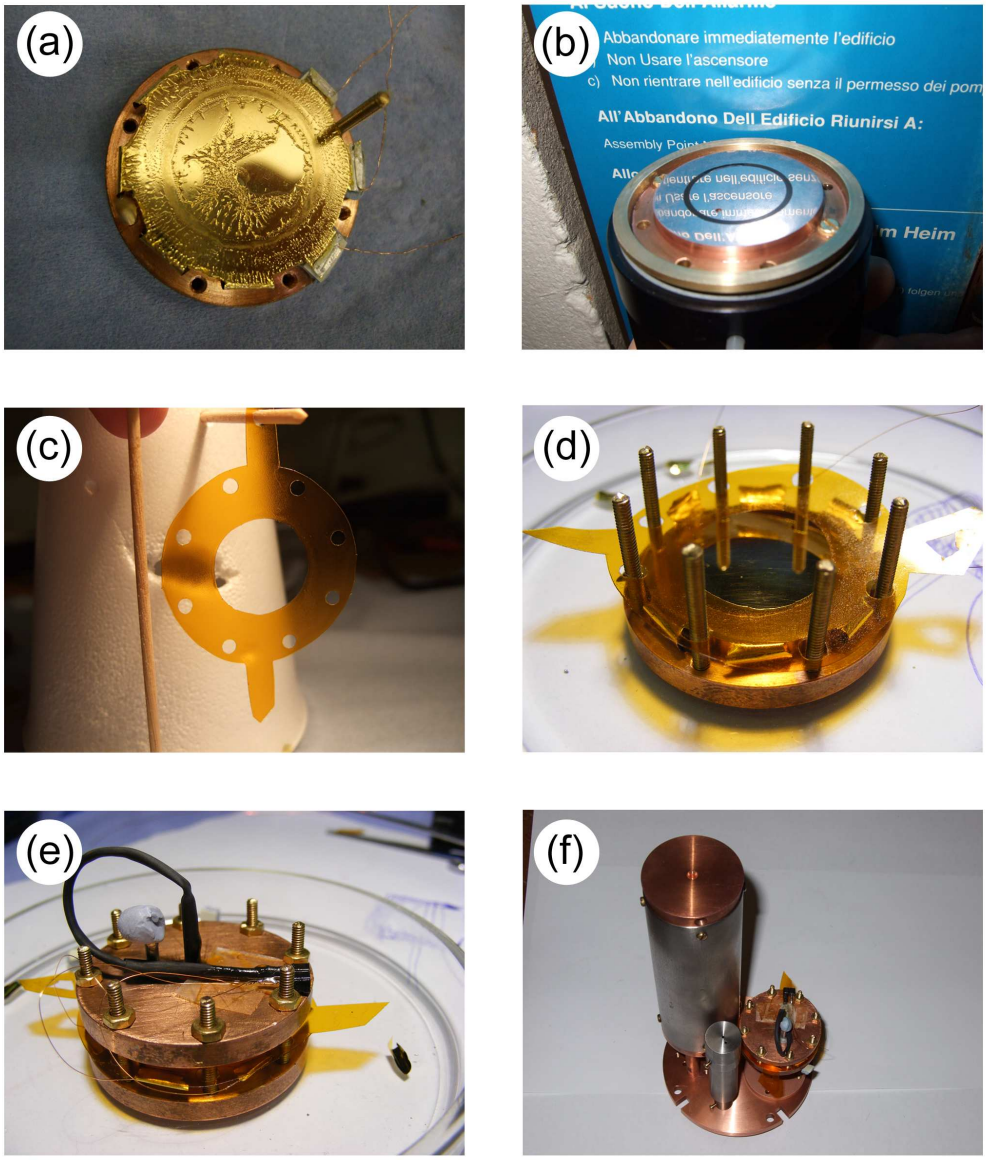

Figure 4.7: (a) The gold plated Kapton membrane epoxied to the cell side of the gauge. This picture shows the how grease has crept onto the gauge surface under vacuum. (b) The reference side of the gauge showing a mirror finish after polishing. The outer polished surface is part of the gauge body that seals to the Kapton spacer. Inside the Stycast ring is the fixed capacitor plate and the small hole is the reference pumping line. (c) The Kapton spacer after applying a Apiezon N vacuum grease/toluene mixture. (d) The cell side of the gauge with Kapton spacer ready for final assembly. (e) The completed gauge with electrical connector varnished to the body. (f) The gauge mounted on the cell plate with NMR coil set and a shield for an unused SQUID noise thermometer.

diaphragm cause it to deflect from its equilibrium position changing the capacitance, which can be read out to high precision using lock-in techniques. The sensitivity and range of the gauge is determined by the plate area and equilibrium separation of the plates, the Young's modulus of the diaphragm, and the sensitivity of the readout method.

4.3.1 Construction

The main gauge assembly consists of four machined OFHC components; the base, the cell side gauge body, the reference side gauge body and the fixed capacitor plate. The diameter of the gauge body is 36 mm and the diameter of the fixed capacitor plate is 16 mm.

The fixed capacitor plate was glued into the reference side of the gauge body in a two part process. Firstly the gauge body was cleaned using acetone and ethanol in an ultrasonic bath before preplating with a Stycast layer made of an equal weights mixture of Stycast 2850ft with LV24 catalyst and Stycast 1266 parts A and B. This forms an epoxy with the required thermal expansion properties and also is machinable. After leaving to set for 24 hours the Stycast was machined to accept the fixed capacitor plate. This was then glued into place using a similar Stycast mixture. This two part process ensured that the gauge body did not short to the capacitor plate.

To ensure the optimum sensitivity, range and to understand the behaviour of the gauge it is important that the capacitive plates are flat and parallel with the minimum surface roughness. To achieve this the assembly was machined flat removing

any excess epoxy before polishing. A Buehler Minimet 1000 polishing machine was used with a clamp designed to keep the gauge assembly flat during the grinding process. The capacitor surface was polished with successively fine abrasives from 600 grit sand paper to 1 μm diamond paste providing a mirror finish, shown in figure 4.7(b).

The diaphragm is made from 12.5 μm Kapton. This was stretched tightly and clamped into a metallic base where it was evaporated with a gold film in a clean room. The cell side of the gauge was then prepared. The concave surface was polished by hand down to 9 μm diamond paste. This was cleaned ultrasonically before gluing to the bare side of the diaphragm using Stycast. The electrical contacts to the gold plated Kapton diaphragm were made by roughening the surface of the gold and using silver paint to attach copper wires. The gauge was now ready for the final assembly process.

The separation of the two capacitor plates is determined by the thickness of a Kapton spacer ring which sits between the gold plated diaphragm and the fixed plate on the reference side of the gauge, shown in figures 4.6 and 4.7(c)-(d). This was chosen to be 37.5 μm. The spacer forms part of the gauge body and the vacuum seal is achieved using cryogenic vacuum grease. The choice of vacuum grease and amount applied were found to be crucial. Initially Dow Corning high vacuum grease [29] was carefully applied to both sides of the spacer ring using a sharpened q-tip. The grease was found to spread when held under vacuum, causing the two capacitor plates to stick together on cooling to 77 K. The spread of the grease is shown in figure 4.7 (a). This Problem was solved by replacing the Dow Corning grease with Apeizon N cryogenic vacuum grease [30]. As this is not silicon based it does not suffer from creep in the same way. A technique was developed to apply a thin homogeneous

coverage of the grease. The spacer was dipped into a dilute solution of the Apeizon N grease and toluene. The spacer was redesigned with a tag on the edge of the ring, as seen in figure 4.7(c), so that it could be held vertically whilst drying. On the opposite side of the ring a second tag was added to focus droplets and stop puddles forming at the bottom edge due to surface tension. This was left in a desiccator to keep clean whilst drying.

4.3.2 Gas Handling System For The Pressure Gauge

A simple gas handling system was made for the gauge and mounted on the top of the insert. A diagram of this is shown in figure 4.8. This was needed for a number of reasons. Firstly it was important to maintain our sample always under vacuum or in an inert atmosphere. The addition of the pressure gauge complicates this slightly as we need to keep the pressure differential across the gauge preferably below 10 mbar where the Kapton membrane deflects by the width of the spacer causing the gauge to short. Exceeding this value causes stress at the edge of the diaphragm where it is clamped by the body of the gauge.

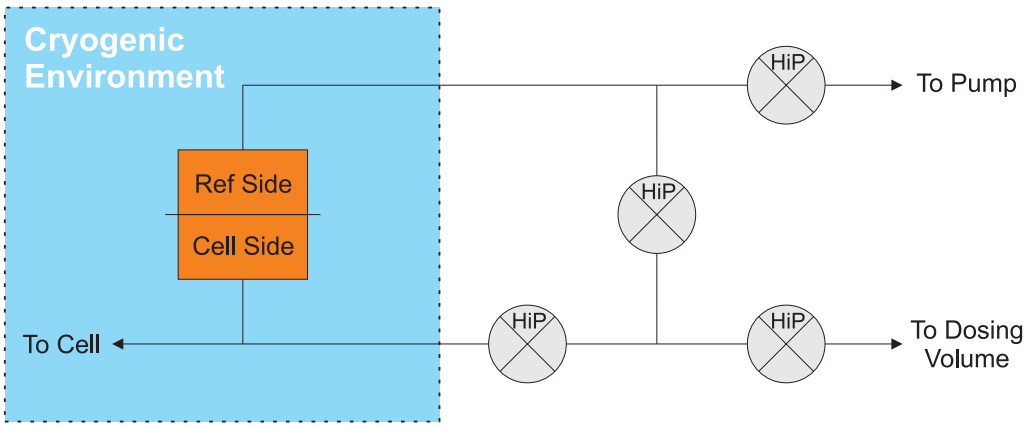

Figure 4.8: Gas Handling System for Straty-Adams type *in-situ* pressure gauge

The easiest way to prevent overpressure is by interconnecting both sides of the gauge through a low impedance pathway. We wanted to keep dead volumes to a minimum necessitating narrow fill lines and mounting the gas handling system directly on the cryostat to keep the pathway short. Also our cryostat is mobile, lifted in and out of a stationary Dewar between runs. To do this we need to disconnect the insert fully from the main gas handling system. Having this smaller gas handling system mounted on the cryostat meant that the system could be sealed from atmosphere during this process.

4.3.3 Capacitance Readout Method

Two methods were used to measure the gauge capacitance. For the initial ^{4}He isotherm a bridge circuit was assembled using a EG&G lock-in amplifier and inductive voltage divider, IVD. A nominal 33 pF surface mount reference capacitor was mounted on a thinned down PCB in a RF shielded box packed with Dow Corning vacuum grease and heatsunk to the cell plate. Stainless steel co-axial cables from Cambridge Magnetic Refrigeration [31] were used for the gauge and the reference capacitor. Using a cold reference and similar wiring should reduce changes in line capacitance due to changes in the helium bath level. A program was written in LabVIEW to automate the bridge circuit such that the lock-in sensitivity would autorange and the capacitance was constantly recorded. The sensitivity of this setup was 0.12 fF which is equivalent to 0.1 μbar, however at this sensitivity the measurements were very susceptible to thermal fluctuations and more reliable measurements were obtainable above 1 μbar.

For the second ^{4}He isotherm a Andeen-Hagerling 2550A capacitance bridge [32]

with ovenized reference capacitor was used. This had no facility to use an external capacitance standard. Initially the capacitances of the gauge and cold reference were measured independently so that an effective bridge ratio could be determined and compared to the IVD circuit. Performance of the two systems were found to be comparable. Although the AH bridge has an extra digit of precision this was found to be unstable for reading out the gauge, probably due to thermal and pressure fluctuations. The AH bridge has an internal averaging mode which could be set to give a more stable reading, however, this made the response time slow and hence was only used for taking pressure measurements, and when adding more helium to the system was turned off to observe the gauge response in real time. Measuring the cold reference for different bath levels showed that the change in the line capacitance was negligible and that suitable readings could be obtained measuring the gauge capacitance alone.

4.3.4 Calibrating The Pressure Gauge

The ratio of the gauge capacitance to that of the reference capacitor, $C_{\text{gauge}}/C_{\text{ref}}$ when using the inductive voltage divider is given by;

$$\frac{C_{\text{Gauge}}}{C_{\text{Ref}}} = \frac{R}{1-R} \tag{4.1}$$

where R is the bridge ratio. It was found experimentally that the deflection of the gauge from its equilibrium position is temperature independent, however the equilibrium gauge capacitance does show some temperature dependence associated with the change in tension of the Kapton membrane. The first step in calibrating the gauge was to measure the capacitance of the gauge in equilibrium as a function

of temperature, $C_0(T)$, over the experimental range. This was measured under vacuum both sides of the gauge open to each other through the gauge gas handling system and is plotted in figure 4.9. $C_0(T)$ was found to be non-linear over this range and was fitted to a 5^{th} order polynomial with good agreement. The value of the equilibrium point did show some hysteresis but this was found only to affect the DC offset. The difference between the maximum and minimum values of $C_0(T)$ was found to be equivalent to a pressure change of 1.2 µbar at constant temperature.

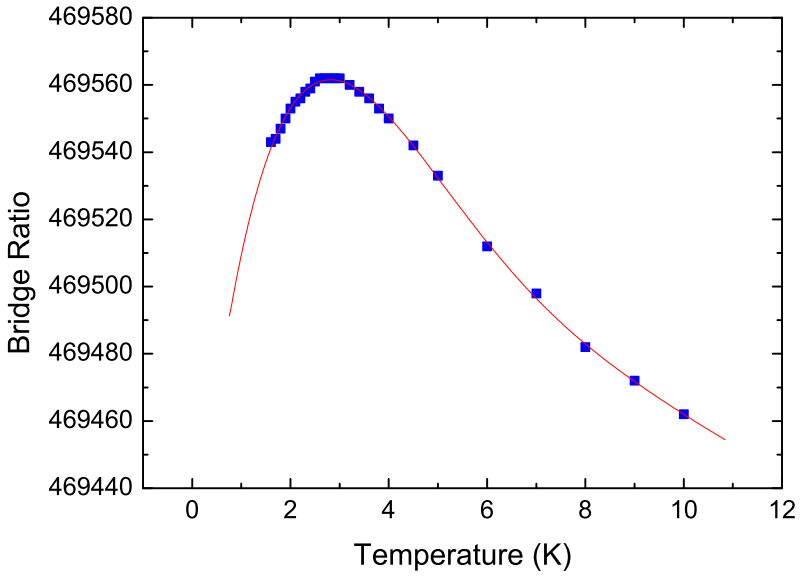

Figure 4.9: The equilibrium bridge ratio for the pressure gauge as a function of temperature.

The relative change in capacitance from its equilibrium value, $C - C_0$ is approximately a polynomial in P and was fitted on a log-log scale as shown in figure 4.10. For the experimental runs this calibration was performed during the isotherm process, at high temperatures and low coverages before reaching the area of interest approaching monolayer completion. The independent pressure measurements for the calibration were made using a Paroscientific Digiquartz pressure transducer [33] (Model No: 215A-101, Range: 0-15 psi) operated at room temperature as part of

the main gas handling system and read out by a Keithley 2000 DMM. Thermomolecular pressure corrections using the coefficients from [34] were applied, and for this system are calculated to be 3% for 1 mbar measured at room temperature for a cell temperature of 1.6 K.

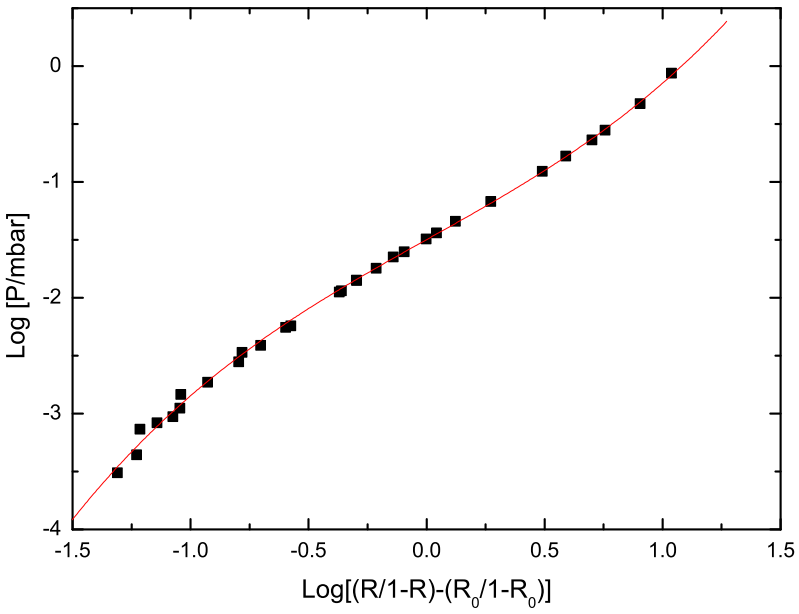

Figure 4.10: The bridge ratio measured as a function of pressure. Here R_0 is the ratio in equilibrium and includes pressure measurements at 7, 8 and 10 K. This was one of a number of calibrations used as the gauge response changes on thermal cycling and over extended time periods.

4.4 The NMR Spectrometer

We have performed broadband pulsed NMR at low frequencies using a DC SQUID NMR spectrometer similar to those described previously, for example [35]. A block diagram of the spectrometer created for this work is shown in figure 4.11. The compact NMR coil assembly is contained within a niobium superconducting shield, as shown in figure 4.12. The receiver and transmitter coils are wound of superconduct-

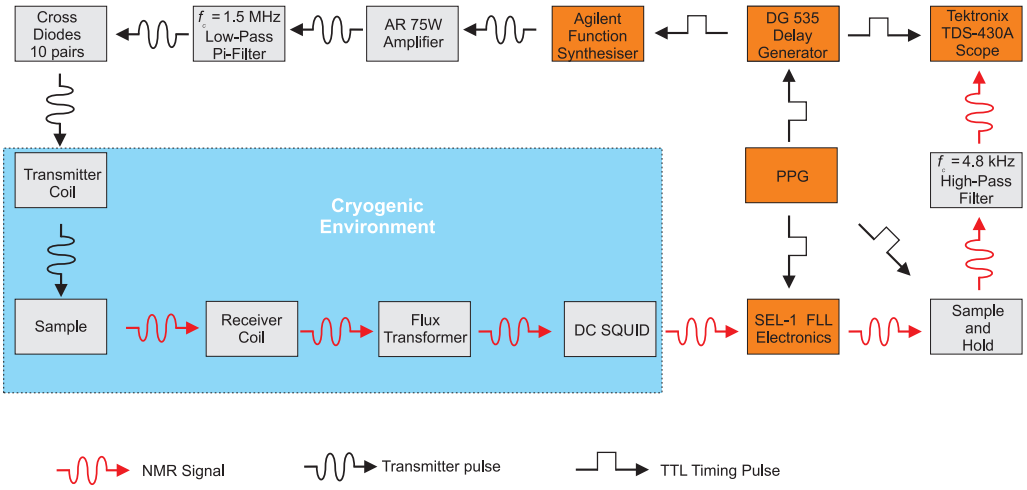

Figure 4.11: A block diagram of the NMR spectrometer. Orange items are controlled by a computer running LabView

ing wire on separate Kel-F formers in a saddle geometry around a cylindrical sample cell. These are located inside a small solenoidal static field magnet such that the magnetic fields produced by each of the coils are orthogonal.

The remotely mounted SQUID sensor is housed in a niobium shield and heat sunk to the ^{4}He-pot at around 1.5 K. This is coupled to the receiver coil through a superconducting flux transformer circuit incorporating an integrated Q-Spoiler current limiter, which consisting of a series array of hysteretic SQUIDs. The array is resistive for high currents and superconducting for low currents, and therefore limits the current in the input circuit due to cross-coupling from the transmitter pulse and shortens the spectrometer recovery time.

NMR experiments were carried out in the frequency range 80 to 240 kHz. In conventional NMR spectrometers operated at higher frequencies a gated sine wave is usually used to produce phase coherent NMR pulses and the output is mixed down to audio frequencies before amplification. A potential problem with this, which is of particular significance for the low amplitude signals in these experiments, is the

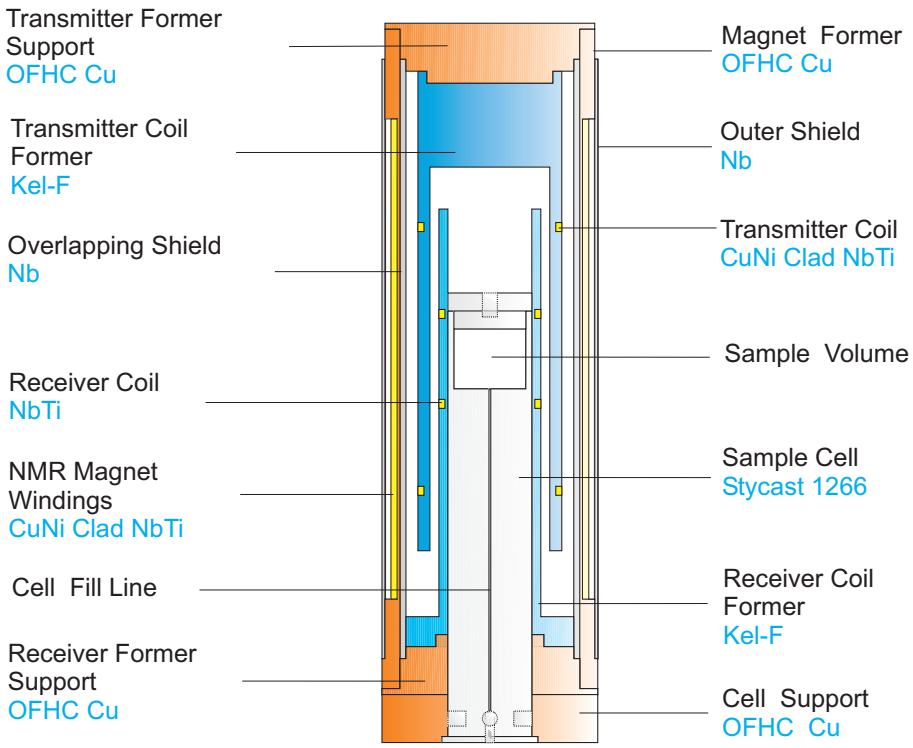

Figure 4.12: A Scale diagram of the compact NMR coilset with sample cell

possibility of feedthrough from the master oscillator frequency when the pulses are off. To avoid this problem 90° and 180° pulses where produced as integer cycle bursts from two Agilent 33220A Arbitrary Waveform Generators and a Stanford Research Instruments SRS DG535 Digital Delay/Pulse Generator with 5 ps delay resolution was used for precise timing of the waveform generators, and all were clocked from an SRS SC10 10 MHz ovenized quartz master oscillator. This set-up was used in conjunction with a home-built pulse generator, utilising a PIC micro controller, which also provided reset pulses to open the flux-locked loop (FLL) of the SQUID electronics whilst the transmitter pulses were on. The SEL-1 SQUID electronics [36, 37] allowed the FLL to be closed again within a few µs of the end of the pulse and in general data could be taken 10 µs after a transmitter pulse had ended. The pulses from the two waveform generators were combined and amplified

by an Acoustic Research AR 75A250 power amplifier and the output of the amplifier was monitored across a 10 Ω resistor. It was necessary to place 10 pairs of crossed diodes between the amplifier and transmitter coil to make the noise from the amplifier lower than intrinsic SQUID noise. In all experiments the spectrometer sensitivity was dominated by the intrinsic noise of the SQUID which was white over the frequency range of interest. The output of the SQUID electronics was recorded by a Tektronix 430 digital storage oscilloscope, triggered by the DS535. Signals were measured directly, without mixing down. In all cases it was necessary to subtract a background in the time domain, taken with the NMR signal detuned to lie at the first minimum in the power spectrum of the transmitter pulse. In this way spurious magneto-acoustic resonances could be removed. All the pulse sequencing and data acquisition were controlled by a PC running LabVIEW.

4.4.1 The NMR Magnet

The static B_0 field is produced by a superconducting solenoid magnet operating as part of a persisted superconducting circuit. The circuit is formed from two lengths of superconducting wire from the same spool; one length forming the magnet coil and the other the persistent switch. The two wire lengths were joined using spot-welds, heatsunk at the pot, which provides a superconducting connection with $I_c \approx 2$A.

The magnet coil is wound on an 80 mm long OFHC copper former with a 31 mm outer diameter and 30 mm bore, designed to fit inside a cylindrical Nb shield, 1 mm thick with a 35 mm bore. The magnet coil consists of two layer of superconducting wire with (724) turns on each. The wire used was NbTi, $d = 71$ μm, clad with CuNi, $d = 81$ μm, with Formvar, $d = 106$ μm insulation from SuperCon inc. The room

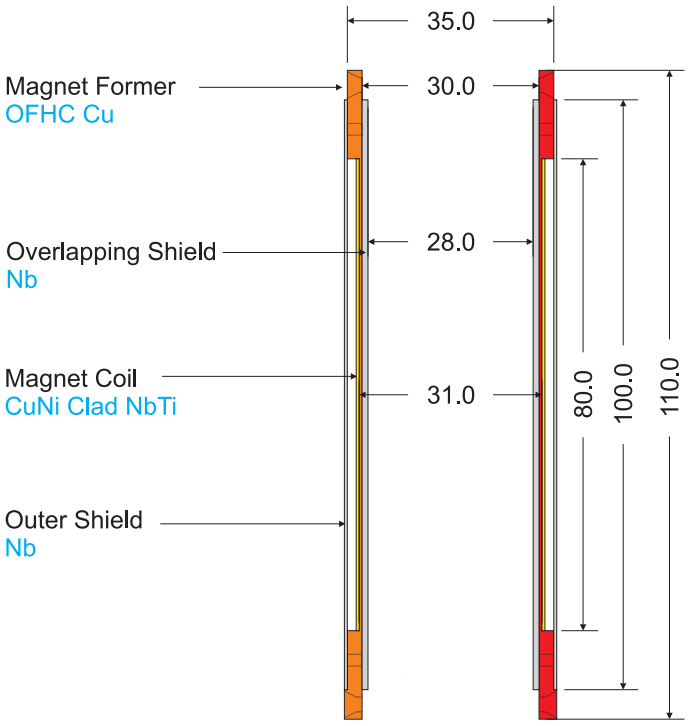

Figure 4.13: A Scale diagram of the compact NMR Magnet and former

temperature resistance of the magnet coil is 16.44 kΩ given in table 4.1.

The field current ratio and the homogeneity of an ideal magnet have been calculated using the Helsinki magnet program [38] giving $(B_0/I)_{\mathrm{th}} = 4.62\,\mathrm{mT\,A^{-1}}$ and $\Delta B/B_0 = 400$ ppm, shown in figure 4.14. B_0/I was determined experimentally by the Larmor frequency of ^{3}He to be $3.806\,\mathrm{mT\,A^{-1}}$. For frequency independent motion the magnet homogeneity $\Delta B/B_0$ can be determined from the NMR data using equation 4.2 where;

$$\frac{1}{T_2^*} = \frac{1}{T_2} + \omega_0 \frac{\Delta B}{B_0} \tag{4.2}$$

$\Delta B/B_0$ has been calculated in section 7.3.1 for the pure ^{3}He experiment as 267 *ppm* and from spin-echo measurements for the ^{4}He preplated experiment in section 7.4.2 as (367.6 ± 6.9) ppm. Between the two experimental runs attempts were made to

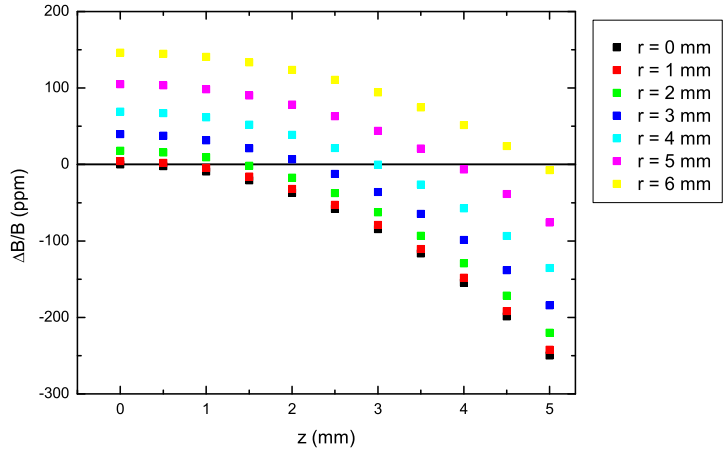

Figure 4.14: Theoretical homogeneity profile of the static field NMR magnet produced using the Helsinki magnet program. Here z and r are the distances from the centre of the magnet in the axial direction and radial directions respectively.

reduce the magnitude of transient responses to transmitter pulses by improving the grounding of the overlapping shield, section 4.4.2. This had a detrimental affect on the magnet homogeneity, the reason for which is not fully understood.

The magnet is operated in persistent mode and a superconducting persistent switch is used to allow current to be injected into the magnet. This consists of 16 turns of superconducting wire with a normal metal cladding wound around a 470 Ω resistor and potted into a PTFE cylinder using Stycast 1266. Below T_c the switch is superconducting and the current in the loop is constant. The resistor is used to heat the switch above T_c where is has a finite resistance, allowing current to be driven into the magnet circuit.

The persistent switch for the magnet circuit is located in the helium bath which makes persisting the field more rapid than if it were located in the IVC, but necessitates a superconducting feedthrough for the magnet wires. The construction

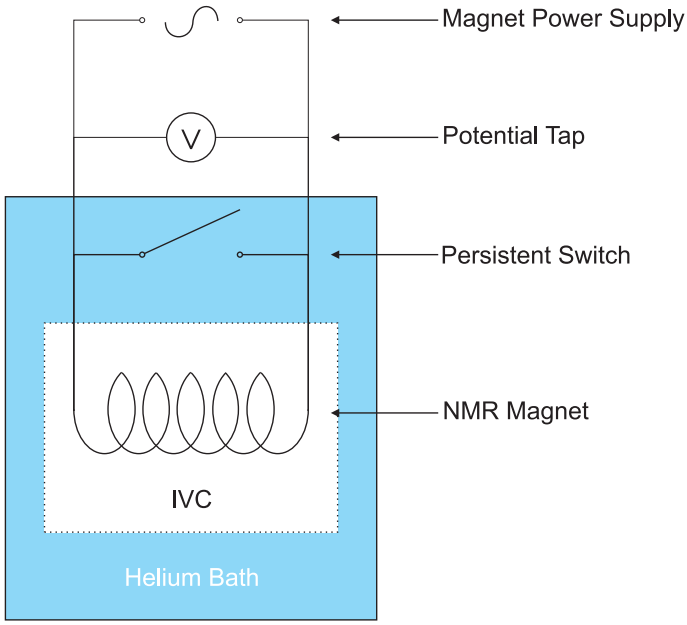

Figure 4.15: A Schematic diagram of the persistent current superconducting magnet circuit

of the feedthrough was similar to the method described in White [39]. A cap was machined from a mixture of Stycast 2850 FT and 1266 with four feedthrough holes drilled into the top. The leads for the chosen persistent switch were twisted to make a pair long enough to position the switch on the top of the IVC then the Formvar insulation was removed from the wires in the region where they would pass though the cap using nitric acid. A single wire was threaded though each hole in the cap and a layer of similar Stycast was applied to the top. When the Stycast was set, lengths of PTFE sleeve were placed around the exposed lengths of wire to prevent electrical shorts. The cap was glued with Stycast onto a thinned down stainless steel tube on the top of the IVC.

The superconducting spot-welds connecting the persistent switch to the magnet are heatsunk directly to the pot in an attempt to make them as robust as possible and maximise T_c. A critical current of $I_c \approx 2$ A has been observed for similar spot-welds.

The critical current for our circuit was not tested, but a current of 2 A was routinely used.

4.4.2 Overlapping Shield

An open-ended cylindrical shield of overlapping niobium foil [40] is inserted between the transmitter coil and the OFHC copper magnet former. This was made by rolling up a long sheet of Nb around a former using a layer of Kapton to prevent electrical conduction between layers. Due to the boundary conditions the shielding factors perpendicular to the axis of the tube is similar to that of a complete superconducting cylinder. The main purpose of the cylinder is to prevent currents circulating in the magnet former following transmitter pulses. However it has the dual benefit of improving the field homogeneity at the centre of the magnet. The presence of the shield does suppress the magnitude of the transmitter pulses and this was taken into account whilst calibrating the RF pulse lengths, however it is not included in the Helsinki magnet program [38].

4.4.3 The Transmitter Coil

As the sensitivity of the SQUID systems increases emergent noise sources become increasingly important. The transmitter coil was designed to minimise the noise produced by NMR pulses, developing the ideas described in the thesis of Köerber [41].

In his study two main issues arose. Following the transmitter pulses eddy currents

are induced in the magnet former which are observed as low frequency transient fields and picked up by the SQUID. The magnitude of the transient response is much greater than the signal size in all of the work outlined here. This has been addressed by the addition of an open diamagnetic cylinder, as described in section 4.4.2, and also by digital filtering described in section 7.2.

Transmitter pulses can create mechanical vibrations at the Larmor frequency, producing an acoustic response. This is inferred from the coherent resonance spikes observed in the frequency domain around the Larmor frequency. To minimise the coupling of the resonances from the transmitter to receiver coils in this experiment the transmitter former is mechanically separated from the magnet and receiver formers and clamped rigidly to one endcap of the coil set assembly. This can be seen in figure 4.12, and greatly reduces the magnitude of the resonance spikes compared to tightly fitting coil sets.

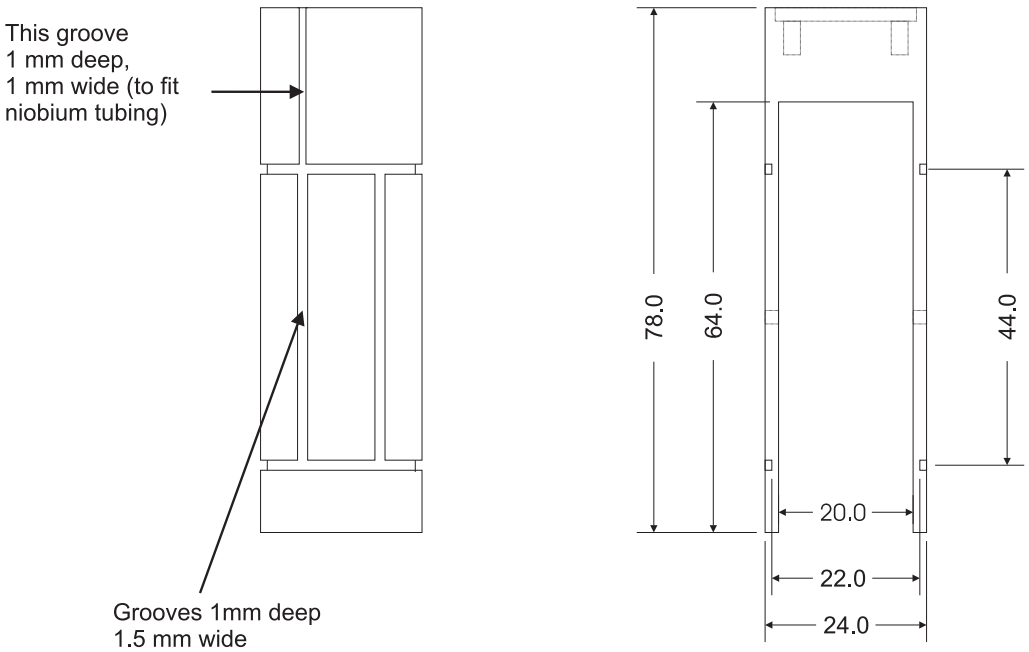

Figure 4.16: A technical drawing of the Kel-F transmitter coil showing relevant dimensions.

The cylindrical Kel-F transmitter former, as shown in figure 4.16, was machined with an Inner Diameter, ID = 20 mm and an Outer Diameter, OD = 24 mm. Optimum homogeneity of a saddle coil is achieved if the angular width of the coil is 120° and the length of the coil, $2g$, is twice the diameter, a [42] and hence the length of this coil was chosen to be 44 mm. The former was patterned with flat recessed guides for the coil to be wound in, with a width of 1.5 mm and a depth of 1 mm. The transmitter coil was wound with $N = 15$ turns of superconducting wire on each side. The wire used was the same as used for the static field magnet in 4.4.1.

If we make the approximation that the coil is made up of two superconducting rectangles of wire, the inductance of a single loop can be calculated by [43]:

$$\frac{L}{N^2} = 2 \times 10^{-7} \left(\ln \frac{2l}{\rho} - \alpha \right) \tag{4.3}$$

Where l is the perimeter of the loop, ρ is the radius of the wire used and $\alpha = 2.855$ is a geometric constant determined by the ratio of the sides of the rectangular coil. This gave a predicted inductance value of 64.1 μH. In free space the inductance of the coil was measured to be 51.8 μH by using the coil as the inductive source in an L-C circuit for a range of calibrated capacitances and measuring the resonant frequencies using a vector impedance meter. The inductance was measured again when the coil was located in the NMR coil set and was found to be reduced to 36.2 μH by the presence of the superconducting shield.

The field-current ratio $(B/I)^{\text{th}}$ for a field at the centre of a saddle coil in free space can be calculated using;

$$\left(\frac{B}{I} \right)^{\text{th}} = \frac{\sqrt{3}\mu_0 N}{\pi} \left(\frac{ag}{(a^2+g^2)^{\frac{3}{2}}} + \frac{g}{a(a^2+g^2)^{\frac{1}{2}}} \right) \tag{4.4}$$

For this coil $(B/I)^{\text{th}} = 1.11\,\text{mT}\,\text{A}^{-1}$. The actual magnitude of the produced field is suppressed due to screening currents produced by the overlapping shield.

4.4.4 The Flux Transformer Input Circuit

Flux is coupled from the cell to the remotely mounted SQUID by a superconducting flux transformer. A simple flux transformer consists of the receiver coil and the SQUID input coil connected by superconducting wire. This device works on the principle of conservation of flux through a superconducting loop. A signal flux, $\delta\phi_{\text{s}}$, threading the receiver coil will induce a screening current, I, in the circuit such that the flux linkages gives

$$\delta\Phi_{\text{s}} + \delta\Phi_{\text{r}} + \delta\Phi_{\text{i}} = 0 \tag{4.5}$$

Where subscripts r and i denote the receiver and input coils, and $\Phi = N\phi$ where N is the number of turns on the coil. Hence;

$$\delta\Phi_{\text{s}} - (L_{\text{r}} + L_{\text{i}})I = 0 \tag{4.6}$$

The flux coupled to the SQUID is given by $\Phi_{\text{SQ}} = M_{\text{i}}I$ where M_{i} is the mutual inductance between the SQUID and the input coil, so the gain of the flux transformer is;

$$\frac{\Phi_{\text{SQ}}}{\Phi_{\text{s}}} = \frac{M_{\text{i}}}{(L_{\text{r}} + L_{\text{i}})} \tag{4.7}$$

This is optimised when $L_{\text{r}} = L_{\text{i}}$. The receiver coil was designed to be matched to the input coil of the C2 SQUID Array, section 5.5, with $L_{\text{i}} = 1.48\,\mu\text{H}$.

The flux transformer used in this experiment also includes a Q-spoiler, an integrated

current limiter consisting of a series array of hysteretic SQUIDs. The array is resistive for high currents and superconducting for low currents. It therefore limits the current in the input circuit caused by cross-coupling from the transmitter pulse and shortens the spectrometer recovery time.

A Quantum Design Q-Spoiler was used in conjunction with the C2 SQUID Array. This was mounted on the SQUID carrier inside the Nb shield. This had normal state resistance $R_{\mathrm{N}} = 405.8\,\Omega$ and the critical current I_{c} was tunable between 20 and $40\,\mu\mathrm{A}$ depending on bias position, controlled by modulation coils. The maximum recommended current in the input coil is $950\,\mu\mathrm{A}$ so the SQUID is suitably protected. The Q-spoiler also reduces the dead time before data acquisition. For the C5 SQUID a suitable Q-spoiler device is fabricated on chip removing the need for an external device. This reduces the number of superconducting joints necessary in the input circuit making the device more reliable on thermal cycling.

4.4.5 The Receiver Coil

The cylindrical Kel-F receiver former, as shown in figure 4.17, has an OD of 17 mm and an ID of 14 mm. It is designed to be a close fit to the cell to optimise the flux threading the coil. It is secured rigidly on an OFHC Copper base such that the coil former is geometrically perpendicular to the transmitter and patterned with a guide for a saddle coil similar to that of the transmitter. Again the angular width of the coil is 120° and the height of the coil was chosen to be 15 mm, less than twice the diameter of the coil.

The receiver coil is wound from NbTi superconducting bare wire, $d = 101.6\,\mu\mathrm{m} =$

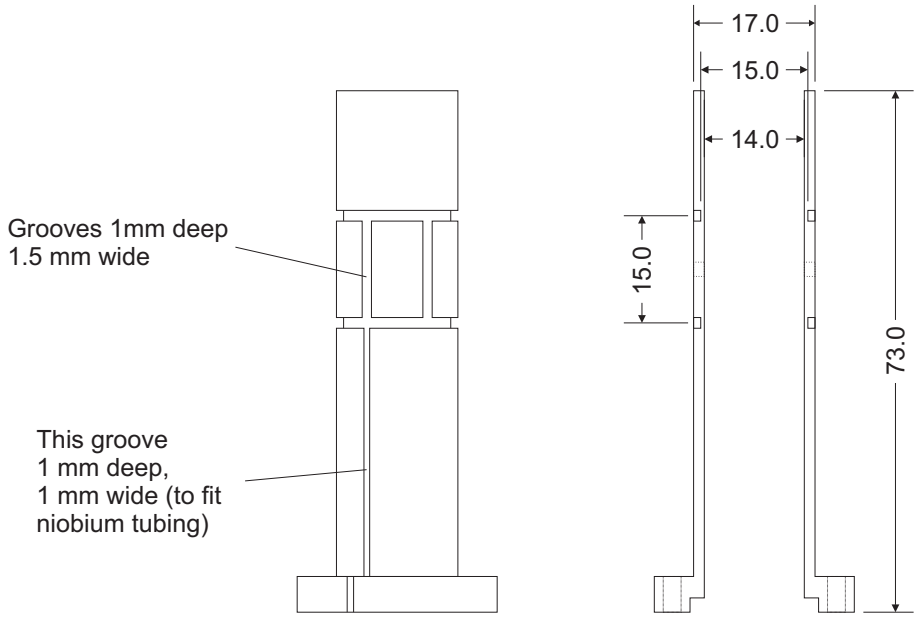

Figure 4.17: A technical drawing of the Kel-F receiver coil showing relevant dimensions.

0.004″ insulated with Formvar, $d = 127\,\mu\text{m} = 0.005''$. The receiver coil forms part of a superconducting circuit, so it was not necessary to use CuNi clad wire which can be soldered to. Also Johnson noise generated within the normal metal cladding of wire clad has experimentally been found to increase the measurement noise. The diameter of the saddle coils is 15 mm and the height of the coil is 15 mm.

The coil inductance is calculated using equation 4.3 for $l = 53\,\text{mm}$ and $\rho = 50.8\,\mu\text{m}$ to be $L = 1.624\,\mu\text{H}$ for 4 turns on each side of the saddle coil. The inductance was measured by cooling the coil to 4.2 K and using it as the inductance in a resonant LC circuit. The measured inductance was $L_\text{r} = 2.16\,\mu\text{H}$. The field at the centre of the coil is calculated by equation 4.4 as $(B/I)^\text{th} = 384\,\mu\text{T/A}$.

4.4.6 The Sample Cell

The sample cell design is shown in figure 4.18. It is machined from a Stycast 1266 cylinder and was designed to be a tight fit inside the NMR receiver coil. The inner sample chamber is a cylinder of height 10 mm and diameter 12 mm giving a volume $V_s = 1.131\,\mathrm{cm}^3$. The fill line is formed by setting the Stycast around a greased 31 SWG piano wire of diameter 0.3 mm. The cell is mounted on a brass base which forms part of the coil set assembly. A stainless steel fill line is glued with Stycast to the piano wire fill line at the base of the cell. At the other end of this fill line a brass bush is hard soldered, to connect with the main gas handling system. An overview of the cell positioned inside the coil set assembly is shown in figure 4.12.

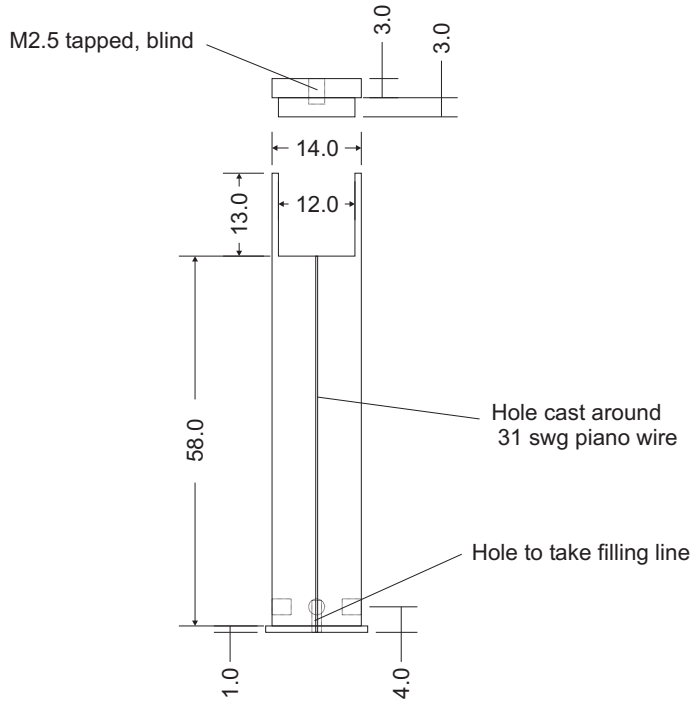

Figure 4.18: The Stycast sample cell with piano wire fill line. The cell volume is $1.13\,\mathrm{cm}^3$

4.4.7 Sample Preparation and Loading the Cell

The MCM-41 powder was baked out under vacuum in a quartz glass tube for 25 hours at 500 °C using a Gallenkamp oven. An indium o-ring was used to make a glass-to-metal seal between the bake out tube at the open end and a metal clamp which connects to a Swagelok valve. Quartz glass wool was placed inside the tube between the powder and the valve to ensure that the valve seat remained clean. The sample was pumped out through a low impedance LN_2 cold trap using a turbomolecular pump.

Prior to assembly the cell and lid were cleaned ultrasonically using ethanol. A disc of Whatman Grade GF/F filter paper [44] was placed at the bottom of the cell to prevent any of the sample powder leaving the cell through the fill line. This was baked under vacuum prior to assembly and held in place by a tight fitting Stycast 1266 ring.

The powder was transfered from the bake out tube to the cell in side a glove bag with a dry ^{4}He atmosphere. The gas handling system for the glove bag contained an activated charcoal cold trap at LN2 temperature and allowed the bag to be filled and pumped cleanly. The glove bag was flushed with ^{4}He and pumped seven times before opening the bake out tube. A diamond tipped blade was used to score around the quartz glass tube enabling it to be snapped cleanly whilst holding it with two wooden blocks. The cell was filled using a spatula and compacted gently using a PTFE rod machined to be a good fit to the cell bore. The sealing surface at the top of the cell was cleaned with a cotton bud to ensure that it was free from powder before Stycast 1266 was applied with a syringe and sharped q-tip. After positioning the cell lid a 50 g weight was placed onto the top to ensure that it set in the correct

position. Once cured a neoprene cap was placed over the fill line bush so that the powder remained in a ^{4}He atmosphere when removed from the glove bag.

Exposing the sample to atmosphere briefly whilst attaching the cell to the cryostat was unavoidable. To minimise this exposure a neoprene cap was chosen to seal the cell fill line. This was chosen over a soldered cap as it allows the inner surface of the bush and the cryostat fill line to be prepared for soldering in advance. The neoprene cap was cooled with LN_2 to allow clean machining.

Prior to making the solder connection ^{4}He was blown through the cryostat fill line. This was stopped prior to soldering to ensure the quality of the solder joint. The cell was pumped immediately using a turbomolecular pump with a dry bellows backing pump.

From measurements of the mass of the sample container before and after loading the cell we estimate that the cell contains 246 mg of MCM-41 powder. This measurement was made using a Stanton Unimatic CL41 single pan balance and is an upper estimate as a small amount of the sample was lost while cleaning the surfaces of the cell prior to applying the Stycast and remained on tools after the filling procedure.

Chapter 5

The DC SQUID Sensor

Superconducting QUantum Interferance Devices, SQUIDs, are presently the most sensitive detectors of magnetic flux for NMR applications. The detection method for the NMR experiments carried out in this work utilises a DC SQUID as a cryogenic sensor, operated as part of a Flux-Locked Loop, FLL. In this arrangement the SQUID is used as a null detector using the Direct readout Offset Integration Technique (DOIT) proposed by Drung [45]. This section contains a brief overview of the SQUID and readout method and then focuses on the particular SQUIDs used for the NMR experiments and techniques used to enhance the output signal. For the first NMR experiment, where ^{3}He was adsorbed directly onto the substrate, a C2 16-SQUID linear array was used. This was upgraded to a C5 single SQUID with APF for the preplated experiment, giving an order of magnitude improvement energy sensitivity. For a detailed discussion of SQUID devices and applications see for example [45–47].

5.1 A Brief Introduction to SQUIDs

A DC SQUID is formed of two identical Josephson Junctions connected in parallel forming a superconducting loop. The flux threading a superconducting loop is quantised in units of $h/2e = \phi_0$, the flux quantum. When an external field is applied a screening current is set up in the loop to oppose the field such that the total flux threading the loop remains $n\phi_0$ where n is an integer. When the external field exceeds $(n \pm 1/2)\,\phi_0$ it becomes energetically favourable to allow an additional ϕ_0 to thread the SQUID loop causing the screening current to reverse.

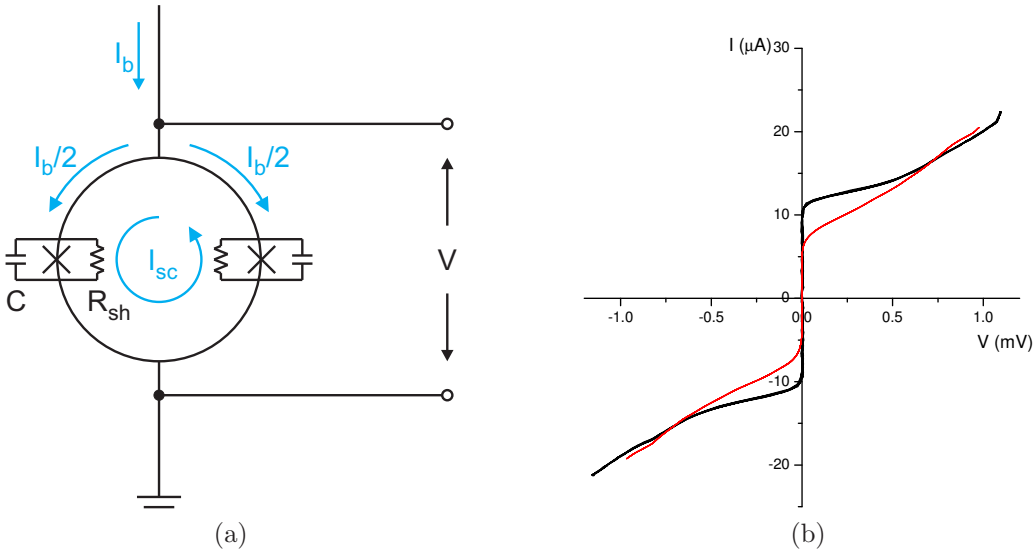

(a) (b)

Figure 5.1: (a) SQUID schematic. (b)SQUID $I-V$ characteristic of the c2 SQUID Array where $I_{\mathrm{c,max}} = 11.5\,\mu\mathrm{A}$, $I_{\mathrm{c,min}} = 7.3\,\mu\mathrm{A}$. The gradient $\delta V/\delta I$ at the working point is the dynamic resistance, R_{dyn}

The total current in each arm of the the SQUID loop is given by $I = I_{\mathrm{b}} \pm I_{\mathrm{sc}}$ where I_{b} is the applied bias current and $\pm I_{\mathrm{sc}}$ is the screening current. The critical current will be exceeded when $I_{\mathrm{c}} < I_{\mathrm{b}} + |I_{\mathrm{sc}}|$. Hence the critical current observed across the SQUID will be modulated by the external flux threading the SQUID loop. This results in an $I-V$ characteristic as shown in figure 5.1(b). This shows the maxi-

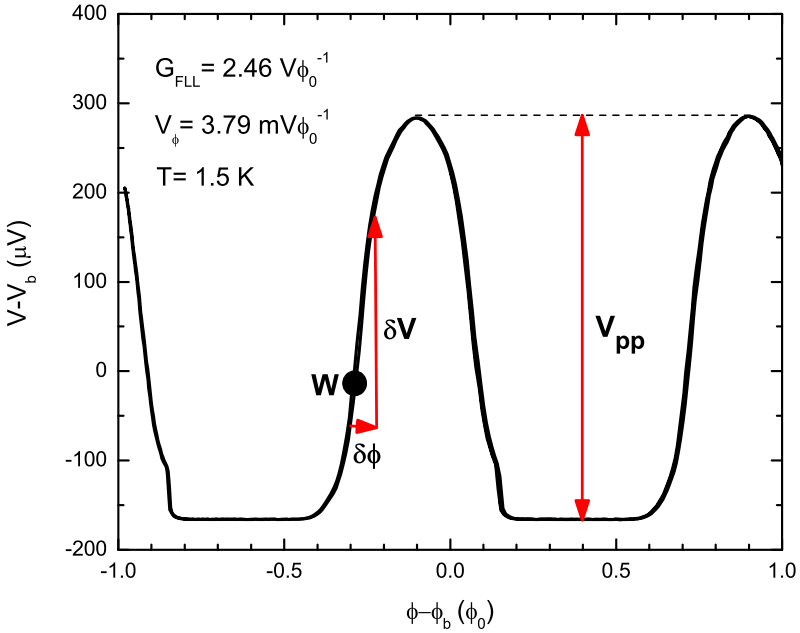

Figure 5.2: SQUID $V - \phi$ characteristic for the C2 SQUID array with optimal bias positions. W is the FLL working point.

mum and minimum critical currents for the C2 SQUID Array. The intrinsic $I - V$ characteristic is hysteretic but this can be suppressed by resistively and capacitively shunting the Josephson junctions. Clarke [47] shows that the characteristic will not be hysteretic provided that

$$\beta_c \equiv 2\pi I_0 R_{sh}^2 C/\phi_0 \leq 1 \tag{5.1}$$

For a bias current $I_b > I_c$ a finite voltage will be observed across the SQUID given by $V = I_n R_{dyn}$, where I_n is the normal component of the current and R_{dyn} is the dynamic resistance of the SQUID. If this bias current is held constant then I_n will vary periodically with field, giving rise to a $V - \phi$ characteristic as shown in figure 5.2.

The $V - \phi$ characteristic is linear to good approximation about the points of inflec-

tion. In the small signal regime the SQUID intrinsically becomes a linear flux to voltage converter. We define a working point, W, as the steepest part of the $V - \phi$ characteristic. By applying a voltage bias, v_b, and flux bias, ϕ_b, to the SQUID we can use the SQUID as a sensitive flux to voltage converter in the small signal regime, where $\phi \ll \phi_0$. The gain will be given by the transfer function $V_\phi = \delta V/\delta\phi$ at the working point, and the modulation depth V_{pp} is the voltage swing.

5.2 Flux-Locked Loop Electronics

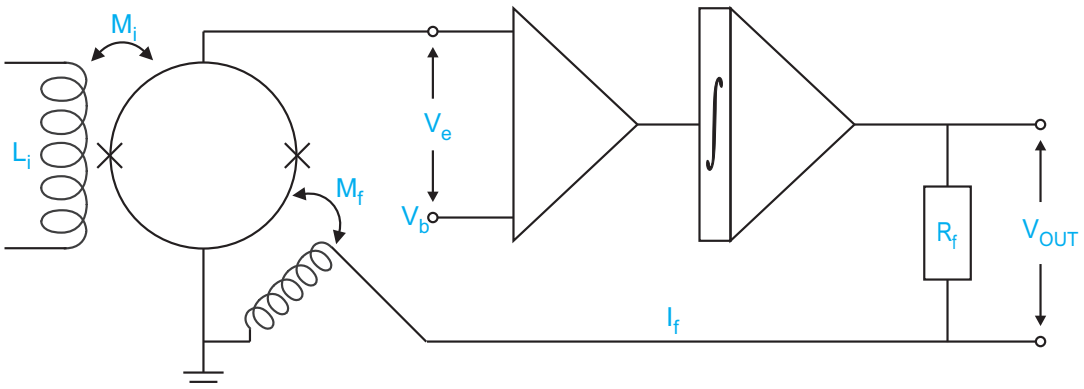

Figure 5.3: A schematic diagram of the Flux-Locked Loop feedback electronics.

The linear flux region can be can be extended over a far greater range by operating the SQUID as part of a Flux-Locked Loop (FLL). We implement a Direct Offset Integration Technique (DOIT) FLL scheme after Drung [45]. This is a negative feedback system where the SQUID is used as a null detector. The system used is commercially available through Magnicon GmBH [37] and is fully computer controlled using LabVIEW derived software. A schematic of the system is shown in figure 5.3. Here the working point of the SQUID is chosen by adjusting I_b such that a $V - \phi$ characteristic with the greatest V_ϕ is achieved and setting V_b to the steepest part of the curve.

The voltage developed across the SQUID is coupled directly to a low noise differential amplifier at room temperature generating an error voltage, $V_{\rm e} \propto V - V_{\rm b}$. $V_{\rm e}$ is amplified further by a single pole integrator. The output of the room temperature electronics is fed back to the SQUID by a feedback coil, with $L_{\rm f}$ and a mutual inductance to the SQUID $M_{\rm f}$, through a resistor $R_{\rm f}$. The flux coupled to the SQUID directly opposes the flux coupled from the input coil such that $\Delta\phi_{\rm f} = -\Delta\phi_{\rm SQ}$. The current in the feedback coil necessary to produce the feedback flux is $\Delta I_{\rm f} = \Delta\phi_{\rm f}/M_{\rm f}$, which generates a potential $\Delta V_{\rm OUT} = R_{\rm f}\Delta I_{\rm f} = R_{\rm f}\Delta\phi_{\rm f}/M_{\rm f}$. The output voltage, $V_{\rm OUT}$, is directly proportional to the flux threading the SQUID within the device bandwidth and the FLL gain is given by $G_{\rm FLL} = R_{\rm f}/M_{\rm f}$. The FLL gain is independent of the SQUID temperature making this method of detection robust to temperature fluctuations and the bandwidth is typically a few MHz.

5.3 Flux-Locked Loop Noise

The noise in the detection system consists of contributions from the SQUID and from the room temperature electronics. The total effective FLL flux noise power spectral density per unit bandwidth can be expressed as

$$\begin{aligned} S_\phi &= S_{\phi,\rm SQ} + S_{\phi,\rm amp,V} + S_{\phi,\rm amp,I} \\ &= S_{\phi,\rm SQ} + \frac{V_{\rm N,amp}^2}{V_\phi^2} + \frac{I_{\rm N,amp}^2 R_{\rm dyn}^2}{V_\phi^2} \end{aligned} \tag{5.2}$$

where $S_{\phi,\rm SQ}$ is the SQUID flux noise power, $V_{\rm N,amp}^2$ and $I_{\rm N,amp}^2$ are the voltage and current noise powers associated with the room temperature electronics. The units of S_ϕ are $\rm Wb^2\,Hz^{-1}$, however it is often expressed in terms of the magnetic flux

quantum $\phi_0 = 2.068 \times 10^{-15}$ Wb as ϕ_0^2/Hz. We use the commercially available SEL-1 FLL electronics from Magnicon. These have $V_{\mathrm{N,amp}} = 0.4$ nVHz$^{-1/2}$ and $I_{\mathrm{N,amp}} = 4$ pAHz$^{-1/2}$. In order to couple the SQUID directly to the FLL electronics we need to amplify the signal and the noise contributions from the SQUID so that the $S_\phi \approx S_{\phi,\mathrm{SQ}}$, achieved by maximising V_ϕ.

Simulations of $S_{\phi,\mathrm{SQ}}$ [48] show that it is approximately four times higher than the expected Johnson noise associated with R_{sh}, hence can be expressed as

$$S_{\phi,\mathrm{SQ}} = \frac{16 k_{\mathrm{B}} T L^2}{R_{\mathrm{sh}}} \tag{5.3}$$

where G_{FLL} is the closed flux locked loop gain. The SQUID noise is approximately proportional to the Johnson noise in the resistive shunts, and can be reduced in a similar manor. R_{sh} can be minimised but must be low enough to satisfy inequality 5.1 to prevent hysteresis . We can reduce $S_{\phi,\mathrm{SQ}}$ by cooling the SQUID which also has the effect of increasing I_{c} and V_ϕ.

One figure of merit for a SQUID is the energy sensitivity, ε, which has units of J s and is usually expressed in units of h given by

$$\varepsilon = \frac{S_\phi}{2L_{\mathrm{s}}} \tag{5.4}$$

Where L_{s} is the SQUID inductance in Wb. For a SQUID operated with a broadband input circuit the appropriate unit is the coupled energy sensitivity, $\varepsilon_{\mathrm{c}} = \varepsilon/k^2$ where $k = M_{\mathrm{i}}/\sqrt{L_{\mathrm{i}} L_{\mathrm{s}}}$ and M_i is the mutual inductance between the SQUID and the input coil, hence

$$\varepsilon_{\mathrm{c}} = \frac{L_{\mathrm{i}} S_\phi}{2M_{\mathrm{i}}^2} \tag{5.5}$$

5.4 SQUIDs Used

Two different SQUID sensors have been used for the NMR experiments. ε was similar for each device, however the improved coupling of the C5 device resulted in an order of magnitude improvement in ε_c. This is equivelent to an order of magnitude reduction in NMR averaging time to achieve the same signal-to-noise ratio.

5.5 C2 SQUID Array

A second generation SQUID from PTB, S/N: C208-K25-XL16MOA, was used for the initial NMR experiment without ^{4}He preplating. This device is described in greater detail in [36]. It consisted of a linear array of 16 identical SQUIDs, each with the same M_i and M_f. In this configuration the array operates as a single SQUID with an enhanced $V-\phi$ characteristic. The resultant V_ϕ and S_ϕ are 16 times greater than for an individual SQUID but with no reduction of the linear range, $\Delta\phi$. The shunt resistors feature large area fins to aid in cooling, as can be seen in figure 5.4a. This particular device was optimised to be operated at 1.5 K.

The choice of control wires used between the SQUID and the FLL electronics at room temperature can significantly effect the performance of the feedback system. Lower resistance wire in the feedback lines can decrease the delay in the transmission lines increasing the FLL bandwidth and aid stability. Here two twisted pairs of copper wire connect the FFL electronics at the top of the cryostat to a junction box at the 4 K plate. To minimise the heatleak CuNi clad NbTi superconducting wire was

used from the 4 K plate to the SQUID, mounted at the pot temperature. A length of uninsulated copper wire was used to heatsink the Stycast SQUID carrier to the SQUID plate. This was fed through the Nb shield and secured to the SQUID carrier with copper tape.

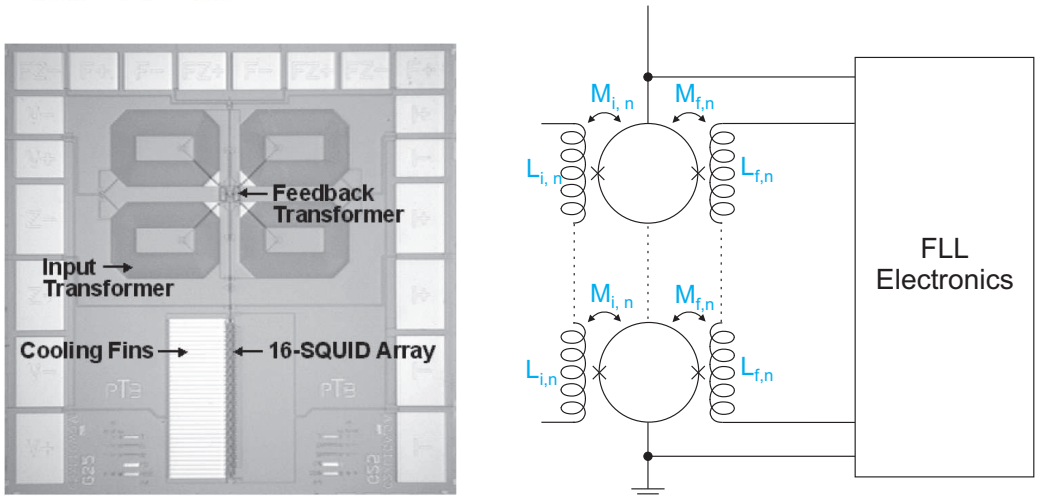

(a) (b)

Figure 5.4: (a)SQUID Array photograph (b) SQUID Array schematic. Images from [36]

In this brief discussion of the array noise the subscript n will be used to denote an individual SQUID in an array of N SQUIDs. For a single SQUID device we usually find that $V^2_{\mathrm{N,amp}} \gg I^2_{\mathrm{N,amp}} R^2_{\mathrm{dyn}}$ allowing the amplifier current noise to be neglected. Since for a SQUID array $R_{\mathrm{dyn}} = N R_{\mathrm{dyn,n}}$ the amplifier current noise becomes significant. The C2 array had $\mathrm{R_{dyn}} = 87\,\Omega$ and $V_\phi = 3.79\ \mathrm{mV}\phi_0^{-1}$ at the working point. From this we calculate the FLL electronics contribution to the total noise to be $S_{\phi,\mathrm{AMP}} = S_{\phi,\mathrm{amp,I}} + S_{\phi,\mathrm{amp,V}} = 1.96 \times 10^{-14}\ \phi_0^2\mathrm{Hz}^{-1}$ for a SQUID cooled to 1.5 K. At this temperature the total system noise measured at 100 kHz using a SR760 Spectrum analyser was $S_\phi = 7.33 \times 10^{-14}\ \phi_0^2\mathrm{Hz}^{-1}$ equivalent to $\varepsilon_\mathrm{c} = 296$ h. The intrinsic SQUID contribution was $S_\phi - S_{\phi,\mathrm{AMP}} = S_{\phi,\mathrm{SQ}} = 5.37 \times 10^{-14}\ \phi_0^2\mathrm{Hz}^{-1}$ and the associated energy sensitivity 216 h. In principle we could gain an improvement

Table 5.1: Summary of C208 SQUID Parameters

Input coil inductance, L_i	1.48	μH
Input coil-SQUID mutual inductance, M_i	1.089	nH
V_ϕ at the working point	3.791	mV/ϕ_0
FLL gain, G_FLL	2.46	V/ϕ_0
Flux transformer gain $\phi_\mathrm{SQ}/\phi_\mathrm{p}$	2.992	$\times 10^{-4}$
$S_\phi(1.5\,\mathrm{K})$	310	nϕ_0Hz$^{-1/2}$
$\varepsilon(1.5\,\mathrm{K})$	34.4	h
$\varepsilon_\mathrm{c}(1.5\,\mathrm{K})$	296	h
Coupling constant k	0.34	

by changing to the latest XXF FLL electronics from Magnicon [37] which have lower current and voltage noise.

5.6 C5 SQUID with APF

For the ^{4}He preplated experiment we upgraded the SQUID with one that had an improved input coil coupling and coupled energy sensitivity. This was a C5XXL1W type SQUID, H46 from wafer C504. It was a single SQUID which used an Additional Positive Feedback,APF, technique to enhance the $V-\phi$ characteristic in order to be read out directly using room temperature electronics. Here an additional flux is coupled to the SQUID in order to skew the $V-\phi$ making it non-symmetric. A schematic of an APF system is shown in figure 5.5(a). This system consists of an additional resistance and inductance connected in series, in parallel to the SQUID.

It is intuitive to consider three currents when describing the APF action, I_c the superconducting component of the current across the SQUID, I_N, the normal component of the current across the SQUID and I_{APF}, the current through the APF circuit. Now if we are in a region of the $V-\phi$ characteristic where V increases

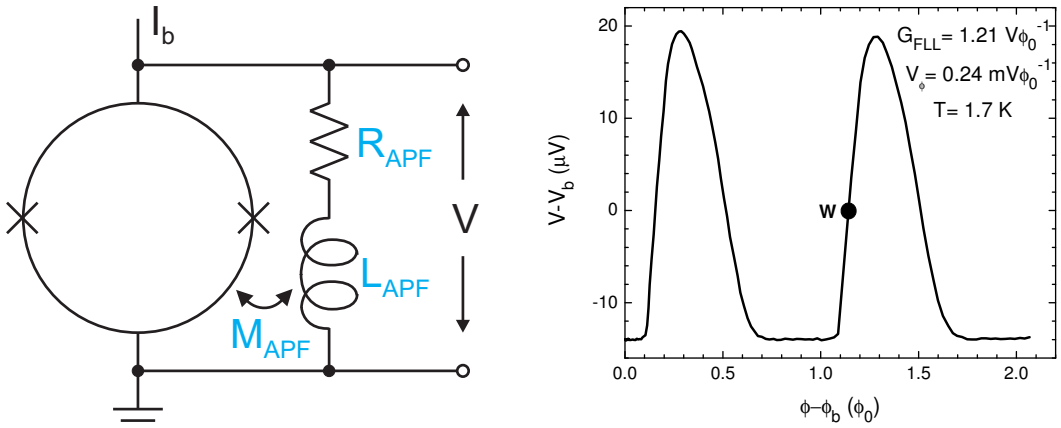

(a) (b)

Figure 5.5: (a) C5 APF SQUID schematic. (b)APF $V - \phi$ characteristic for the APF SQUID

with ϕ then an increase in ϕ will decrease I_c. This will increase the current I_{APF} passing through L_{APF}, and the flux threading the SQUID for a given current in the feedback coil, ϕ_f, will be enhanced. Similarly if we are on the (other slope) of the $V - \phi$ then a positive change in ϕ will decrease V, increasing I_c and subsequently reducing I_{APF} and hence ϕ_{APF}. The decrease in ϕ_{APF} will partly compensate/damp the increase in ϕ and the slope of $V - \phi$. The resultant skewed $V - \phi$ characteristic for this APF SQUID is shown in figure 5.5(a).

The wiring scheme was modified to aid in cooling the SQUID chip. Similar copper wiring was used from room temperature to the 4 K junction box, although 7 wires were now used to support the future use of 2-stage SQUIDs on this probe. Superconducting wire was used from 4 K to a further junction box on the SQUID plate. Copper wire was used from the junction box to the SQUID. The SQUID was also fabricated with a cooling plane. This was connected by a wirebond to a printed copper 'C'-shaped thermal contact on the SQUID carrier and is used to aid cooling the SQUID below 4 K.

Table 5.2: Summary of C504 SQUID Parameters

Input coil inductance, L_i	1.8	μH
Input coil-SQUID mutual inductance, M_i	9.23	nH
V_ϕ at the working point	0.31	m$\mathrm{V}\phi_0^{-1}$
FLL gain, G_FLL	1.217	$\mathrm{V}\phi_0^{-1}$
Flux transformer gain $\phi_\mathrm{SQ}/\phi_\mathrm{p}$	2.33	$\times 10^{-3}$
$S_\phi(1.5\,\mathrm{K})$	656	n$\phi_0\mathrm{Hz}^{-1/2}$
$\varepsilon_\mathrm{c}(1.5\,\mathrm{K})$	29.3	h

For this device we measured $S_\phi^{1/2} = 1.23\ \ \phi_0/\sqrt{\mathrm{Hz}}$ at 100 kHz and 4.3 K, giving $\varepsilon_\mathrm{c} = 103\,\mathrm{h}$. This was reduced to $S_\phi^{1/2} = 656\,\mathrm{n}\phi_0/\sqrt{\mathrm{Hz}}$ at the pot temperature of 1.5 K, which gives $\varepsilon_c = 29.3\,\mathrm{h}$. This suggests that the SQUID is cooling and that the noise is dominated by the intrinsic SQUID noise.

5.7 Comparison of C2 SQUID Array and C5 APF SQUID

Optimal flux transfer is achieved in a flux transformer when the pickup and input coil inductances are equal, however a large pickup coil inductance, L_p, is needed to couple sufficient flux from the experimental cell. Both of the SQUIDs used feature a double flux transformer input circuit with a large turns ratio. The C2 generation of SQUIDs from PTB were the first to feature this type of input circuit fabricated on chip which allows a reasonably sized pickup coil to be coupled to a SQUID with optimally low L_S. However for the array to act as a single SQUID the parasitic mutual inductance from the input transformer to the each SQUID in the array must be minimised. This was achieved by positioning the array far away from the input transformer on chip [36]. This resulted in large stray inductances in the interconnect

lines and a lower than expected effective M_i [49]. This constraint is not relevant for the single APF SQUID allowing it to be fabricated close to the input transformer. The resultant M_{i} was 8.5 times higher for the APF SQUID giving a significantly improved ε_{c} with a larger L_{i}.

However there are a number of disadvantages to the APF system. The modulation depth ΔV is reduced over that of a normally operated single SQUID as a fraction of I_b is shunted through the APF components. The linear range $\phi_{\mathrm{Lin}}$is also decreased as the V_ϕ is non-symmetric. Both of these decrease the slew rate. R_{APF} also adds a Johnson noise contribution to the SQUID noise. Therefore the chosen value of R_{APF} is a compromise between Johnson noise and modulation depth.

For both of our SQUID sensors the noise in the detection system is dominated by the intrinsic SQUID Johnson noise and the detector noise was reduced by cooling the SQUIDs below 4 K.

Overall it was found that the C5 APF SQUID was more stable suffering less from flux jumps, however more care was taken to eliminate sources of environmental noise and electronic noise originating from other parts of the detection system when using this SQUID in order to take advantage of the increase in sensitivity which allowed samples with a smaller spin density to be measured.

Chapter 6

Helium Adsorption Experiments

The initial characterisation of our sample was performed by the groups of Chan and Bharat at Penn State [50] and the results of this study are outlined in section 6.2. Here the specific surface area, porosity and average pore diameter were determined.

In section 6.2.1 these are compared with the experimental results from the group of N. Wada At Nagoya University, whose group has performed a systematic study of ^{4}He and isotopic helium mixtures observed on FSM-16 which is structurally similar to MCM-41. Also reported are the results of a theoretical study of ^{4}He adsorbed on a structureless flat substrate using a Worm-Algorithm Monte Carlo simulation by M. Boninsegni. This includes data for the behaviour of a single ^{3}He impurity in such a film.

We have performed our own *in-situ* ^{3}He and ^{4}He vapour pressure measurements to further characterise the system. Initial attempts to characterise the sample by a ^{3}He isotherm at 4.2 K are described in section 6.3. The isothermal compressibilities

of the adsorbed helium were calculated from these results in order to compare the results with those of Wada for a similar substrate and pore diameter [7]. The point B definition of monolayer completion [51] was found to be unsuitable as it gave quantitatively different results at different temperatures which could not be accounted for by atoms entering the vapour phase. The reason for this is not fully understood, but may be due to the geometry of the pores. Spot measurements of the vapour pressure at different substrate temperatures were made at coverages at which NMR data were acquired to obtain the isosteric heat of adsorption. Combining these results with the NMR results of section 7.3 it is inconclusive as to whether the substrate was cooling below 2 K in the absence of a finite vapour pressure.

For the ^{4}He isotherms described in section 6.4 improvements were made to the gas handling system and a sensitive low temperature pressure gauge was added. Detailed vapour pressure measurements were made at temperature between 1.6 K and 10.1 K. These changes greatly improved the sensitivity of our monolayer completion measurement, however repeating the ^{4}He isotherm revealed a ~ 5 % reduction in the surface area. We attributed this to structural instability of the sample on thermal cycling and consequently we cannot reliably comment on the difference in monolayer density for ^{3}He and ^{4}He adatoms. At the highest coverages the film became thick enough to observe bulk like properties where the pressures tended towards the ^{4}He saturated vapour pressure (SVP) value at base temperature which indicates that in this case the cell was cooling adequately.

6.1 Thermodynamic Background to Adsorption

Any composite system consisting of a film and a vapour phase is said to be in thermodynamic equilibrium when the chemical potentials of the two phases, μ_f and μ_v, are equal. It is therefore possible to obtain a large amount of thermodynamic information about the adsorbed phase purely by observing the behaviour of the gas. Some of the useful thermodynamic properties and their relations to the vapour pressure are outlined in this section.

6.1.1 General Isotherm Model

In this section we assume that the gaseous phase is ideal and that the interactions are dominated by a Leonard-Jones 6-12 potential between the substrate atoms and adatoms. Integrating this over a homogeneous, semi-infinite substrate leads to a potential of the form

$$U_{3-9} = \frac{D}{2}\left(\frac{a^9}{r^9} - 3\frac{a^3}{r^3}\right) \tag{6.1}$$

Where D is the characteristic depth of the potential well, and a is the equilibrium spacing given by the position of the well minimum and r is the perpendicular distance between the substrate and adatom. For this analysis we assume a simplified form

$$\mu_{\mathrm{f}}(r) = -\Gamma/r^3 \tag{6.2}$$

valid for distances greater than a where the repulsive forces can be neglected. Here we use $\Gamma = 1100\,\mathrm{K\,\AA}^3$ which is the value for glass [17]. For a film in equilibrium

with an ideal gas we find the chemical potentials

$$\mu_{\mathrm{f}} = \mu_v = -k_{\mathrm{B}}T \ln\left(\frac{k_{\mathrm{B}}T}{p\lambda^3}\right) \tag{6.3}$$

Where $\lambda = \sqrt{h^2/2\pi m k_{\mathrm{B}}T}$ is the thermal de Broglie wavelength, p and T are pressure and temperature. Measuring the pressure gives us relatively direct information about the chemical potential of the film and changes in its thickness. Hence for layer by layer growth from equation 6.2 we expect stepwise decrease in the chemical potential coincident with layer promotion. From equation 6.3 we see that this will be observed as a step change in vapour pressure. This has been observed for other helium systems, see for example vapour pressure isotherms of helium isotopes on grafoil [52]. In general the transitions between isotherm steps are continuous, smoothed out by surface hetrogeniety and the finite temperature of film observed as a knee in the isotherm. The first isotherm step corresponding to monolayer is usually preserved as the binding energy is strong at the surface but higher coverage steps are often lost.

Henry's Law suggests that above this knee we should observe a regime where the pressure increase is proportional to coverage. This has been used by Bretz and others to define layer completion [51]. Using this criterion monolayer completion is often quoted as Point B, where the linear isotherm region begins. Sometimes Point A is also quoted, which is the coverage corresponding to Henry's law extrapolated to zero pressure. These points are shown in figure 6.3(a).

6.1.2 Isothermal Compressibility

A sensitive probe of monolayer completion is the two-dimensional isothermal compressibility, κ_{T}, of the adsorbed film, which is a minimum at layer completion. This method has been used previously to determine layer completion in multilayer helium films for planar [52, 53] substrates and monolayer completion in porous [7] porous substrates. κ_{T} is defined as [54]

$$\kappa_{\mathrm{T}} \equiv -\frac{1}{a}\left(\frac{\partial a}{\partial \phi}\right)_T \tag{6.4}$$

Where $a = 1/n$ is the molecular area, n is the areal density and ϕ is the 2D spreading pressure, the thermodynamic conjugate variable to a. In the low pressure regime κ_{T} is approximately temperature independent [10] which allows a number of vapour pressure isotherms over a range of temperatures to be combined extending the coverage range of this technique. Moving to lower temperatures at higher coverages minimises the fraction of gas atoms in the dead volume. For an ideal 2D film the chemical potential can be expressed as

$$\mathrm{d}\mu_{2\mathrm{D}} = -s\mathrm{d}T + a\mathrm{d}\phi \tag{6.5}$$

where s is the entropy per particle. Hence at constant temperature

$$a = \left(\frac{\partial \mu_{\mathrm{f}}}{\partial \phi}\right)_T \tag{6.6}$$

Substituting equation 6.6 into 6.4 gives

$$\kappa_{\mathrm{T}} = \left(\frac{\partial a}{\partial \mu_{\mathrm{f}}}\right)_T \tag{6.7}$$

If we assume that the vapour is an ideal gas, then by substituting equation 6.3 into 6.7 at constant T and putting $a = A/N$ where A is the adsorption area and N the number of adatoms we get

$$\kappa_{\mathrm{T}} = \frac{A}{N^2 kT} \left(\frac{\partial N}{\partial \ln p} \right)_T \tag{6.8}$$

The adsorption surface area only enters equation 6.8 as a multiplicative factor in the magnitude of the compressibility and hence is unimportant in determining layer completion.

6.1.3 Isosteric Heat of Adsorption

The heat of adsorption, q_{st}, is a measure of the amount of energy needed to remove a particle from the surface of a film to infinity. For $T = 0$ and zero coverage q_{st} is equal to the binding energy, where at higher coverages where bulk fluid is formed q_{st} is the latent heat. It is defined as [54]

$$q_{\mathrm{st}} \equiv \left(\frac{\partial Q_{\mathrm{R}}}{\partial N_{\mathrm{f}}} \right)_{T,p,A} \tag{6.9}$$

Where dQ_{R} is the amount energy released when N_{f} atoms are adsorbed to the film from the vapour. Assuming that the vapour is an ideal gas this becomes

$$q_{\mathrm{st}} = -\left(\frac{\partial \ln p}{\partial (1/T)} \right)_{N_{\mathrm{f}},A} \tag{6.10}$$

6.2 Initial Characterisation

Initial characterisation of the sample was undertaken independently by the groups of M. H. W. Chan and B. L. Newalker at Penn State. Here efforts have focused on N_2 adsorption and X-ray Diffraction (XRD) data. A summary of the results for the available MCM-41 samples BC1 and BC2 are presented in table 6.1. Sample BC1 was chosen as the experimental substrate as the pore diameter is slightly smaller which should drive up the 2D to 1D transition temperature for a given ^{4}He preplating coverage. Only a brief description of the different techniques used for sample characterisation is given here, for a review of the BET, XRD and KJS methods see the review article by Sonwane [55].

Three different methods have been used to determine the pore radii and the surface area, which begin from two differing standpoints. For the BET method [56]the surface area is the measured quantity and the pore diameter is derived from this using geometric considerations. For the XRD and KJS [55] methods the pore radius is measured and the surface area is derived using the pore volume assuming infinite cylindrical pores.

The BET surface area, S_{BET}, was measured in the usual way by fitting to the N_2 adsorption isotherm. The associated pore radius is then calculated using the Gurvitsch approach where $r_{2\mathrm{V/S}} = 2V/S_{\mathrm{BET}}$ and V is the full pores volume also taken from N_2 isotherm. It is important to note here that the BET isotherm is well known to overestimate the surface area of MCM-41 when using the standard surface density of adsorbed N_2 on a flat substrate and that this effect becomes stronger as the radius of curvature decreases. As the surface area is overestimated this leads to an underestimate in the $r_{2\mathrm{V/S}}$ pore diameter.

The XRD method uses geometric considerations to calculate the inner pore surface using the measured full pore volume and the lattice constant d_{XRD} obtained from XRD measurements. The substrate is modelled as infinitely long cylindrical pores arranged on a hexagonal lattice and the pore surface area, S_{p} is given by

$$S_{\mathrm{p}} = \frac{2V_{\mathrm{p}}}{r_{\mathrm{XRD}}} = \frac{4\pi r_{\mathrm{XRD}}}{\rho_{\mathrm{SiO_2}}\left[\sqrt{3}\left(2r_{\mathrm{XRD}} + W\right)^2 - 2\pi r_{\mathrm{XRD}}^2\right]} \tag{6.11}$$

Here, W, the wall thickness is given by

$$W = \frac{2}{\sqrt{3}} d_{\mathrm{XRD}} - 1.2125 d_{\mathrm{XRD}} \sqrt{\frac{\rho_{\mathrm{SiO_2}} V_{\mathrm{p}}}{1 + \rho_{SiO_2} V_p}} \tag{6.12}$$

Where $\rho_{\mathrm{SiO_2}} V_{\mathrm{p}}/(1 + \rho_{\mathrm{SiO_2}} V_{\mathrm{p}})$ is the porosity and the skeletal wall density is taken to be $\rho_{\mathrm{SiO_2}} = 2.2\,\mathrm{g\,cm^{-3}}$. This can be solved for r_{XRD} to give the pore radius, and from here S_{p} can be calculated.

The final pore radius measurement was made using the KJS [57] approach which uses a modified version of the Kelvin equation, again using the N_2 adsorption isotherm where

$$r_{\mathrm{KJS}} = \frac{2\gamma_\infty \rho}{T \ln\left(P_0/P\right)} + \delta + C \tag{6.13}$$

Here γ_∞ is the surface tension at a flat interface, ρ is the bulk liquid density, δ is the film thickness and C is an empirically adjusted constant. The value of $C = 3\,\text{Å}$ for N_2 is chosen as this is the amount by which this method underpredicts the pore radius compared to the XRD measurements [55]. As such this secondary approach is primarily used in the computation of the Pore Size Distribution, PSD.

The XRD and KJS approaches give a similar pore radius measurement for the BC1 sample of $r = (11.5 \pm 0.5)\,\text{Å}$ which is as expected given that the KJS approach

Table 6.1: Summary of initial N_2 and XRD characterisation of the MCM-41 samples. Sample BC1 was chosen for this experiment as it has a slightly smaller pore diameter. [1]Characterisation by Chan. [2]Characterisation by Newalker. S_{BET} is the usual BET determination of surface area. S_p is the primary (mesopore) surface area. Pore radii, r, determined by $^{(a)}$ $r = 2V/S_{\mathrm{BET}}$, $^{(b)}$ XRD, geometry and porosity, $^{(c)}$ KJS appoach described in the text.

Sample	T (K)	S_{BET}/g ($\mathrm{m^2\,g^{-1}}$)	S_p/g ($\mathrm{m^2\,g^{-1}}$)	V/g ($\mathrm{cm^3\,g^{-1}}$)	$\mathrm{r}^{(a)}$ (Å) BET	$\mathrm{r}^{(b)}$ (Å) XRD	$\mathrm{r}^{(c)}$ (Å) KJS
BC1[1]	64.3	813	638	0.351	8.5	11	
BC1[2]	77.35	992	757	0.454	9	12	11.5
BC2[1]	78	830		0.544	13		
BC2[2]	77.35	959		0.538	11		13.5

is normalised to the XRD results. These are consistent with values for $C8$ and $C10$ [55] where numbers 8 and 10 correspond to the number of carbon atoms in the amphiphile hydrocarbon used in patterning the substrate.

The BET results gives pore radius measurements $\sim 30\%$ smaller and surface area meausrements $\sim 30\%$ larger than for the XRD results in line with expectation. From here we take forward a nominal value of (23 ± 1) Å as the diameter of our pores and $\sim 700\,\mathrm{m^2\,g^{-1}}$ as an estimate of the specific surface area.

6.2.1 Summary of Wada Results

The group of N. Wada at Nagoya University have undertaken an extensive study of pure ^{4}He and isotopic helium mixtures adsorbed on a range of porous substrates. Of these, Folded Sheet Mesopores, FSM-16, is structurally similar to MCM-41. The results presented in this section have been compiled from a number of publications for systems of different pore radii in the range of 18 to 47 Å. For each of these

experiments the powder substrate was mixed with 0.5 μm silver powder and sintered onto silver discs in a silver sample cell to aid cooling below 1 K.

It is noted in the literature [8] that the FSM-16 pore diameters for these samples have been determined using the BJH method [58] based on a modified Kelvin equation although the explicit form of the model is not specified. There exist a number of different models based on this approach which provide quantitively different results, including the KJS model described in section 6.2. In the micropore pore regime the calculated pore diameter can differ by a factor of 2 depending on the version of the BJH method used. For this reason I refrain from relying too strongly on direct comparisons of these FSM-16 results to our MCM-41 results based on the stated pore diameters.

Table 6.2: A summary of the FSM-16 ^{4}He adsorption data. Data for pore diameters followed by (a) and (b) are for measurements made by Wada's group published in [7] and [6] respectively, and (c) is from the theoretical study [16] which is the focus of section 6.2.2. The surface area, S_{BET}, is measured by N_2 adsorption, is used to determine monolayer density, n_1. The position of the observed second minimum in $\kappa_T\, n_2/n_1$ (obs) is shown where $n_2 > 2n_1$ for the largest pore diameter indicating that the minimum is due to complete filling of the pores and not due to layer completion. An estimate of the ratio of n_2/n_1 (est) using purely classical geometric considerations is added for comparison.

σ(Å)		S_{BET}(m^2)	n_1 (Å^{-2})	n_{on}/n_1	n_2/n_1 (obs)	n_2/n_1 (est)
18	(a)	195	0.0741		1.4	1.6
	(b)	157	0.0828	1.15		
22	(a)	141	0.0940		1.7	1.68
	(b)	178	0.101	1.17		
28	(a)	146	0.103	1.4	2.0	1.76
	(b)	182	0.106			
47	(a)	103	0.105		2.9	1.86
	(b)	135	0.106	1.44		
Flat	(c)		0.10	1.53	1.65	

The surface areas quoted have been calculated using the BET isotherm method, which probably results in these being overestimated leading to the corresponding atomic densities being underestimated. It is unclear whether the surface density at monolayer should increase with pore diameter, or if this can be accounted for by the change in S_{BET} with pore radius.

For FMS-16 only two minima in κ_{T} were observed for all pore diameters including the 47 Å sample [7]. The absence of a minimum corresponding to the completion of the second layer suggests that layer-by-layer growth is not well defined in the pores at the experimental temperatures. The statistical thickness of the film derived from the Frenkel-Halsey-Hill (FHH) isotherm model grows monotonically, proportional to the adsorbed amount up to the second mimimum. At this point the constant of proportionality increases consistently with the difference in surface areas calculated for the inner pore walls and the outer grain surface. For the larger pores monolayer density approaches $0.108\,\text{Å}^{-2}$ the value for ^{3}He [59] and $0.120\,\text{Å}^{-2}$ for ^{4}He [52, 53] on grafoil.

We also observe for the largest pores $n_2/n_1 = 2.9$. The second layer density must be lower than the first indicating the coverage is more than high enough to form a complete second layer in the pores. It is therefore reasonable to assume that for all pore sizes the second minimum in κ_{T} is due to complete filling of the pores and not second layer completion. Further experimental confirmation is required to show that two well defined layers can form in the pores at low temperatures.

The increase in film thickness scaled in terms of n_1 is similar for all pore diameters showing that capillary forces have little effect on the solid first layer. Figure 6.1 shows a comparison of the adsorbed ^{4}He film thickness for 18 Å and 47 Å pores. The

film thickness is greater than for our MCM-41 data at monolayer indicating that the binding energy is lower. This is also seen in the measured heat of adsorption where q_{st} is higher for our sample at a given coverage.

We can crudely approximate the ratio of atoms in the first and second layers, $n_2/n_1(\mathrm{est})$, by assuming that the ^{4}He atoms are hard spheres and considering the numbers of atoms that could be placed on two concentric rings of diameter $(\sigma - d)$ and $(\sigma - 3d)$. For areal density $n_1 = 0.108\,\text{Å}^{-2}$ we obtain a sphere diameter $d \sim 3\,\text{Å}$. The ratios obtained are shown in table 6.2.

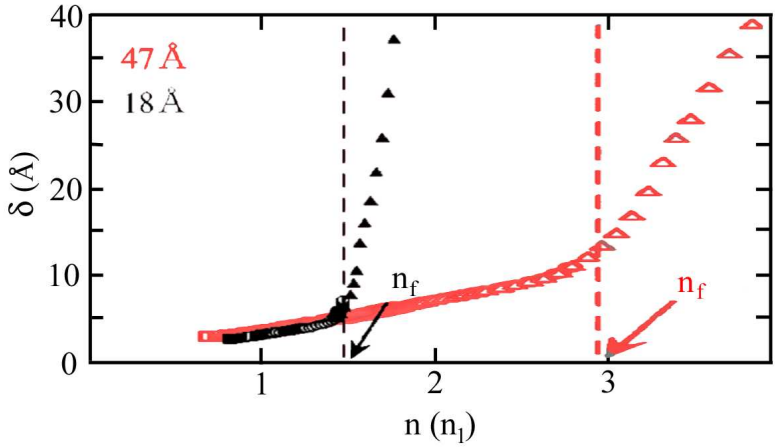

Figure 6.1: The thickness of a ^{4}He film adsorbed on two FSM-16 substrates scaled to monolayer completion density, n_1. The black symbols are for 18 Å pores and red symbols for 47 Å pores. The growth of the film appears similar up to full pores, n_{f}.

Torsional oscillator experiments [6, 7, 11] have confirmed that a substep observed in the isothermal compressibility coincides with a mass decoupling attributed to the onset of superfluidity within mesopores of various diameters. Such a substep in κ_{T} was observed for samples where the pore diameter was greater than 28 Å which can be understood in terms of a Kosterlitz-Thouless superfluid transition. The torsional oscillator study also showed a finite mass decoupling for substrates with

pore diameters as small as 18 Å which cannot be understood in terms of Kosterlitz-Thouless assuming that the pore diameters are not underestimated to a large extent. The superfluid transition temperature for the 22 Å pores at coverages below n_2 were lower than 500 mK, the minimum temperature of the vapour pressure study.

A heat capacity study shows a Shottky type peak occurring for some systems of ^{3}He adsorbed in ^{4}He preplated pores [4, 9] indicating a dimensional cross-over to a 1D fluid state at temperatures significantly below the phenomenon. The observation of the peak was found to be dependent on the preplating coverage. Where we expect the position of the peak to be driven up to higher temperatures as the pore size decreases, little change was found. Also at higher coverages the peak was not observed. This has been attributed to Andreev surface states in the film [9].

6.2.2 Monte Carlo Simulations

A study of ^{4}He adsorbed on a flat glass substrate was undertaken by M. Boninsegni using Monte Carlo simulations [60]. This yielded a phase diagram up to promotion from the second layer as a function of surface density, shown in figure 6.2.

Here the substrate is modelled as a semi-infinite structureless flat glass with a 6-12 Leonard-Jones potential using equation 2.5, where D is taken to be 100 K and $a = 2.05$ Å. This is equivalent to $\Gamma \approx 1292\,\mathrm{K\,\AA^3}$, which is slightly higher than the value of $\Gamma = 1100\,\mathrm{K\,\AA^3}$ used for the preceding calculations, and those of Wada and Cole. It becomes increasingly difficult to perform calculations at lower temperatures using this technique, and therefore the majority of calculations were performed at 1 K.

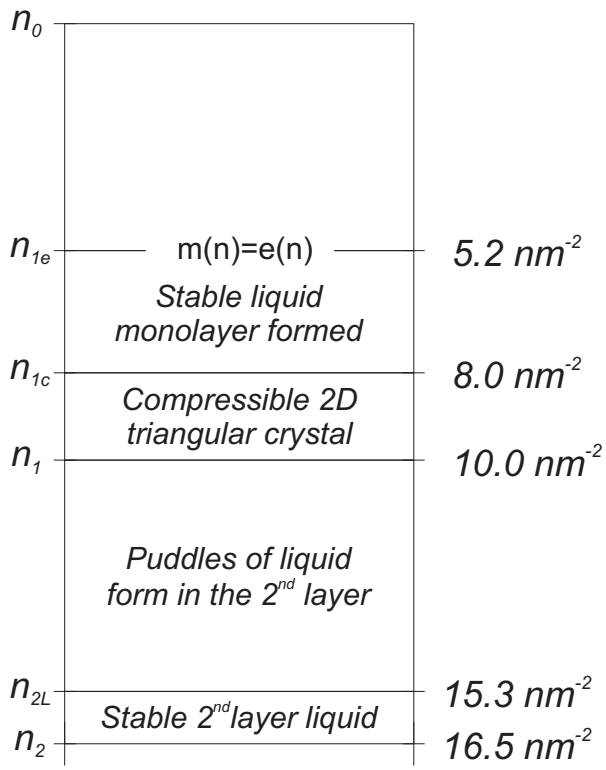

Figure 6.2: Theoretical Phase Diagram of low coverage ^{4}He adsorption on a glass substrate

In the first layer a stable fluid was found at 1 K for densities above the monolayer equilibrium coverage where the energy per particle was equal to the chemical potential, $e(n) = \mu(n)$, where the density was found to be $n_{1e} = 0.052\,\text{Å}^{-2}$. It should be noted that in a real system, where the surface is corrugated and disordered a "glassy" insulating monolayer will be stabilised. In the model the first layer solidified forming a triangular lattice at $n_{1c} = 0.08\,\text{Å}^{-2}$. Promotion from the monolayer was found to begin at $n_1 = 0.1\,\text{Å}^{-2}$ which is quantitatively very close to that observed by Wada in table 6.2.

^{4}He in the second layer was found to puddle at low densities forming a stable fluid at $n_{2l} = 0.153\,\text{Å}^{-2}$ with a superfluid fraction of approximately 1/3. The onset of superfluiditity was also reported by Wada for FSM-16 materials. Promotion to the

Table 6.3: Comparison of the statistical thicknesses of an adsorbed ^{4}He film at monolayer. Data for this study is for the MCM-41 sample with 23 Å pores. For the FSM-16 data this is independent of pore diameter and for the Boninsegni study this is for a flat structureless glass.

Study	δ(Å)
This Study MCM-41	3.2
Wada FSM-16	4.2
Boninsegni	2.36

third layer began at $n_2 = 0.163\,\text{Å}^{-2}$.

Table 6.3 shows a comparison of monolayer film thicknesses for our MCM-41 sample, the FSM-16 sample of Wada [7] and the Monte Carlo simulations of Boninsegni. The film thicknesses for this work and that of Wada are calculated from the measured vapour pressure using the FHH isotherm (equation 6.14), assuming $\Gamma = 1100\,\text{K}\,\text{Å}^3$ whilst the equivalent for the Boninsegni study is $\Gamma = 1292\,\text{K}\,\text{Å}^3$.

Boninsegni's study also includes information about a single ^{3}He impurity in a ^{4}He film. This shows that at 1 K the ^{3}He atom resides in the top layer of the film at all coverages but does not float on top of the film. However, this is calcuated for a flat substrate and it is thought that at low enough temperatures quantum confinement in the pore will force the average position of the ^{3}He to be away from the top layer.

6.3 ^{3}He Isotherm

Our initial pressure and NMR measurements were made using ^{3}He as the adsorbate species. This was for the dual purpose of ensuring our substrate was in good condition after preparation and loading the cell and that our NMR spectrometer was functioning correctly with adequate performance.

For this run the main gas handling system was in the configuration described in section 4.3 where the dosing volume incorporated three computer controlled solenoid valves. The intention was to use this isotherm to gain information about the isotherm process which would allow full automation of the process on subsequent runs. The dosing volume for this run was 2.92 cm^3. The cell pressures were measured using a Paroscientific pressure transducer at room temperature, which uses a quartz crystal resonator whose period of oscillation varies with pressure induced stress. There is a second temperature dependent quartz crystal resonator used to compensate for changes in ambient temperature. The two periods are read out by a single Keithley 2000 DMM with scanner card controlled by a computer running LabVIEW, where an algorithm is used to convert the frequency to pressure. As the Paroscientific gauge is connected to the cold volume by an impedance we must apply thermo-molecular pressure corrections to ascertain the correct pressure at the lower temperature. This becomes important for our system below 10 mbar. The limit of resolution for this set-up is $\sim 50\,\mu$bar at low pressures with a pressure range of 0 to 1 bar.

The ^{3}He isotherm was carried out discontinuously whilst loading the cell for the associated NMR experiments. The longest breaks lasted up to a few months whilst a detailed calibration of the spectrometer took place and an in depth study the NMR parameter space was undertaken.

For coverages up to $n = 0.88\ n_1$, the first coverage where NMR experiments were performed, the isotherm was completed at 4.23 K with ^{4}He exchange gas in the IVC to suppress any temperature instabilities. Consequently it was not possible to anneal the cell at elevated pressures between coverages so the cell was allowed to come into equilibrium for 30 minutes between shots. After this time fluctuations and

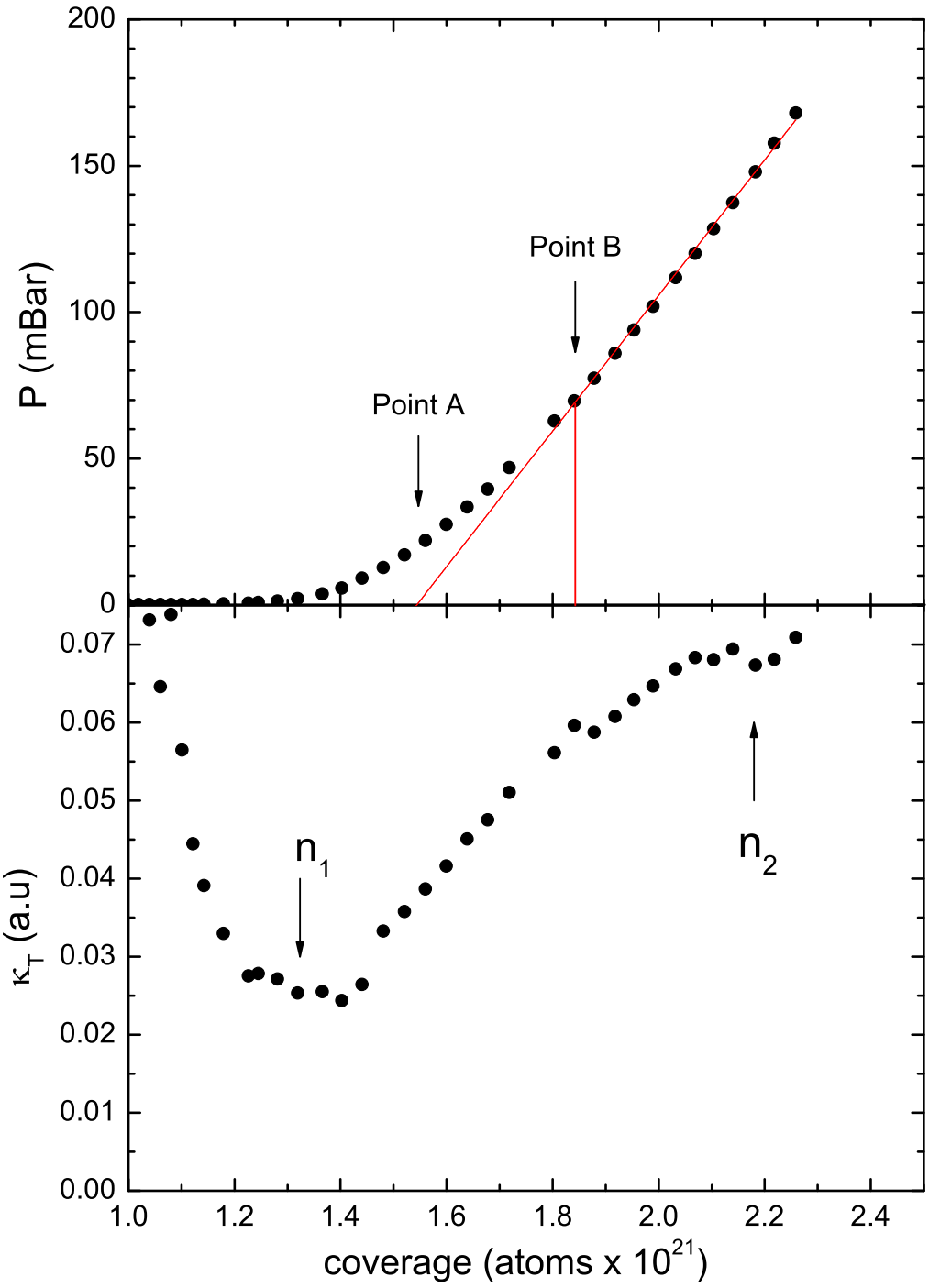

Figure 6.3: (a) ^{3}He vapour pressure isotherm completed at 4.2 K. (b) Isothermal compressibility calculated using the data in (a).

instabilities in the pressure sensor dominated any variation in vapour pressure. ^{3}He was added to the cell until a finite vapour pressure was observed. Due to the high binding energy of the substrate with the first layer atoms a finite vapour pressure is observed around monolayer promotion. At this coverage there was also a sufficient number of spins to observe a relatively large NMR signal and make a rough estimate of the adsorption surface area.

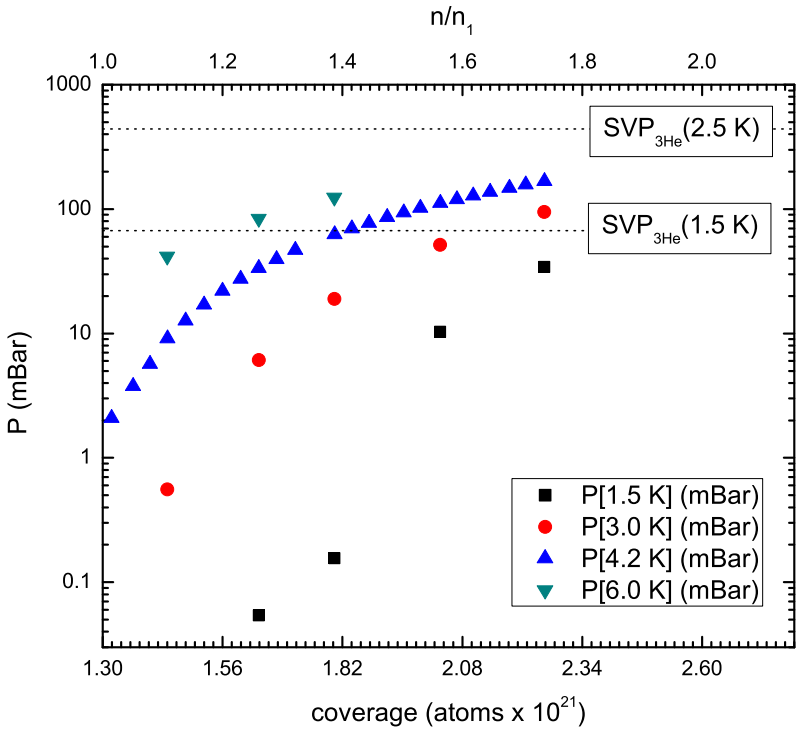

Figure 6.4: ^{3}He vapour pressure isotherm as a function of coverage

At this coverage the NMR spectrometer was characterised and a number of experiments were performed taking a few months to complete. During this period the exchange gas was removed from the IVC and the cell was operated in the temperature range 1.5 K to 8 K, measured using the calibrated germanium thermometer located on the cell plate. The isotherm was continued in smaller sections, each consisting of 3 to 6 shots, whilst stepping through NMR coverages. This was done with

the 1 Kpot running flat out and the cell stabilised at 4.23 K using a home built PID temperature controller described in section 4.1.1.

The resultant isotherm is shown in figure 6.3(a). It was convenient to use the number of atoms admitted to the cell as our unit of coverage. This was calculated assuming the gas to be ideal and it was a natural unit choice as we have the pressure and temperature of each shot in the dosing volume readily available. Point A is extrapolated to be at 1.54×10^{21} atoms and point B at 1.84×10^{21} atoms. The point B definition of layer completion is not in agreement with the first minimum in the two-dimensional compressibility, n_1, shown in figure 6.3(b). Here monolayer is observed at $(1.3 \pm 0.1) \times 10^{21}$. From this plot, full pores at n_2 is thought to occur at the small compressibility minimum at 2.2×10^{21}, giving a ratio $n_2/n_1 = 1.69$ which is in good agreement with the results of Wada [7] who gives $n_2/n_1 = 1.7$ for ^{4}He adsorbed in similar 22 Å pore pores, shown in table 6.2. For subsequent results for this run the coverage will be expressed in terms of the completed monolayer coverage n_{3He}/n_1 where n_1 is 1.3×10^{21}.

The vapour pressures as a function of temperature for coverages above monolayer are shown in figure 6.4. The vapour pressure decreases significantly with temperature suggesting that the film is cooling. The saturated vapour pressures for bulk ^{3}He at 1.5 K and at 2.5 K are marked on the plot for reference. The ^{4}He isotherm, measured later, was continued beyond full pores where the film thickness increased rapidly with coverage and the pressure approached the saturated vapour for the temperatures measured using the germanium thermometer. The ^{3}He isotherm was finished prior to this occurring and so it is not possible to use this to determine the temperature. At low pressures where $p \ll 1$ mbar the thermomolecular pressure corrections become important and the error in the pressure is large.

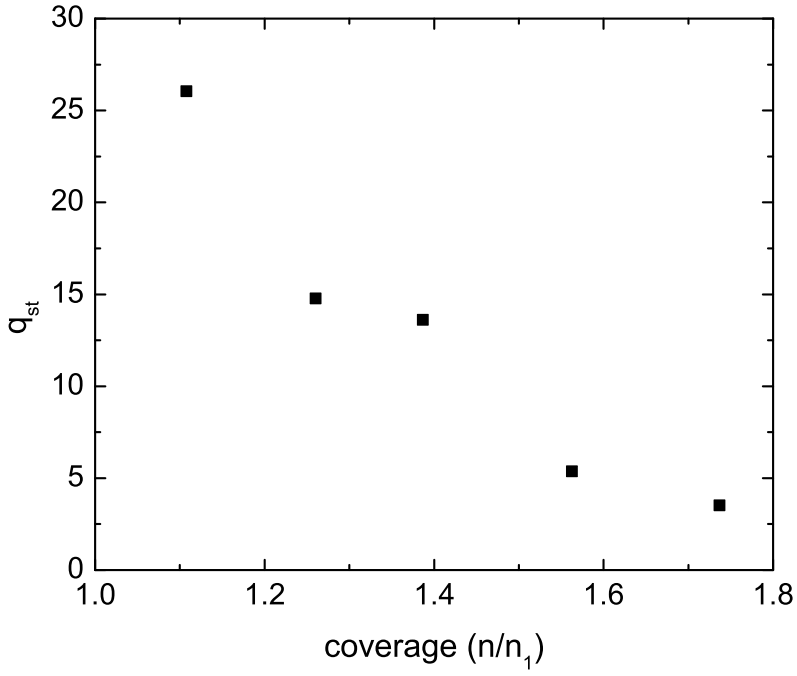

Figure 6.5: Isosteric heat of adsorption for ^{3}He as a function of coverage.

The data from figure 6.4 was used to calculate the isosteric heat of adsorption shown in figure 6.5. The steep decrease in q_{st} with increasing coverage is characteristic of a strongly heterogeneous surface.

The statistical thickness of an adsorbed film can be estimated using the FHH model. This continuum model does not take into account the layer by layer growth of the film or the capillary force of the pore, which limits its usefulness in the low coverage regime. This model predicts the film thickness $d(\text{Å})$ as

$$d = \left[\frac{T}{\Gamma}\ln\left(\frac{p_0}{p}\right)\right]^{-1/3} \tag{6.14}$$

Where p_0 is the saturated vapour pressure and $\Gamma = 1100\,\mathrm{K\,Å}^3$.

The film thickness has been calculated using the vapour pressure measurements at 3 K as this gives a reasonable pressure across the coverage range. The first layer

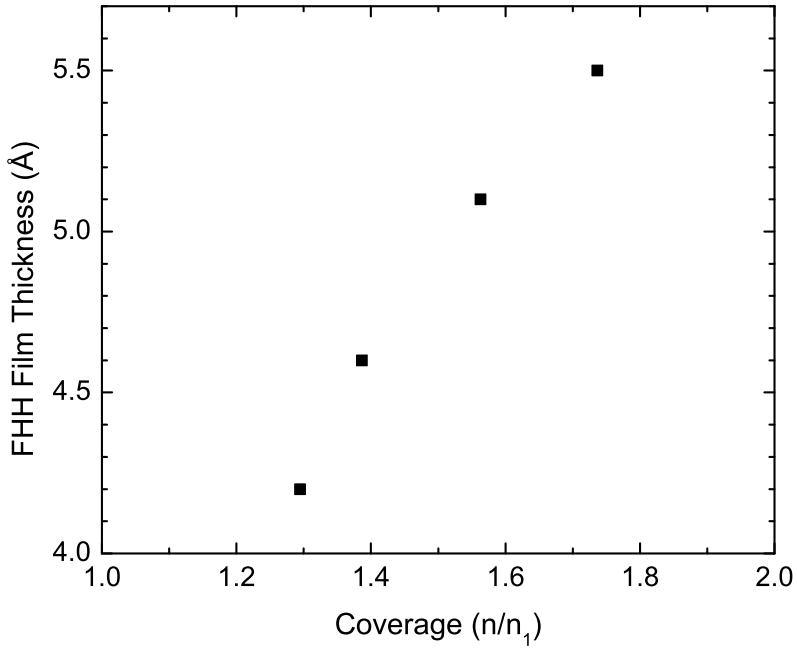

Figure 6.6: ^{3}He film thickness calculated using the assumptions of the FHH model. This was calculated using vapour pressure measurements at 3 K

is expected to be solid and as such will be shallower than indicated on the plot. This model has been improved upon for ^{3}He adsorbed on a graphite substrate [52] by assuming solid non-interacting first layer of an assumed depth. However the film thickness is presented here to illustrate that the film is growing homogeneously up to our highest coverage. As the pore adsorption area is far greater than the outer surface of the powder grains we would expect the rate of increase of the film thickness to be much higher when the pores saturate. This was observed for the ^{4}He isotherm and suggests that this isotherm was stopped before full pores.

6.3.1 Limitations of the Isotherm

There were a number of issues identified during this isotherm which prompted the changes to the GHS made in section 4.5 and the addition of the low temperature

pressure gauge described in section 4.3. Whilst constantly powered the equilibrium operating temperature of the solenoid valves was approximately 80 °C, as measured with a thermocouple. This large deviation from ambient temperature made measuring the amount of gas admitted to the cell difficult and the temperature compensation is not accurate over such a large temperature range. This could have lead to a significant overestimate of the total amount of ^{3}He gas admitted to the cell, which could explain why we later measured monolayer completion at similar densities for ^{3}He and ^{4}He. The Solenoid valves use Viton seals, therefore replacing the solenoid valves with HiP valves also alleviated the concern about outgassing water vapour into our system, especially at the raised temperatures.

Also the compressibility minimum corresponding to monolayer completion is not well defined. At this point the vapour pressure at 4.2 K is less than 10 mbar meaning that thermomolecular pressure corrections are important and the gauge is not stable or sensitive enough to provide an adequate pressure reading. The addition of the low temperature pressure gauge mounted at the same plate as the cell negated any thermomolecular pressure differences. Also the sensitivity of the gauge in the low pressure regime was 1.2 µbar increasing the sensitivity where $p \ll p_0$. The low temperature pressure gauge has an operating range of 0-10 mbar, and applying a significant over pressure stresses the membrane at the point it is clamped and can cause permanent damage. This limits the accessible temperature range, and to cover the whole coverage region necessitates combining a number of different isotherms at different temperatures.

There is some uncertainty to the surface area of the MCM-41 sample in our cell. We have two measurements of surface area per gram that were provided with our sample powder, each from a different group. Both were obtained by fitting to a

N_2 BET-Isotherm and gave values of $992\,m^2\,g^{-1}$ and $813\,m^2\,g^{-1}$. We believe that our cell contains 246 mg of our sample powder. The Isothermal compressibility was calculated assuming $813\,m^2\,g^{-1}$ giving a total surface area of $200\,m^2$. We calculated the amount of powder that we have in our cell by comparing the combined weight of the powder and the sample container before filling the cell to the weight of the remaining powder and sample container after filling the cell. Our sample cell is fairly heavy and due to practical considerations it was not possible to make an accurate measurement of the weight of the cell before and after filling. As such 246 mg is an upper bound to the amount of powder in the cell as some powder was lost to spillage and also some became stuck to the spatula and rod used to pack the powder into the cell.

The minima in the two-dimensional compressibility are associated with layer promotion. We see the first compressibility minimum, corresponding to monolayer completion, at approximately 1.3×10^{21} atoms. If we assume a surface area of $200\,m^2$ then we have an surface density of $6.5\,nm^{-2}$. We would have expected a higher surface density, closer to the ^{4}He monolayer density of $\sim 10\,nm^{-2}$ reported by Wada for a similar pore diameter, shown in table 6.2, slightly lower than the ^{3}He on grafoil value of $12\,nm^{-2}$ [52, 53].

Aside from the uncertainty in the mass of the powder in the cell the discrepancy in the measurements could also be due to inaccuracy in the measured surface area per gram, surface contamination and possibly some of the pores may be closed due to contamination or instability of the pores on thermal cycling as observed for the ^{4}He isotherms.

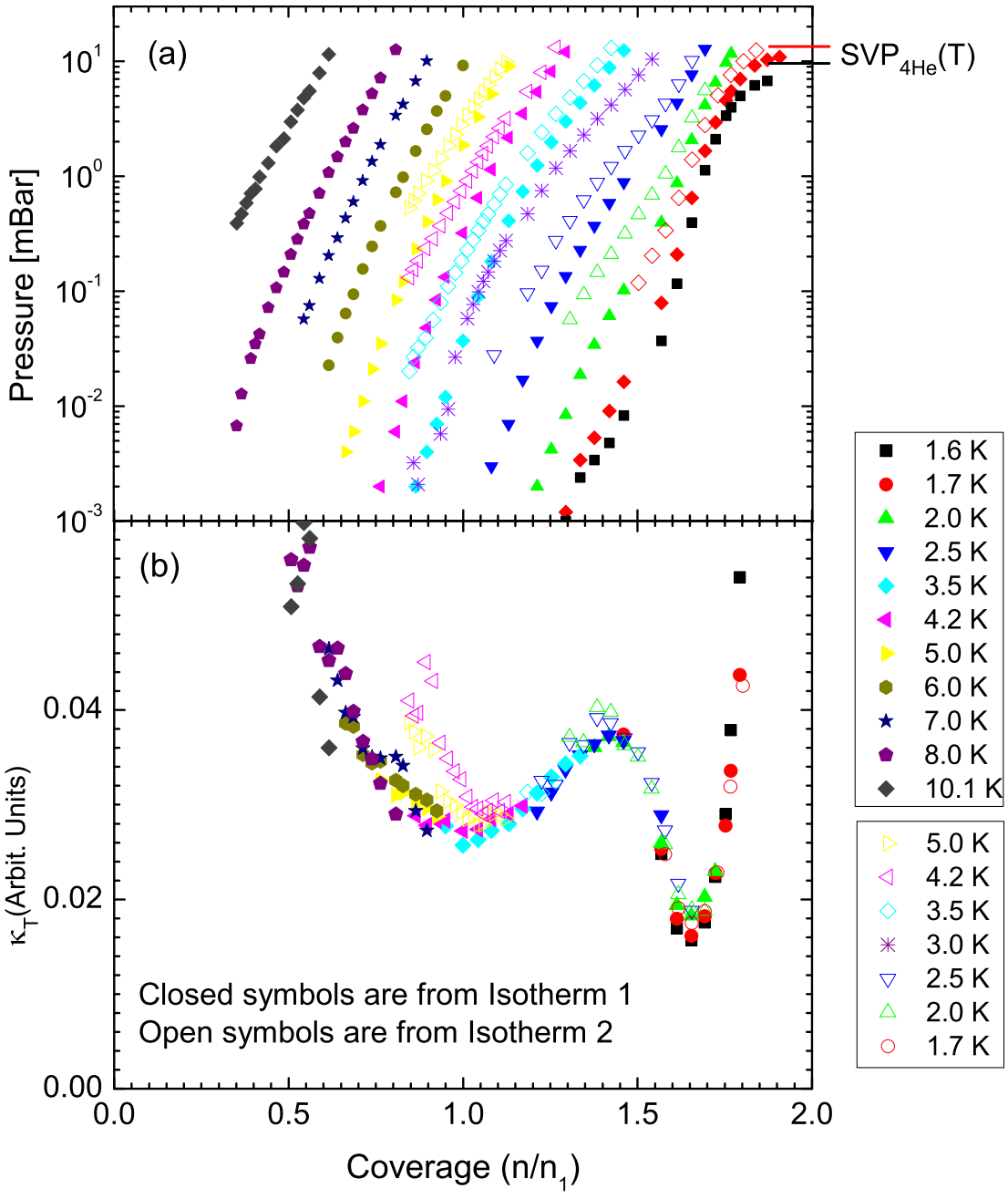

Figure 6.7: A comparison of (a) Pressure and (b) κ_T vs coverage for the first (Closed symbols) and second (Open symbols) ^{4}He isotherm runs.

6.4 ^{4}He Isotherm

We performed two subsequent vapour pressure isotherms using ^{4}He as an adsorbate. For the first measurement the isotherm was completed to full pores continuously over a period of one month. The second measurement was taken whilst performing NMR measurements on the ^{4}He preplated NMR run, taken discontinuously over a one year period. On this second run 0.02 monolayer consisted of ^{3}He whilst the remainder of the adsorbate was ^{4}He. The results of these measurements are compared with the similar measurements of Wada for a FSM-16 substrate with similar mechanical structure [4, 7] and the theoretical study of Boninsegni [16] for a flat glass substrate.

These measurements were both made using the same experimental setup, where the main GHS had been modified as shown in figure 4.5 and measurements of cell pressure were made using the low temperature pressure gauge described in section 4.3. The readout method for the gauge was changed between runs to compare the relative performance. For the first run the gauge capacitance was measured using the inductive voltage divider circuit and for the second run this was replaced by an AH 2550 capacitance bridge. The two bridge circuits are described in section 4.3.3. The main difference between these two methods is that the IVD circuit measures the gauge capacitance against a cold reference capacitor mounted on the same plate with a similar wiring configuration. This was done to compensate for any variation in stray capacitances that may occur as a function of bath level. The AH bridge incorporates an integrated temperature stablised reference capacitor. The gauge capacitance was found to be approximately constant as a function of bath level with fluctuations equivalent to a few μbar.

Figure 6.7 shows the vapour pressure isotherms and the corresponding isothermal

compressibilities for the first and second ^{4}He isotherms. These were found to be in excellent agreement when the surface area for the second isotherm is scaled to be 0.945 that of the first, and n_2/n_1 was found to be the same in both cases. This suggests that some of the pore may have degraded or become blocked rather than being due to impurities on the adsorption surface.

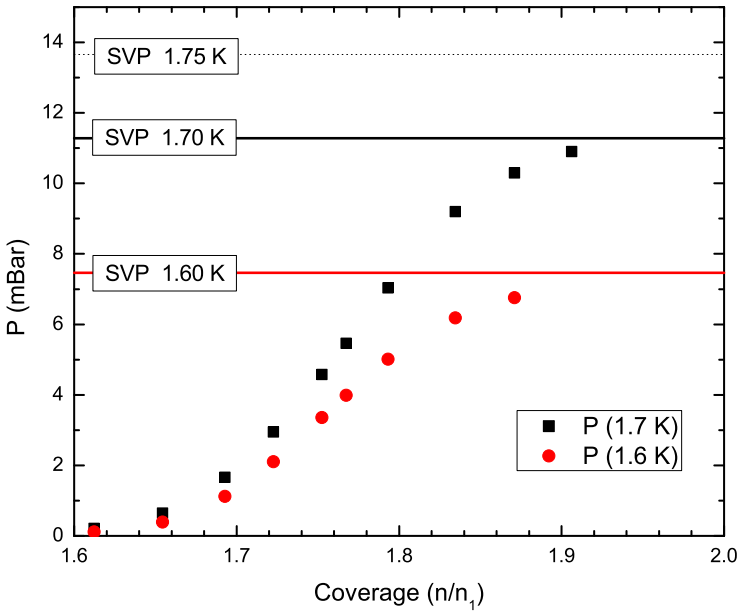

Figure 6.8: Cell pressure and $SVP_{^4\mathrm{He}}$ in the coverage region around the second minimum in χ_T. This suggests that the cell is cooling to the temperatures measured by the germanium thermomometer.

In figure 6.7(a) at coverages, above the second compressibility minimum, the pressures are tending to the saturated vapour pressure (SVP) values. The ITS90 SVP's for 1.6 K and 1.7 K [21] are marked on the plot as horizontal lines in the same colour as the corresponding data. This is shown more clearly in figure 6.8.

In figure 6.9 we see that at these coverages the film thickness is diverging and bulk liquid is forming. This suggests that the Ge temperature was the same as the cell temperature down to the lowest achievable temperatures.

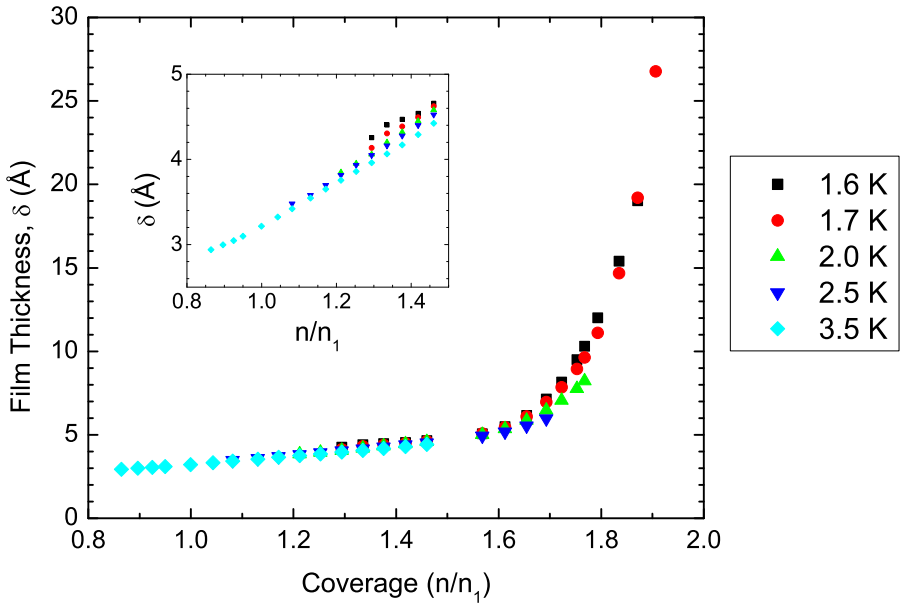

Figure 6.9: ^{4}He film thickness assuming FHH potential. This can be thought of as the average film thickness. The film grows linearly with coverage up to n_2

The rate that the film thickness is increasing with coverage increases by a factor of $\sim$ 100 above the second minimum in κ_T. The surface of the powder grains after complete filling of the pores can be estimated assuming spherical grains with 3000 Å diameter. A simple order of magnitude calculation for the ratio of pore surface area to the powder grain surface area assuming that the pore diameter is 23 Å and the pore length is equal to the grain size also gives a factor of $\sim$ 100. This is in agreement with the measurements of Wada [7] and confirms that in our case n_2 corresponds to full pores.

Figure 6.10 we see that the Point B definition of layer completion appears to coincide with second layer completion from the compressibility data. The form of the isotherm is believed to be *type IV*, as defined by the IUPAC [14], except here the second layer is strongly bound to the substrate so the initial pressure step associated with monolayer completion is not observed. We would not expect to observe hys-

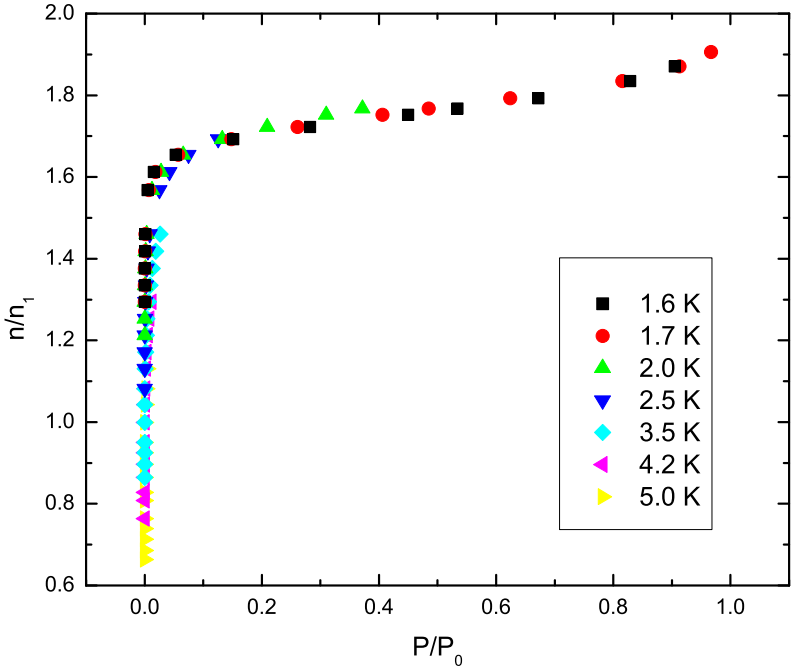

Figure 6.10: Coverage against reduced pressure for the first ^{4}He run.

teresis caused by capillary condensation for helium with this pore diameter, however we did not attempt to perform a desorption isotherm. Some hysteresis was observed by Bharat in the initial sample characterisation, consistent with *H1* [14], however this was not observed in the measurements of Chan. This hysteresis was attributed to the automated nature of the Bharat isotherms, where perhaps insufficient time was allowed for the cell to anneal or equilibrate.

The isosteric heat of adsorption is shown in figure 6.11. This is characteristic of a strongly heterogeneous substrate and is similar to those reported by Wada [4, 7]. At the highest coverages q_{st} is consistent with the latent heat of bulk ^{4}He which is $\sim 10\,\mathrm{K}$.

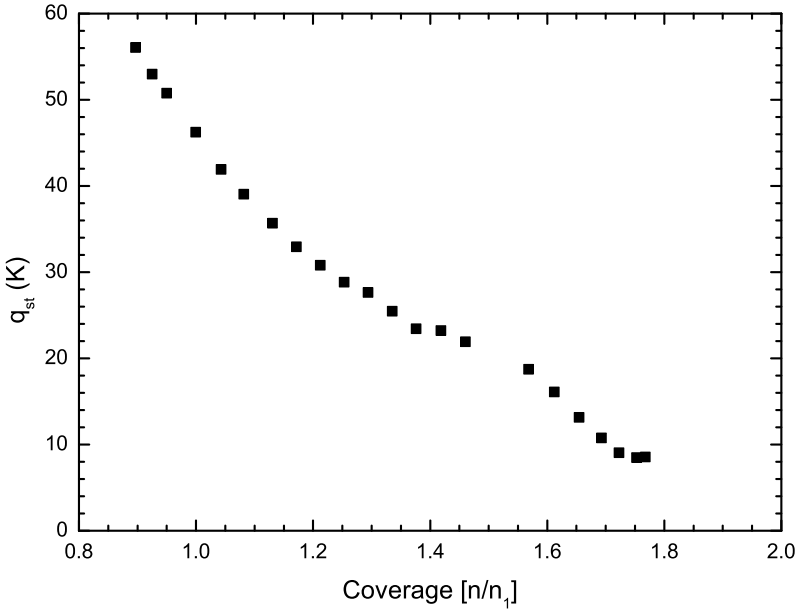

Figure 6.11: The isosteric heat of adsorption, q_{st}, as a function of ^{4}He coverage.

6.4.1 Conclusions

The sensitivity of the installed low temperature pressure gauge enabled the computation of the isothermal compressibility, κ_{T} from vapour pressure isotherms. The measurements described in this chapter show that κ_{T} is a useful tool for the characterisation of MCM-41 and allowed the measurements from this experiment to be compared with those of Wada for the similar FSM-16 substrate.

The isothermal compressibility can be measured over a range of temperatures which allows the vapour pressure to be maintained at a low value whilst characterising the entire experimental coverage range. This minimises the fraction of atoms in the vapour phase. At the highest coverages the vapour pressure approached the saturated vapour pressure corresponding to the temperature measured by the germanium thermometer on the cell plate. This suggests that at least in the case of finite vapour pressure the cell was cooling as expected.

For FSM-16 κ_T only exhibits two minima, n_1 and n_2, corresponding to monolayer completion and full pores respectively, including cases where multilayer film growth should geometrically be possible. We expect this to be the same for MCM-41. The measured ratio of $n_2/n_1 = 1.65$ for our 23 Å agrees well with the value of 1.7 reported by Wada for 22 Å pores in FSM-16. This offers an additional confirmation of the measured pore diameter of our substrate and also confirms the suitability of the surface preparation technique where the sample is transferred to the sample cell after baking in a quartz glass tube.

In chapter 7 monolayer completion is associated with a minimum in T_2 measured as a function of coverage, as is observed for ^{3}He adsorbed on grafoil. This occurs at the same coverage as n_1 showing that our independent measurements of layer completion are in agreement. The rate of increase in film thickness with coverage is ~ 80 times higher above n_2 than it is at lower coverages. This is similar to the calculated ratio of the surface area inside the pores to the surface area of the outside of the powder grains.

Chapter 7

Nuclear Magnetic Resonance Measurements

This chapter describes the two NMR experiments performed. In the first experiment isotopically pure ^{3}He was used as an adsorbate. This provided a large signal with which to calibrate the spectrometer and characterise the sample substrate using a simple system. This is compared with the results of other 2D ^{3}He adsorption experiments.

The second experiment examines the feasibility of creating a quasi-1D system under the stringent conditions described in section 2.3. This necessitated the use of very low ^{3}He coverages, as small as 1% of monolayer, making signal sensitivity an issue. The viability of a future low temperature experiment depends in part on the expected relaxation times. If T_1 is too long it become difficult to average decays and if T_2^* is too short the signal becomes broard in the frequency domain resulting in a small signal-to-noise ratio.

7.1 Calibrating the Spectrometer

The spectrometer was calibrated with a bare ^{3}He coverage of $n_{3He}/n_1 = 0.88$ at frequencies around 200 kHz using an FID pulse sequence described in section 3.3.2.

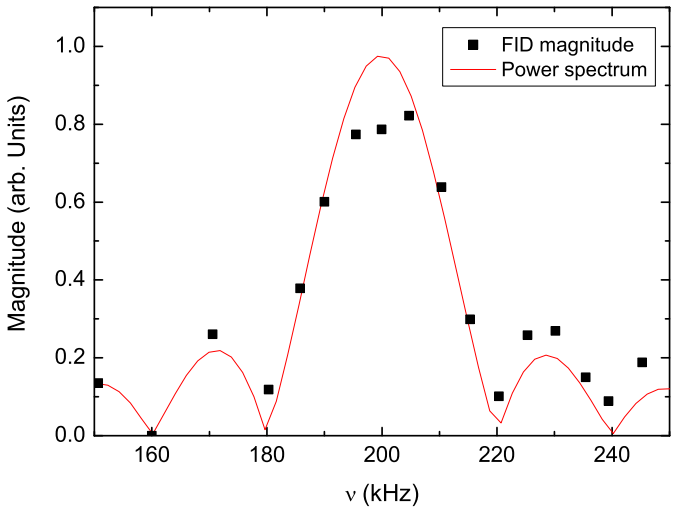

Figure 7.1: NMR power spectrum obtained by exciting the system with a 50 µs 90° pulse at 200 kHz whilst varying the static B_0 NMR field compared with the FFT of the pulse

The field-current ratio of the main NMR magnet described in section 4.4.1 was measured with a hall probe as 4.05 mT A^{-1}in a transport Dewar. The gyromagnetic ratio, γ, of ^{3}He is given by $\gamma/2\pi = 32.44\,\mathrm{MHz\,T^{-1}}$ therfore to excite ^{3}He at a resonant frequency $\nu_\mathrm{L} = 200$ kHz requires a field $B_0 = 6.16$ mT. After observing the first NMR signal the B_0 field was tuned to obtain the greatest FID response and the observed field-current ratio was found to be $B_0 = 3.805\,\mathrm{mT\,A^{-1}}$. This was confirmed by obtaining the NMR power spectrum, exciting the system with a 50 µs 90° pulse at 200 kHz whilst varying B_0. This is shown in figure 7.1 where the measured power

spectrum is compared with the FFT of the excitation pulse.

In section 4.4.3 the field-current ratio of the transmitter coil in free space was calculated to be $(B_1/I)^{\text{th}} = 1.11\,\text{mT}$. The tipping angle is given by equation 3.16, and for a 90° pulse becomes $B_1' = \pi/2\gamma\tau$. Short T_2^* relaxation times were expected so a 50 µs pulse length was chosen equating to 10 cycles at 200 kHz, requiring $B_1' = 154\,\mu\text{T}$. For the calculated field current ratio this requires a peak-to-peak pulse of 5.55 A. The transmitter was calibrated by obtaining FID's with a constant B_0 field and pulsing on resonance at 200 kHz with different B_1 pulse heights. The experimentally obtained value of B_1 was found to be 392 µT/A which is approimately a factor of 3 lower than the calculated value. This attenuation of the field is due to the proximity of the superconducting shield.

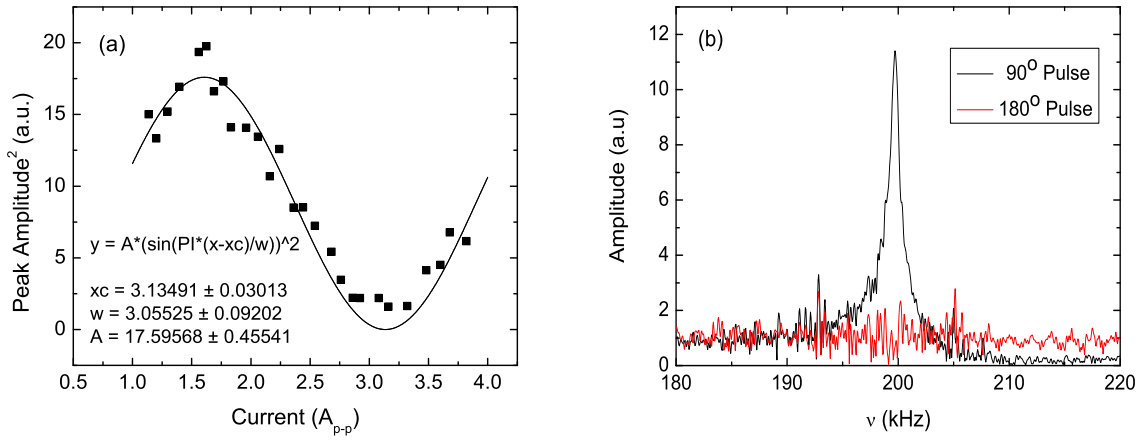

Figure 7.2: (a) Determination of a 50 µs 90° pulse at 200 kHz obtained by applying transmitter pulses of varying magnitudes. (b) FID's following 90° and 180° transmitter pulses.

7.2 Digital Signal Processing Techniques

In this section I will outline the signal processing necessary to obtain NMR signals and indicate where each technique was implemented. A number of different approaches were needed to deal with the coherent and incoherent noise sources, some taking place during data acquisition and others applied during analysis. The signal processing prior to data capture is indicated in the NMR system block diagram figure 4.11.

7.2.1 High Pass Filter & Sample-and-Hold

In our system the NMR signals are small and relaxation times relatively short, of order ms. It is important that we can begin data acquisition sufficiently close to the pulse that the reduction in signal height is small. In practice this means that we need our dead time to be at least less than T_2^*. Broadband SQUID detection is ideal for this type of system as spectrometer recovery times can be made very short because they are not limited by the ringing in a resonant circuit. For our spectrometer the recovery time is determined by eddy current transients in the magnet former following transmitter pulses as mentioned in section 4.4.3. Transient artifacts observed for this experiment were found to be approximately 4 orders of magnitude larger than the NMR signal. To observe the transient without exceeding the 15 V range of the FLL electronics would require the use of a significantly reduced FLL feedback resistance, R_f, which would decrease the sensitivity adding an unacceptable amount of digitisation noise.

A high-pass filter and sample-and-hold device are implemented to limit the effect of

the transient. We use the simplest high-pass filter available to us, using an inline capacitor and a resistance to ground with a cut-off frequency $f_c = 4.8$kHz. The filter produces a response proportional to the differential of the transient, however as $f_c \ll \nu_0$ this does not effect the signal in the region of the resonance. Although far smaller than the original transient, the magnitude of the response from the filter becomes the limit on the resolution of the scope. To reduce this response we use a sample-and-hold device to cut off the initial part of the transient. The sample-and-hold device is similar to that described in Horowitz and Hill [61] and is used to subtract a DC offset from the signal. The value of the DC offset is equal to the signal voltage when the sample-and-hold device is initialised. Using this combination the dead times have been reduced to as little as 25 μs.

7.2.2 Background subtraction

In general it has been necessary to perform two types of background subtraction to remove large noise sources at low frequencies and noise around the Larmor frequency. The initial background subtraction is to remove magneto-acoustic resonances at the Larmor frequency which occur as responses to the NMR pulses. These are described in great detail in the thesis of Körber [41]. Fortunately these are coherent and scale as B_0^2, which means that they are not reduced by averaging but can be subtracted using the following method. First the on-resonance time-domain NMR data set is taken with some number of averages. An off-resonance background trace is taken with the field de-tuned to a resonant frequency corresponding to the first minimum in the transmitter pulse power spectrum. The background trace is normalised as $(B/B_0)^2$ before subtracting from the resonance trace in the time domain. Figure 7.3

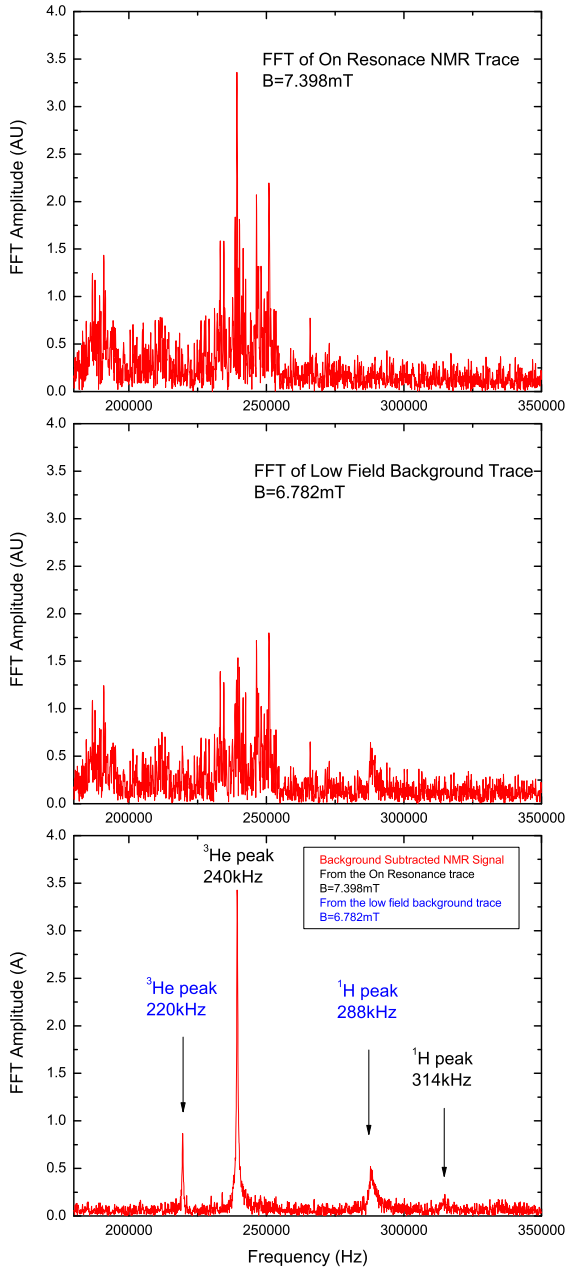

Figure 7.3: (a) The Fourier transform of an NMR trace without background subtraction. Note the NMR signal is obscured by the acoustic resonances. $\nu_{\mathrm{L}} = 240$ kHz, 1000 averages. (b) A background trace where B_0 is detuned to the first minimum in the transmitter pulse power spectrum. All other setting are unchanged. (c) The final background subtracted NMR signal. This example was chosen as there was still some spectral power in the background trace, background signal can be observed. A second proton NMR signal from the stycast sample cell is also observed.

shows the on-resonance trace, off-resonance trace and background subtracted data. The resulting spectrum shows that this technique works remarkably well, however eventually our resolution is limited by our ability to perform this background subtraction. The resonances are weakly time dependent, so we tried to limit time between capturing the on-resonance and background data. 12 hours was found to be acceptable for most cases and allowed for sets of T_1 and T_2-echo measurements to be made without re-tuning the magnet between individual data points. The resonances are also permanently altered by environmental changes such as transferring liquid helium, knocking the cryostat or changing the grounding of the system.

It is necessary to perform polynomial background subtraction on the data to remove the remnants of the transient This is done by dividing the data set into a number of subsets and fitting a low order polynomial to each set in the time domain. The number of sets and polynomial order are chosen to ensure that the routine does not extend up to frequencies approaching the Larmor frequency.

7.2.3 T_2^* Filter

In the case where the signal-to-noise ratio (SNR) is small it is possible to enhance the SNR by multiplying the captured FID by a decaying exponential function with time constant T_{fil} in the time domain. This process of convolution-apodisation enhances spectral features with the chosen linewidth and attenuates all others [62]. This does not alter the ν_0, however T_2^* and H_0, the peak height of the NMR line in the

frequency domain, are modified as

$$\frac{1}{T_2^*(\text{fil})} = \frac{1}{T_2^*} + \frac{1}{T_{\text{fil}}}$$

$$H_0(\text{fil}) = H_0 \frac{T_{\text{fil}}}{T_2^* + T_{\text{fil}}}$$

So that in the case where $T_{\text{fil}} = T_2^*$ the resultant Lorentzian amplitudes and linewidth will be halved compared with the bare FID case. This technique was only used whilst measuring T_1 by the $180° - \tau - 90° -$ FID pulse sequence. Here a series of measurements were made which all have the same time constant T_2^* but with varying amplitudes. T_2^* is established by fitting to an FID obtained for $\tau \gg 5T_1$ for which the magnetisation will have recovered to its equilibrium value. The resultant T_1 time constant is not effected by this procedure, however it aids in fitting data in the region where $\tau \approx \ln 2$ where $H \approx 0$.

7.3 ^{3}He NMR

In the initial NMR experiment isotopically pure ^{3}He was used as an adsorbate to calibrate the spectrometer and provide additional characterisation of the substrate. NMR measurements were made as a function of temperature, frequency and coverage. At low temperatures relaxation was dominated by quantum tunnelling and at higher temperatures motional narrowing of the NMR line was observed. The local fields were found to be ~ 3 times larger than for ^{3}He adsorbed on grafoil, indicating that the substrate fields dominate over the dipole-dipole interactions.

7.3.1 Magnet Homogeneity

For the bare ^{3}He adsorption experiment it was not possible to perform spin echo pulse sequences to directly observe T_2. T_2 was short and the magnet homogeneity high resulting in an insufficient separation of timescales between T_2 and T_2^*. Instead the magnet homogeneity was estimated by comparing linewidths at constant temperature for a range of Larmor frequencies and making the assumption that the field dependence of the relaxation times was negligible over the experimental range. T_2 has been shown to be proportional to frequency for 2D ^{3}He adsorbed on a graphite substrate [63], and as such the magnet homogeneity contribution to T_2^* must be treated as an upper bound.

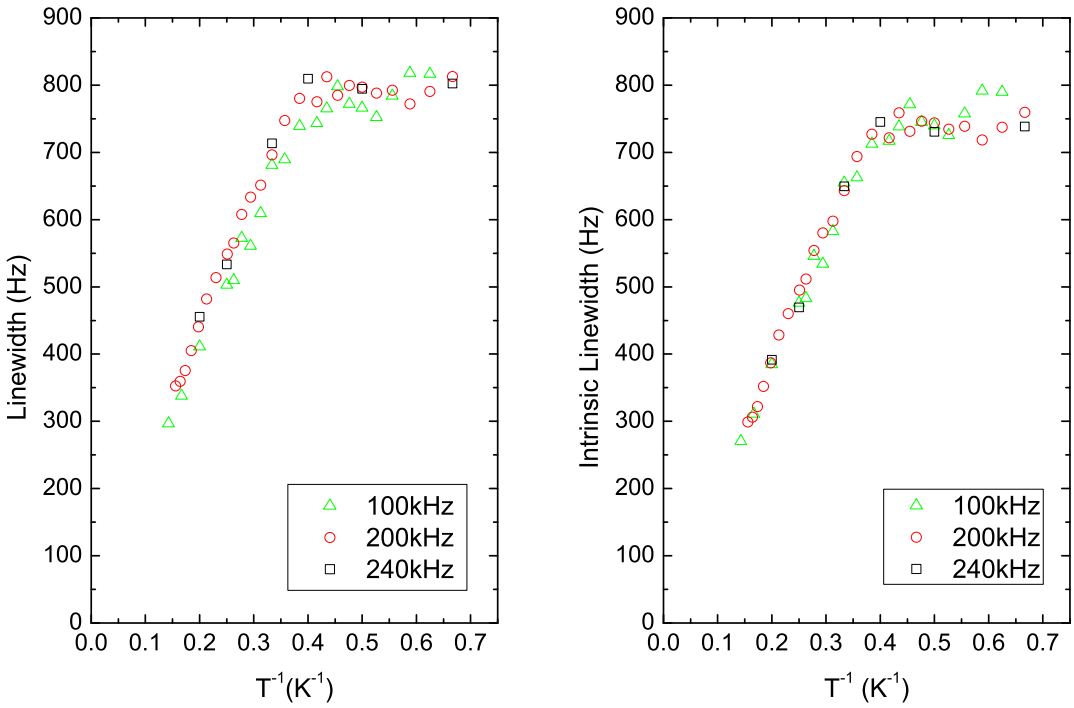

Figure 7.4: Measured and intrinsic linewidths for the ^{3}He experiment with $n_{3He}/n_1 = 0.88$. The magnet contribution to the measured linewidth is obtained by averaging gradient of the linewidth vs ν_0 at fixed temperatures above 2.5 K.

The measured linewidths of the resonance, shown in figure 7.4, are related to relaxation time constants by

$$\Delta\nu = \frac{1}{\pi T_2}, \qquad \Delta\nu^* = \frac{1}{\pi T_2^*} \tag{7.1}$$

where $\Delta\nu^*$ and $\Delta\nu$ are the intrinsic and magnet broadened linewidths respectively. From equation 3.13 the magnet contribution to the line width is

$$\Delta\nu^* = \Delta\nu + 2\nu_0 \frac{\Delta B}{B_0} \tag{7.2}$$

where ν_0 is the Larmor frequency and $\Delta B/B_0$ is the magnet inhomogeneity. $\Delta B/B_0$ was determined by averaging the gradient of $\Delta\nu^*$ vs ν_0 at constant T above 2.5 K, where T_2^* is motionally narrowed. $\Delta B/B_0$ was found to be 134 ppm, better than the calculated 400 ppm due to the presence of the overlapping superconducting cylinder.

7.3.2 Predicted Signal Size

The following signal size calculation follows the method described in [35]. Here the flux threading the receiver coil, ϕ_r, immediately following a NMR pulse is calculated using the principle of reciprocity [42] as

$$\phi_\mathrm{r} = M_0 v_s B'_{1,\mathrm{c}} \kappa \tag{7.3}$$

where M_0 is the initial magnetisation, $v_\mathrm{s} = 1.131\,\mu\mathrm{m}$ is the sample volume, $B'_{1,\mathrm{c}} = 384\,\mu\mathrm{T}$ is the field produce at the centre of the receiver coil by unit current flowing in the coil. The inhomogeneity factor $\kappa \approx 1$ allows for variation in B_1 across the

sample. The transverse magnetisation immediately following a perfect 90° pulse is equal to the equilibrium longitudinal magnetisation, M_0, given by equations 3.11 and 3.12. The flux transferred from the receiver coil to the SQUID is determined by equation 4.7 for the flux transformer gain, so that the flux threading the SQUID is given by

$$\phi_{\mathrm{SQ}} = \frac{M_{\mathrm{i}}}{(L_{\mathrm{i}} + L_{\mathrm{r}})} \frac{\hbar^2 \gamma B_{1,\mathrm{c}} \kappa}{4 k_{\mathrm{B}}} \frac{N_V \omega_0}{T} \tag{7.4}$$

where $\omega_0 = \gamma B_0$ is the Larmor frequency and for the input coil fabricated on the C2 SQUID array chip $M_{\mathrm{i}}/(L_{\mathrm{i}} + L_{\mathrm{r}}) = 2.992 \times 10^{-4}$. Therefore the expected signal magnitude at zero time, $H_0 = 4.72 \times 10^{-45} N_{\mathrm{v}} \omega_0 / T$ Wb.

The amplitude of the output voltage for the FID envelope is determined by the FLL gain of the SQUID electronics which in section 5.2 is shown to be $G_{\mathrm{FLL}} = R_{\mathrm{f}}/M_{\mathrm{f}}$ so that

$$V_{\mathrm{OUT}} = G_{\mathrm{FLL}} \phi_{\mathrm{SQ}} = \frac{R_{\mathrm{f}}}{M_{\mathrm{f}}} \phi_{\mathrm{SQ}} \tag{7.5}$$

The measured value of the FLL gain was $G_{\mathrm{FLL}} = 2.46\,\mathrm{V}/\phi_0$. Therefore the expected time domain signal voltage at zero time is given by,

$$V_{\mathrm{OUT}} = 5.61 \times 10^{-30} N_{\mathrm{v}} \omega_0 / T \ \mathrm{V} \tag{7.6}$$

7.3.3 Non-exponential decay

For the pure ^{3}He experiment the transverse and longitudinal relaxations were found to be non-exponential. In the case of transverse relaxation, where we fit to the FFT of the FID in the frequency domain, the calculated value of T_2^* and the initial signal amplitude, A, were found to change with capture delay. For the case of longitudinal

relaxation, where the magnetisation is traced out in the time domain, a stretched exponential of the form $\exp[\tau/T_1]^\alpha$, where α is a fitting parameter, was found to best describe the decay.

Transverse Relaxation and Magnetisation

In general the NMR free induction decays were found to be non-exponential. The transverse relaxation time, T_2^*, is determined by fitting a Lorentzian function to the square of the magnitude of the FFT of the FID data. This was observed to be approximately Lorentzian in all cases, as illustrated in figure 7.5, however small changes were observed as the dead time between NMR readout pulse and data capture was varied

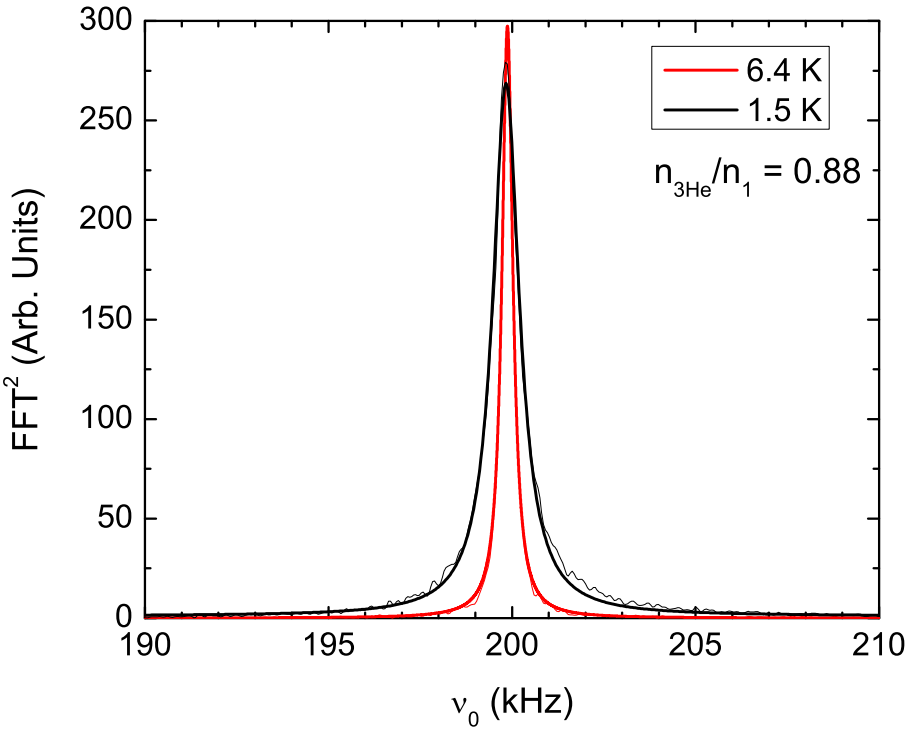

Figure 7.5: Examples of fitting a Lorentzian to the square of the magnitude of the FFT of FIDs obtained by 90° – FID pulse sequence.

Data for coverage $n_{3He}/n_1 = 0.96$ is used here as an example of the general behaviour of the system and to illustrate the method of analysis. In figure 7.6 T_2^* data at $n_{3He}/n_1 = 0.96$ corresponding to different capture delays, τ, are shown for temperatures between 1.5 and 6.43 K. Here τ is the delay time between the centre of the tipping pulse and the start of data capture. The data set at each temperature is obtained from a single FID, and τ was increased by truncating the data set, removing data from the beginning of the data file. The time constant T_2^* is found to vary slightly with τ and in order to compare data recorded with different values of τ, the T_2^* relaxation times were extrapolated back to $\tau = 0$.

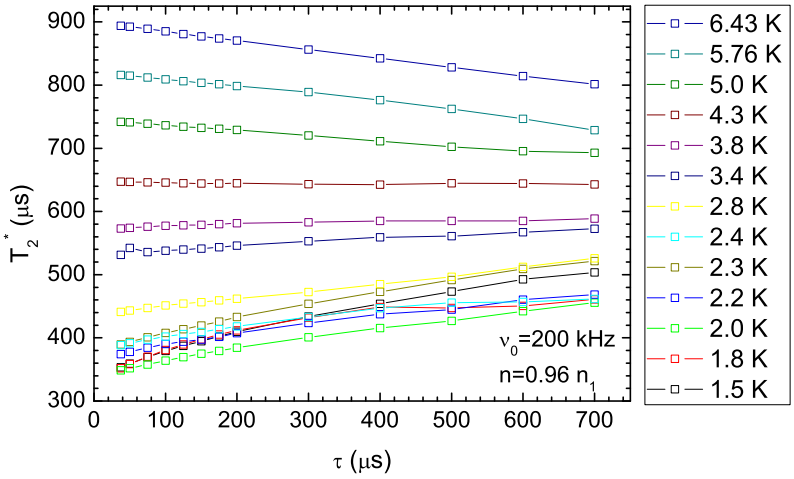

Figure 7.6: T_2^* relaxation times as a function of the capture delay τ. The relaxation time was found to be dependent on τ and the sign of the dependence is observed to change as a function of temperature.

The data resulting in the T_2^* relaxation times shown in figure 7.6 and data for higher coverages were recorded with $\tau = 37.5\,\mu$s with 90 degree tipping pulse lengths $\tau_{90} = 25\,\mu$s. The data at $n_{3He}/n_1 = 0.88$ were taken for $\tau = 125\,\mu$s with $\tau_{90} = 50\,\mu$s. These data were taken before improving the measurement technique allowing for shorter dead times.

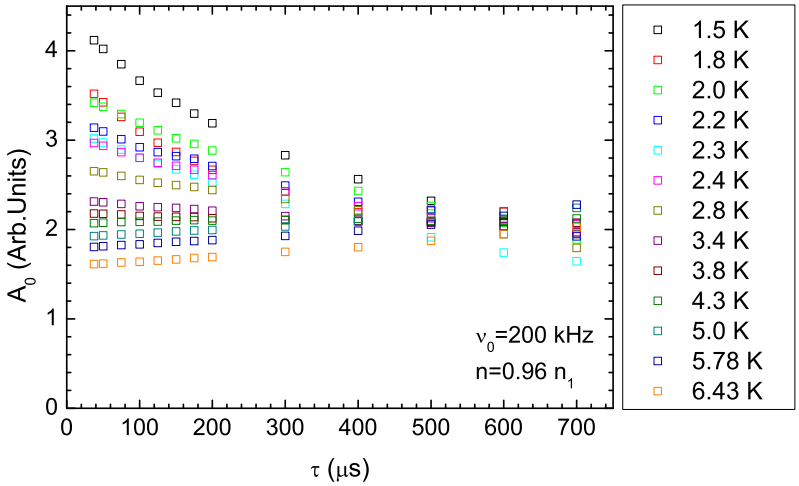

Figure 7.7: A_0 vs Capture Delay. At low temperatures the extrapolated value of A_0 is significantly larger than the $A_0(\tau)$ for $\tau = 37.5\,\mu s$ which is the value at data capture.

The initial amplitude of the FID in the time domain, A_0, is calculated from the parameters of the fitted Lorentzian using equation 3.18, which can be compared directly with the predicted value given by equation 7.6. Assuming an exponential decay the initial signal amplitude can be calculated from the amplitude after a time τ using the relation

$$A(\tau) = A_0(\tau)e^{-\tau/T_2^*} \tag{7.7}$$

Due to the non-exponential decays the value of A_0 will also depend on the capture delay. Figure 7.7 shows the calculated value $A_0(\tau)$ determined using $A(\tau)$ and $T_2^*(\tau)$. Extrapolating back to $\tau = 0$ gave a value for A_0.

The system magnetisation is expected to exhibit Curie type behaviour over the experimental range. Since the initial signal size, A_0, is proportional to the magnetisation, A_0T/B_0N_v is expected to be constant for all cases. Here B_0 is the NMR field and N_v is the number of observable spins. Figure 7.8 shows A_0T as a function of τ for constant B and N_v. For Curie magnetisation we expect the vales of A_0T to

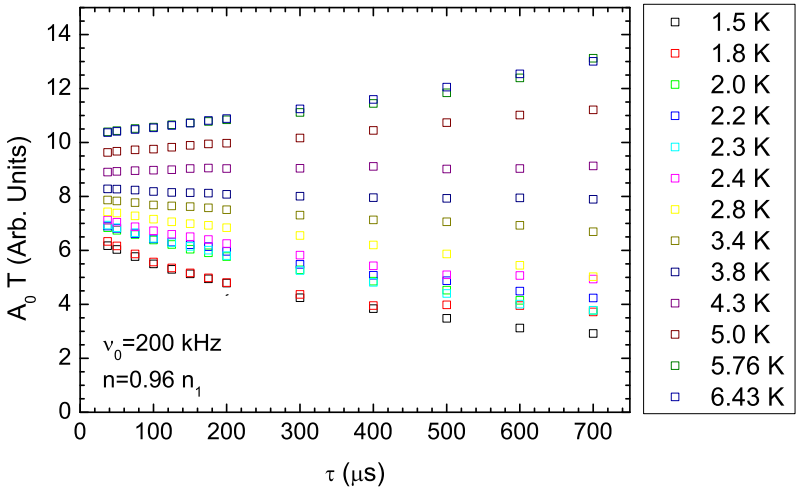

Figure 7.8: For Curie like behaviour A_0T is expected to be independent of temperature. The temperature dependence here is attributed to fitting errors. It can be seen that as the capture delay is reduced the apparent deviation from Curie law is reduced.

be independent of temperature and here we see that as τ decreases the temperature dependence is reduced.

A_0T/B_0N for $\tau = 0$ is plotted in figure 7.9 as a function of temperature and of coverage. A_0T/B_0N was found to be constant with increasing N, shown in figure 7.9(b), indicating that all of the spins are observed at each temperature. A small amount of signal was gained for coverages above monolayer completion.

A_0T/B_0N was found to have some temperature dependence shown in figure 7.9(a). This is believed to be due to fitting errors as the line broadens at low temperatures and not due to the sample not cooling. To ensure that the sample was not being heated though the application of the RF pulses, a number of NMR measurements were performed as a function of repeat time. For the majority of experiments performed in this work the NMR repeat time was 1.6 s, as this is the shortest time interval at which the scope triggers reliably. Increasing the repeat time by an order

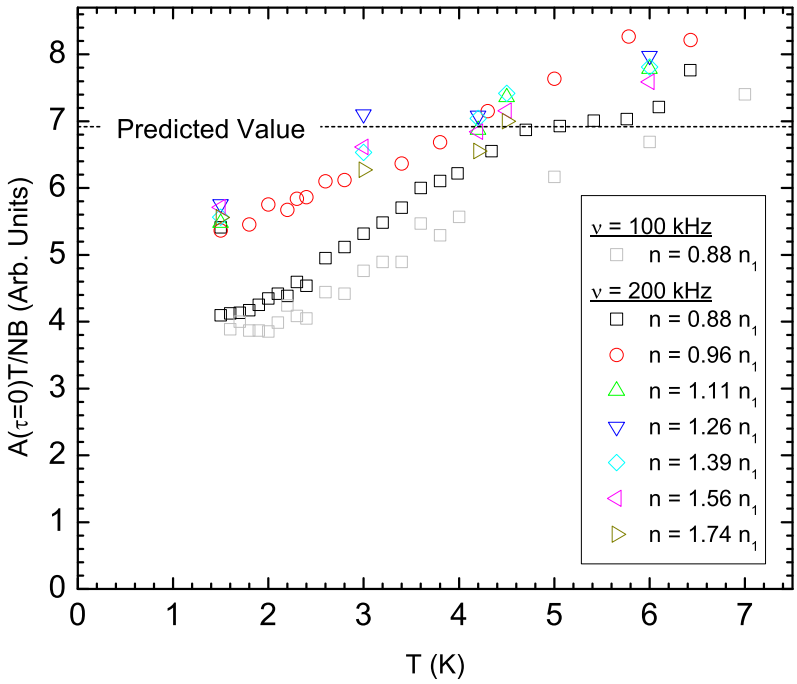

(a)

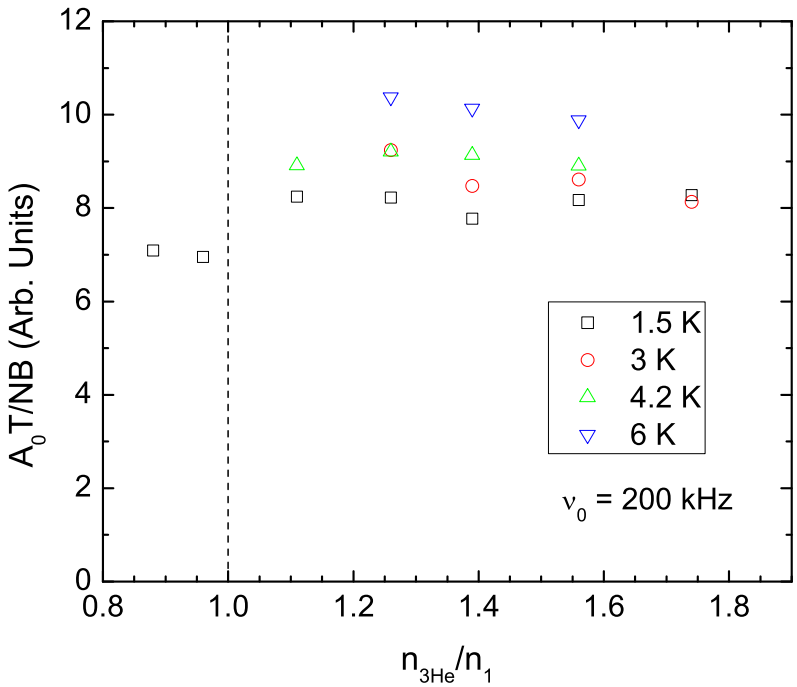

(b)

Figure 7.9: Reduced magnetisation vs (a) temperature and (b) number of spins. This shows a slight temperature dependence and a small amount of signal is gained for coverages above monolayer.

of magnitude to 16 s did not change the observed signal magnetisation or T_2^* beyond the experimental error.

In figure 7.9(a) the data for $n_{3He}/n_1 = 0.88$ were taken for $\tau = 125\,\mu s$ with $\tau_{90} = 50\,\mu s$. The experimental technique was improved for the measurements at higher coverages and at all other coverages $\tau = 37.5\,\mu s$ where $\tau_{90} = 25\,\mu s$. This results in the observed magnetisation at $n_{3He}/n_1 = 0.88$ being significantly lower than at higher coverages and the data are not directly comparable. However they are included to show that the reduced magnetisation is frequency independent.

Longitudinal Relaxation

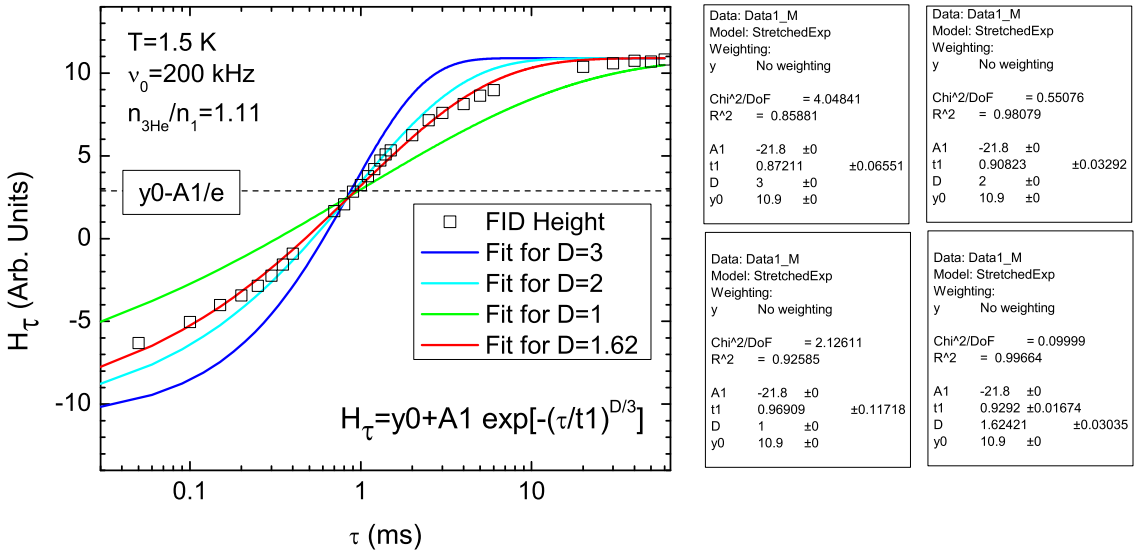

Figure 7.10: Stretched exponential fits to T_1 data for different values of d, relating to different dimensionalities.

The longitudinal relaxation was in general non-exponential, instead the decay resulting from a $180° - \tau - 90°$ is better described by a stretched exponential of the form

$$H_\tau = H_\infty - (H_\infty - H_0)\, e^{-(\tau/T_1)^{d/3}} \tag{7.8}$$

Here H is the height of the signal in the frequency domain. H_∞, the value of H_τ for $\tau \to \infty$, is constrained as the signal height following a $90° - $FID pulse. As we are able to produce accurate 180° pulses, in most cases it is appropriate to constrain H_0 as $-H_\infty$. In this case it is probably due to having a range of relaxation time constants, relating to spins in the first and second layers and other relaxation centres. It was not possible to fit reliably two exponentials to the data. Non-exponential relaxation can also be a characteristic of a low dimensional dilute solid [20] where d is the dimensionality of the system, although that is not the case in this experiment.

Figure 7.10 shows T_1 data with fits for different values of d, where the data are best fitted for d=1.62, but is close to the expected d=2 for a two dimensional solid. For these data H_∞ was measured by $90° -$ FID to be 10.9, and H_0 constrained to be $-H_\infty$. The dashed line represents the point where the signal height has decayed to $(H_\infty - H_0)/e$ of its initial value, so that its interception with the fits occurs at T_1 for $d = 3$. Figure 7.10 illustrates how this method is robust to changes in d. In general T_1 will be taken as the time corresponding to the signal falling to $1/e$ of its initial value. For good 180 °pulses this is equivalent to

$$T_1 = \tau_0 / \ln 2 \tag{7.9}$$

where τ_0 is the time corresponding to $H = 0$, the zero crossing point of the relaxation. In figure 7.11 the fitted values for d for T_1 data for all temperatures and coverages at $\nu_0 = 200\,\mathrm{kHz}$ are plotted.

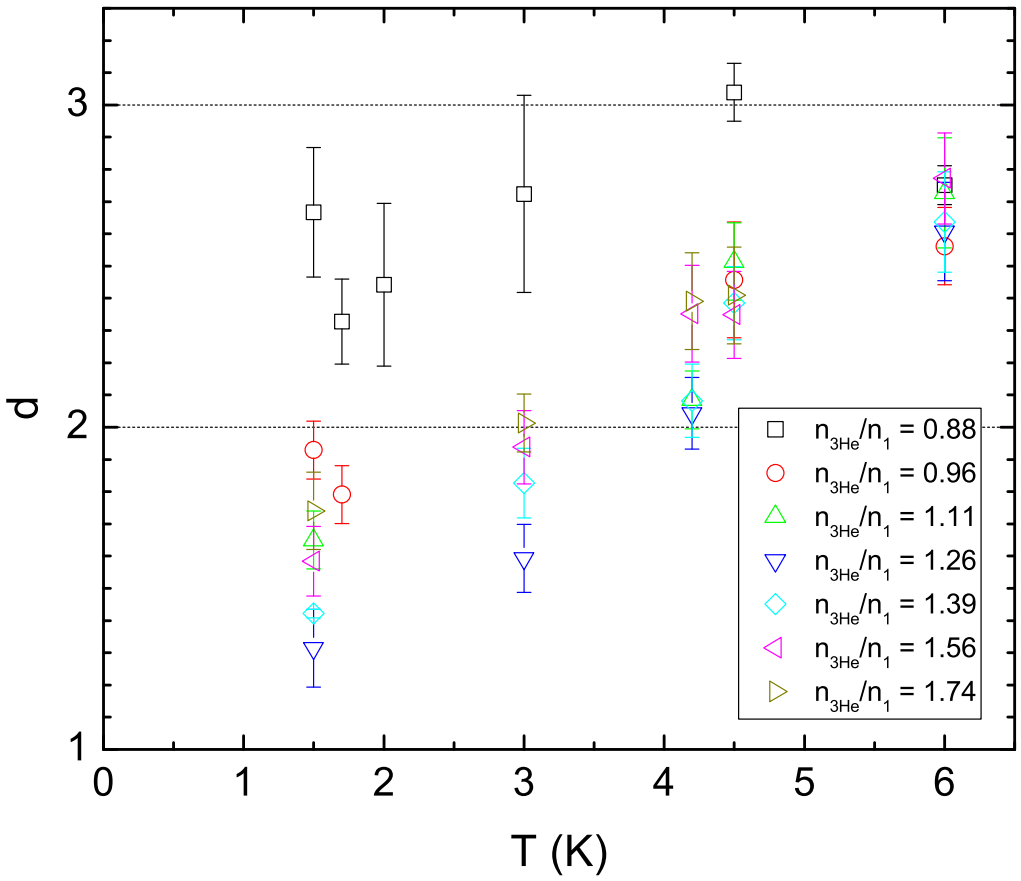

Figure 7.11: d is the index of the stretched exponential obtained by fitting to T_1 data, from equation 7.8. d is shown as a function of temperature for different coverages. At the lowest coverage d is significantly larger than for the higher coverages. This may suggest that there is a different relaxation time associated with the second layer.

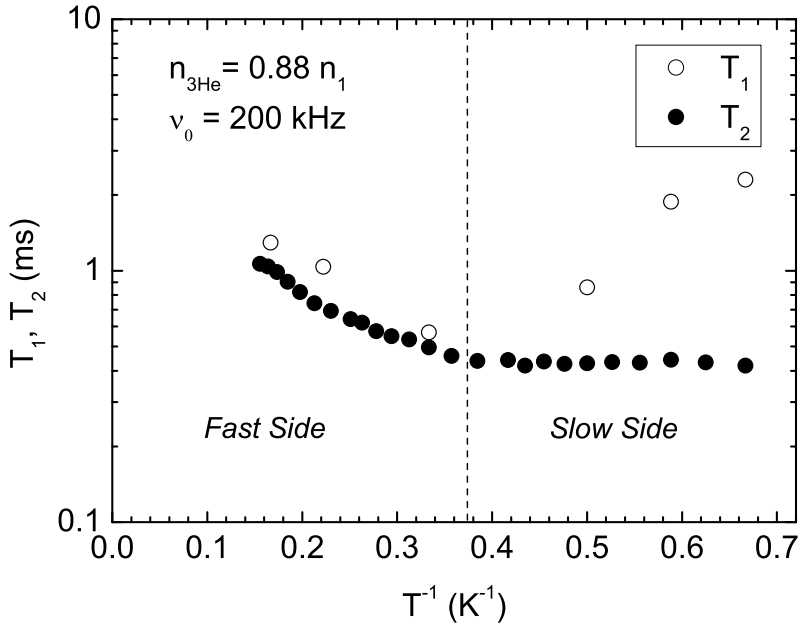

Figure 7.12: Relaxation times as a function of temperature showing $T_1^{(\min)}$.

7.3.4 Relaxation as a Function of Temperature

A survey of T_1 and T_2 data was taken for $n_{3He}/n_1 = 0.88$ as a function of temperature predominantly at $\nu_0 = 200\,\text{kHz}$, as the signal-to-noise was adequate at this frequency. A minimum in T_1 was observed for $n_{3He}/n_1 = 0.88$ at $\nu_0 = 200\,\text{kHz}$, shown in figure 7.12, where at the minimum the correlation time is given appoximately by $\tau_c \sim \omega_0^{-1}$. For temperatures higher than $T(T_1^{(\min)})$ the correlation time $\tau_c < \omega_0^{-1}$ and is generally referred to as the "fast" side of $T_1^{(\min)}$. Conversely for temperatures below $T(T_1^{(\min)})$, $\tau_c > \omega_0^{-1}$ and is referred to as the "slow" side of $T_1^{(\min)}$.

Using the NMR "rule of thumb" that in the motional narrowing regime

$$\frac{1}{T_2} = M_2 \tau_c \tag{7.10}$$

where M_2 = is the second moment of the rigid lattice linewidth, and as at the

minimum $T_1 \sim T_2$ we can say the value of T_1 at the minimum is

$$T_1^{(\min)} \sim \frac{2\pi\nu_0}{M_2} \tag{7.11}$$

From the value of the T_1 minimum we obtain $M_2 = 2.2 \times 10^9\,\mathrm{s}^{-2}$. M_2 is related to the local field strength as $M_2 = \gamma^2 < B_{\mathrm{loc}}^2 >$ where $< B_{\mathrm{loc}} >$ is the mean-squared value of the local field. For ^{3}He where $\gamma/2\pi = 32.44\,\mathrm{MHz\,T}^{-1}$ this gives a local RMS field strength of $2.3 \times 10^{-4}\,\mathrm{T}$. The local field strength is the same as measured previously [64], and is a factor of ~ 3 higher than the monolayer dipole-dipole field strength observed for ^{3}He adsobed on grafoil [63].

For a solid crystal lattice we would expect T_2 to be temperature-independent at low temperatures where $\tau_c \gg 2\pi\nu^{-1}$. Here we expect

$$\frac{1}{T_2} = \gamma < B_{\mathrm{loc}}^2 >^{1/2} \sim M_2^{1/2} \tag{7.12}$$

At low temperatures T_2 levels off at $\sim 420\,\mu\mathrm{s} \gg M_2^{-1/2} = 21\,\mu\mathrm{s}$, implying significant motional narrowing of the line due to quantum tunnelling. On the "fast"side of the T_1 minimum, we would ordinarily expect $T_1 = T_2$. The inequality of T_1 and T_2 is characteristic of two dimensional diffusive motion in the local magnetic fields [65]. On the fast side of $T_1^{(\min)}$ the transverse relaxation is found to be consistent with an activation energy of the form $T_2 \sim \exp[-\Delta/k_{\mathrm{B}}T]$, shown in figure 7.13. The activation energy $\Delta/k_B = 4.01\,\mathrm{K}$ observed between 2.4 and 4.7 K is similar to the $\Delta/k_B = 3.8\,\mathrm{K}$ value reported previously for a similar substrate at this coverage [64]. This is significantly smaller than the value of $\Delta/k_B = 27\,\mathrm{K}$ reported for ^{3}He adsorbed on grafoil for the same coverage [63]. The change in the activation energy was also observed for the ^{3}He adsorbed on grafoil experiment where this was attributed to

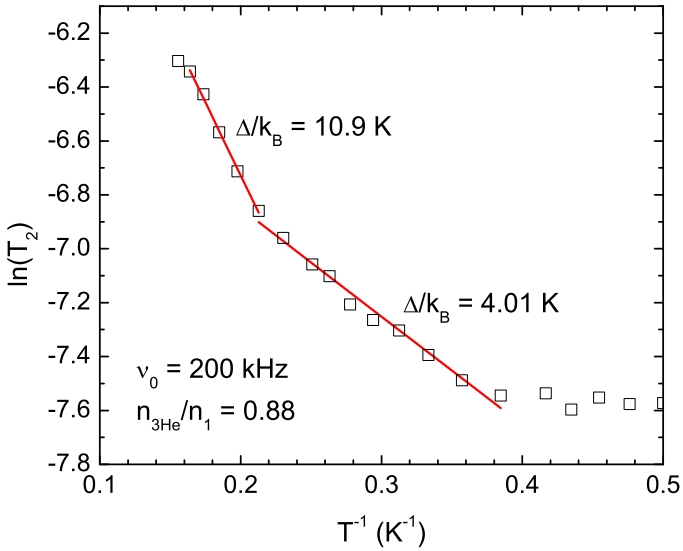

Figure 7.13: Thermal activation energy of T_2^*. At low temperatures motion is dominated by temperature independent quantum tunnelling whilst at higher temperature it is dominated by thermally activated motion. The increase in the activation energy could be due to a change in phase or in the dimensionality of the system. In previous work for ^{3}He on grafoil this has been attributed to melting of the 2D solid.

the melting of the 2D solid, observed in heat capacity measurements for the same temperature and coverage [66].

7.3.5 Relaxation as a Function of Coverage

In figure 7.14 we observe motional narrowing of the transverse NMR line at high temperatures. At the lower temperatures T_2^* is independent of T due to quantum tunnelling. In the motionally narrowed region T_2^* is increasing slightly with coverage. At low temperatures, there is a weak T_2 minimum observed at layer completion as observed in other 2D ^{3}He systems [65].

T_1 at low temperatures decreases approaching layer completion and is approximately constant through the second layer. This is similar to the behaviour observed pre-

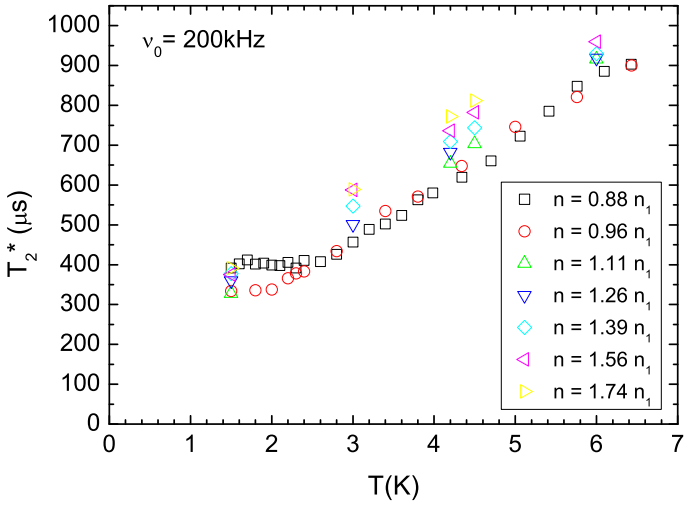

Figure 7.14: A plot showing T_2^* as a function of temperature for different ^{3}He coverages. At higher temperatures thermally activated motional narrowing dominates the relaxation times. In this region T_2^* is generally increasing with increasing coverage. At lower temperatures the relaxation T_2^* is dominated by quantum motion and in this case a minimum in the relaxation time is observed at monolayer completion. This is illustrated by the change in T_2^* at 1.5 K as the coverage is increased from $n_{3He}/n_1 = 0.88$ to 0.96

viously for ^{3}He on grafoil [63, 67]. Indications of further T_1 minima were observed at a number of coverages above $n_{3He}/n_1 = 0.88$, although in all cases there were insufficient data to give their positions.

7.4 Low Density ^{3}He NMR on a ^{4}He Preplated Substrate

The conditions for the observation of a quasi-1D ^{3}He system are quite stringent [4]. In particular an extremely low coverage of ^{3}He is required, which makes signal sensitivity a real issue. The Fermi energy of a non-interacting 1D Fermi gas is given by $k_B T_F^{(1D)} = \left(\hbar^2 \pi^2 n_{1D}^2 / 8m\right)$, where n_{1D} is the 1D line density, and m is the ^{3}He

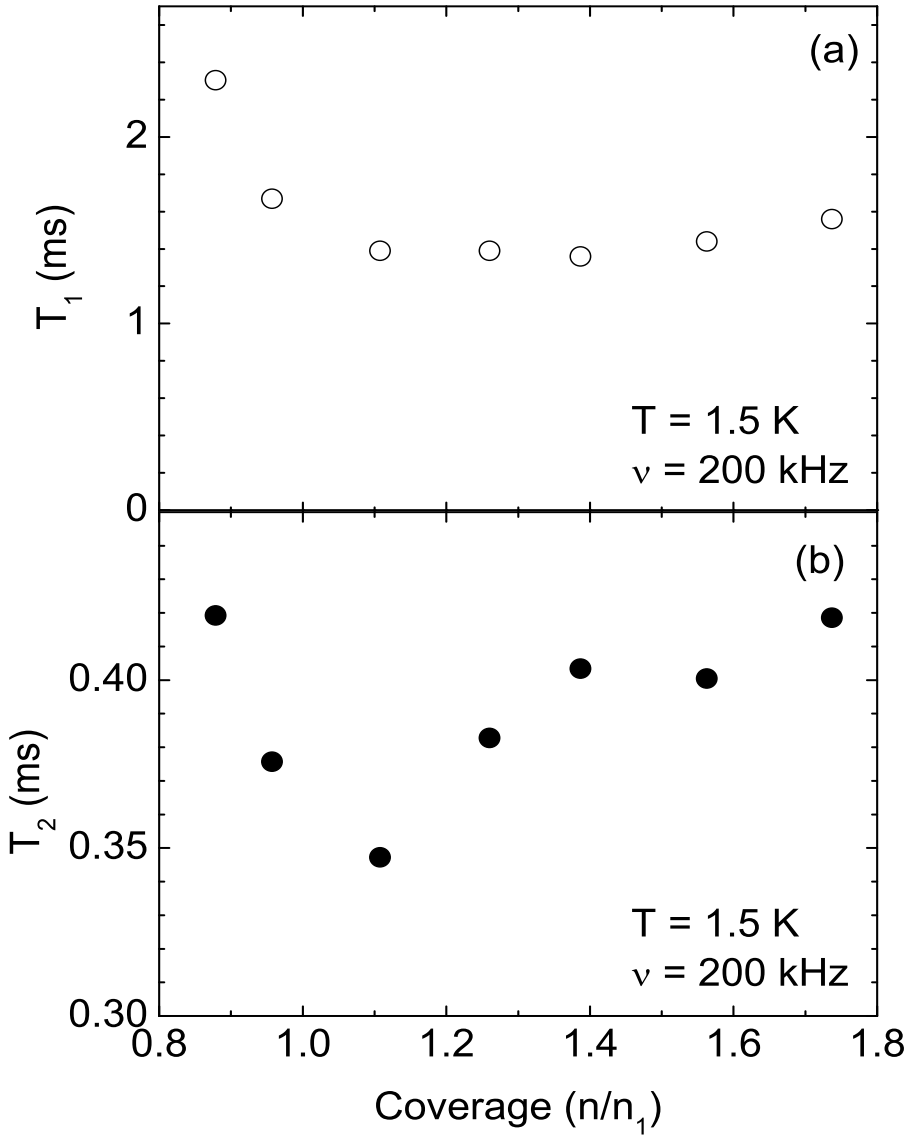

Figure 7.15: T_1 and T_2 as a function of coverage at $T = 1.5\,\mathrm{K}$. (a) The decrease in T_1 as the coverage approached monolayer completion may be due to the random orientation of the pores as similar behaviour has been observed for ^{3}He adsorbed on grafoil as the angle between the basal plane and the applied field is varied [67]. (b) The minimum in T_2^* as $n_{3\mathrm{He}}/n_1$ is characteristic of 2D adsorbed ^{3}He [65].

mass. In order to realize a 1D system the Fermi energy $k_B T_F^{(1D)}$ must be less than Δ, the energy difference between the ground state and the first excited azimuthal state for ^{3}He in the ^{4}He preplated pores. In addition the temperature must be much less than $\Delta/k_B - T_F^{(1D)}$. The eigenstates of bare, non-interacting ^{3}He atoms have been calculated for ^{4}He coated pores [4, 5], resulting in an energy difference Δ of ~ 800 mK for 23 Å pores with a 1.1 layer ^{4}He film. Since $T_{F1D} \propto n_{1D}^2$ the conditions require very small ^{3}He coverages ($T_F^{(1D)} \approx 100$ mK at a coverage of 0.01 monolayer for 23 Å pores).

For this reason we have investigated the NMR relaxation times for $n_{3He} = 0.01 n_1$ on MCM-41 preplated with $n_{4He} \geq 1.05 n_1$. Here n_1 is the ^{4}He monolayer density as determined by the minimum in the isothermal compressibility κ_T of ^{4}He. At this ^{3}He coverage the sample contained 1.24×10^{19} spins. The feasibility of the measurement is determined in part by the magnitude of the relaxation times. Figure 7.23 shows the temperature and frequency dependence of T_1 and T_2^*. The measured times were in general longer than those observed with the high density films, enabling sufficient SNR with the 30 h SQUID. Figures 7.21 and 7.22 also shows the effect of doubling n_{3He} to $0.02 n_1$. Within the scatter there was little change in the measured relaxation times, suggesting that the relaxation is associated with single particle processes.

There was a finite vapour pressure at temperatures above base temperature for the lower ^{4}He coverages and even at base temperature for the higher ^{4}He coverages. We expect that a significant fraction of the ^{3}He will be in the gaseous state and is discussed further in section 7.4.6.

7.4.1 NMR signals from 0.01 monolayer ^{3}He

With the upgraded C5 SQUID array it was possible to observe NMR signals from 0.01 monolayers of ^{3}He, which was 1.24×10^{19} spins. This is 88 times fewer spins than for the lowest coverage in the previous experiment. In order to take advantage of the improved sensitivity of the upgraded spectrometer it was necessary to suppress sources of noise which were small compared to the SQUID noise for the previous experiment, but became dominant for this setup. This included improving the cryostat grounding, increasing the number of crossed-diodes in the transmitter box and opto-isolating various apparatus involved in creating and timing transmitter pulses.

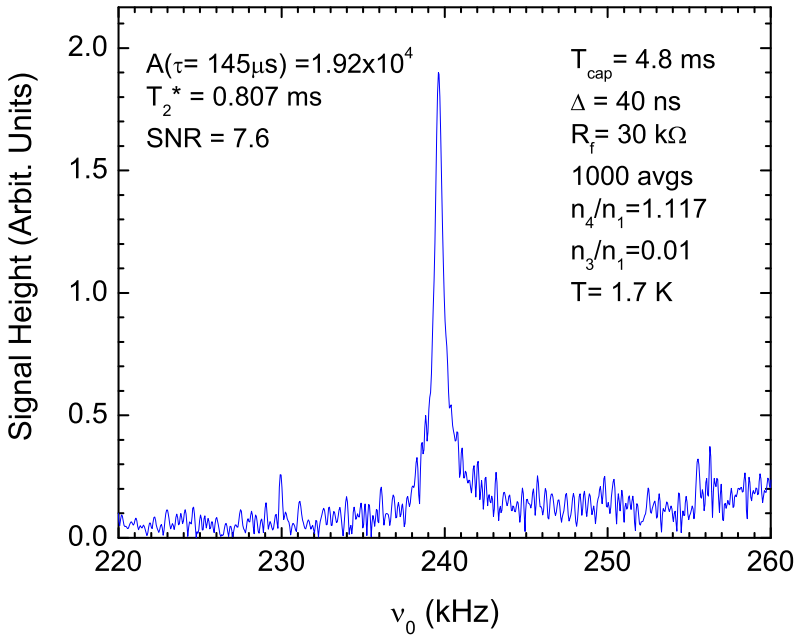

Figure 7.16: FID at 1.7 K and 240 kHz following a 100 μs 90° pulse. Data capture began 95 μs after the 90° readout pulse. The SNR was 7.6

An example FFT of a NMR relaxation following a $90° - \text{FID}$ pulse is shown in figure 7.16. Here the on-resonance pulse was applied at $\nu_0 = 240$ kHz with a background at 240 kHz. A 100 μs 90° pulse was used and so that minima in the power spectrum

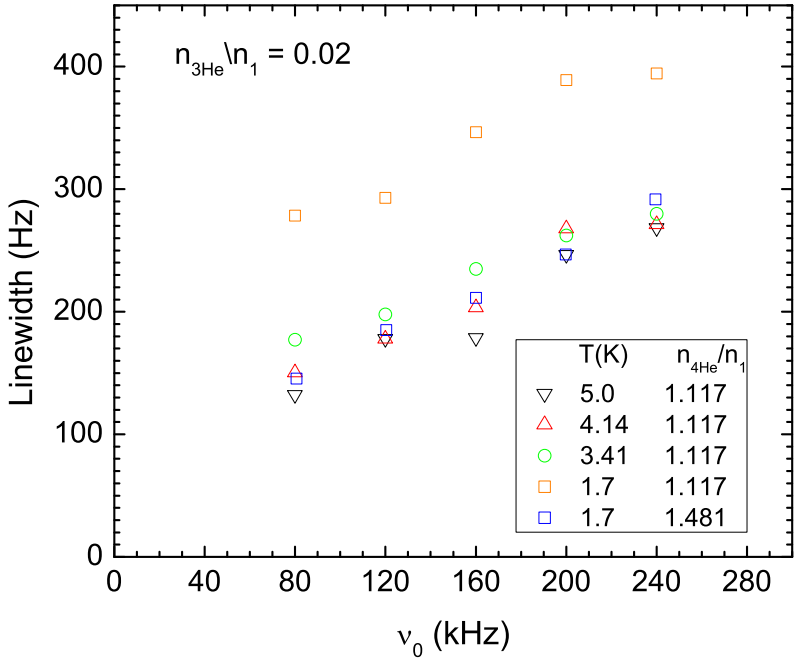

Figure 7.17: Linewidth $\Delta\nu^*$ vs ν_0 showing a constant gradient. This indicates that the gradient is due to magnet inhomogeneity.

occur at 40 kHz intervals. The signal-to-noise ratio (SNR) for 1000 averages was 7.6, which is equivalent to 0.24 in a single shot. It was not possible to capture data as close to the tipping pulse as for the previous experiment, however this was compensated in part by the increase in T_2^*.

7.4.2 Magnet Homogeneity

Frequency Dependence of T_2^*

The frequency dependence of T_2^* was stronger for the preplated experiment than for the bare substrate. The gradients of linewidth versus frequency plots, shown in figure 7.17 were independent of temperature and coverage indicating an inhomogeneous broadening due to the magnet. An average of the linear fits to data at a range of

coverages and temperatures gave a magnet contribution to the linewidth of 162 Hz at $\nu_0 = 200$ kHz which is equivalent to $\alpha = 407$ ppm. This is approximately a factor of 4 larger than observed for the bare ^{3}He case in section 7.3.1, the reason for which is not fully understood. Between the two runs the grounding for the overlapping shield was improved to try to reduce the magnitude of the transient following NMR pulses, and the pressure gauge was added to the cell plate. Both of these changes may have contributed to the decreased homogeneity.

Spin Echoes at High Coverages

Above the second minimum in the isothermal compressibility κ_T, T_1 and T_2 increase rapidly with coverage. This provided the necessary separation of time scales to observe spin echoes. The observation of spin echos with SQUID detection had not previously been achieved at Royal Holloway. To perform a spin echo pulse sequence it is necessary to apply phase coherent NMR pulses. Phase coherance in conventional NMR systems is usually achieved by gating a master oscillator, however due to the sensitivity of SQUID detection the cross-coupling from the leakage current through the gate make this method unsuitable. Here the pulses are created individually using Agilent waveform generators triggered by a Stanford DG535 Digital Delay Generator clocked from SRS SC10 10 MHz ovenized quartz master oscillator, described in greater detail in section 4.4. Using this system there is no leakage current at the Larmor frequency when pulses are not being applied.

The method of calculating the echo height using the $90° - \tau_1 - 180° - \tau_1 -$ echo

pulse sequence is as follows. The height of the echo decays as

$$E_\tau = E_0 \exp[\tau/T_2] \tag{7.13}$$

where $\tau \approx 2\tau_1$ is the time interval between the midpoint of the initial 90° pulse and the peak of the echo. E_0 is determined by taking an FID and extrapolating its hight back to $\tau = 0$. For $\tau \neq 0$ we must wait a few T_2^* for initial FID to decay to a suitably low level before applying the 180° pulse.

When the echo is captured post-processing is required to increase the signal-to-noise ratio. First a polynomial background subtraction routine is performed in LabVIEW using the LU Decomposition routine. An FFT routine is then applied with zero padding and a gaussian filter is applied to the frequency domain signal centred on the Larmor frequency. A further FFT is applied to reveal the echo in the time domain. The position of the echo peak is noted to ensure that the echo is occurring at the correct time and the peak height of the echo is recorded. An example of fitting to the spin echo data is shown in figure 7.18. An exponential function was fitted to the data directly to ensure that the errors are weighted correctly.

With independently measured values of T_2 and T_2^* it is possible to determine the magnet homogeneity across the sample as $\alpha = \Delta B/B$ as

$$\alpha = \frac{\Delta\nu^* - \Delta\nu}{2\nu_0} \tag{7.14}$$

Figure 7.19 shows a measurement of α as a function ν_0. The mean value of the magnet homogeneity $\alpha = (368 \pm 7)$ ppm, which is close to the estimated value from the slope of the linewidth vs frequency plots, figure 7.17. This indicates a slight

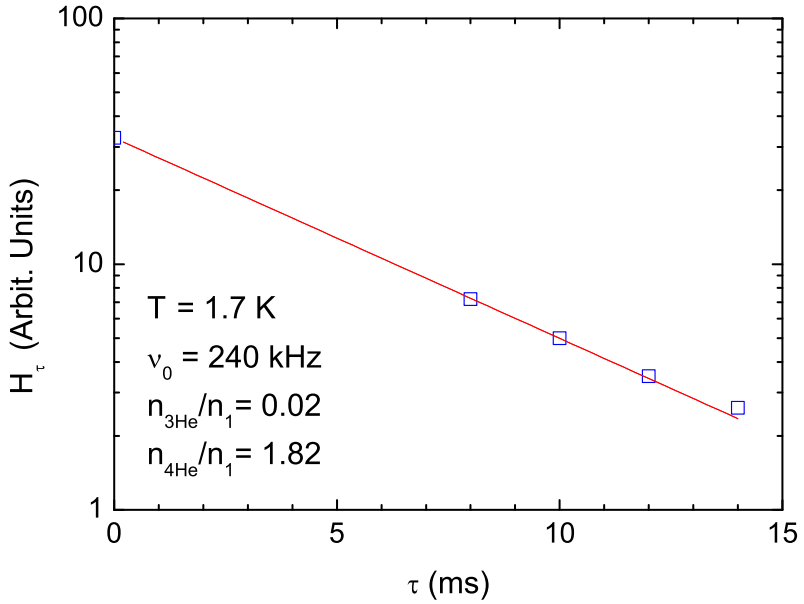

Figure 7.18: An example of fitting T_2 by spin echo. The signal height at $\tau = 0$ is obtained by $90° - \text{FID}$ and for finite values of τ from the spin echo produced by a $90° - \tau - 180° - \text{Echo}$ pulse sequence.

frequency dependence of the intrinsic T_2, which is shown in figure 7.26.

7.4.3 NMR Lineshape

In general the decays were observed to be exponential in time for all of the preplated data. Figure 7.20 shows an example T_1 decay lineshape at the lowest temperature. This is in contrast to the pure ^{3}He case presented in figure 7.6. This indicates that a single relaxation mechanism is dominant for all of the spins or that there is rapid interchange.

T_2^* was also more exponential than for the pure ^{3}He case, being independent of the dead time between pulse and data capture. Where observable, T_2 was found to be fitted well by an exponential as shown in figure 7.18.

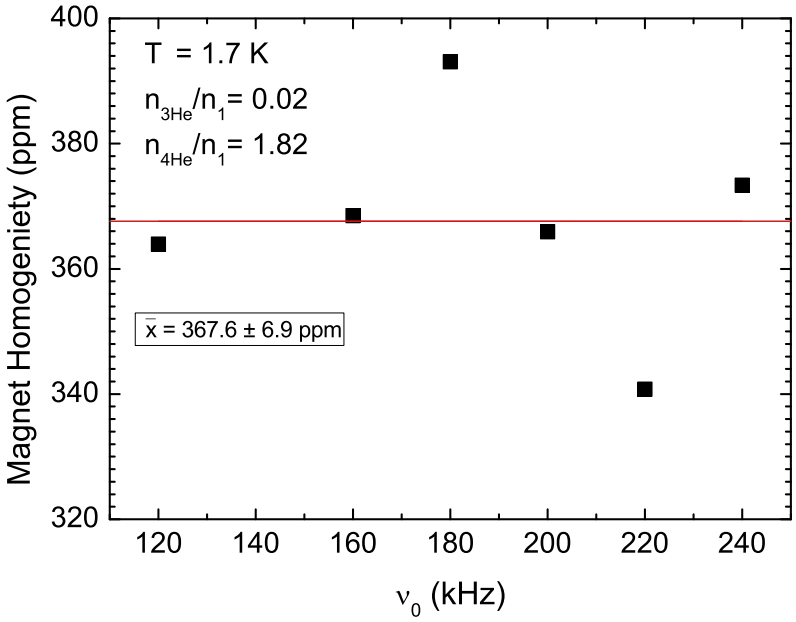

Figure 7.19: Determination of the magnet homogeneity by spin echo measurements. The magnet homogeneity was calculated at different frequencies using equation 7.14 and averaged to give $\alpha = (368 \pm 7)$ ppm

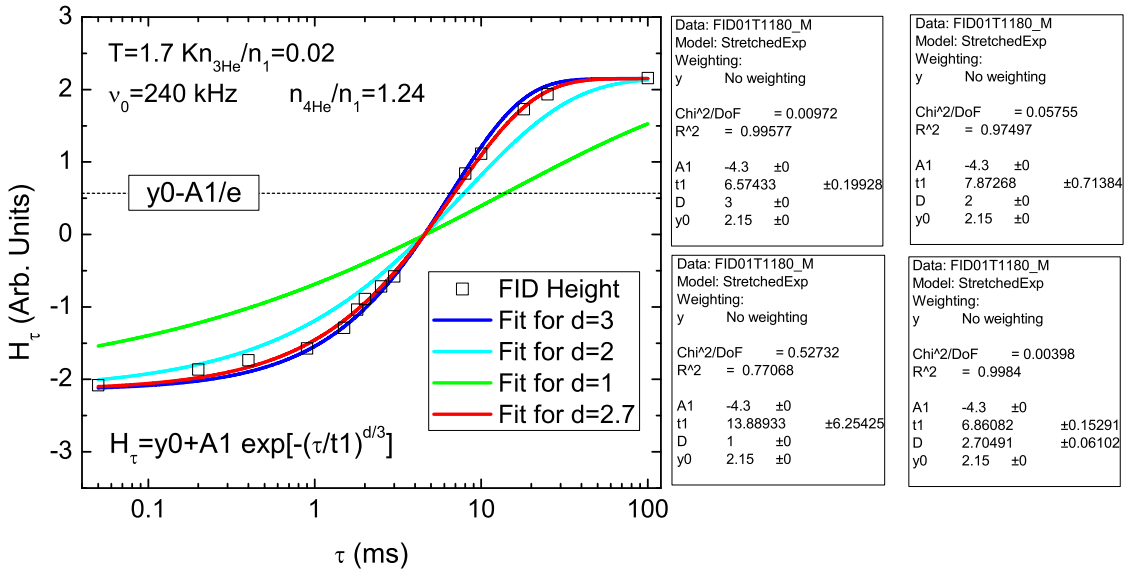

Figure 7.20: An example T_1 fit at 1.7 K and $\nu_0 = 240$ kHz for the preplated experiment. Here the decay is very close to exponential, which is in contrast with the strongly non-exponential decay under similar conditions shown in figure 7.10

7.4.4 Effect of changing the ^{3}He coverage

For this experimental run we initially added ^{4}He to the cell, before adding any ^{3}He. The ^{3}He was not added to the sample until the $n_{4He}/n_1 > 1$ due to concerns that the ^{3}He would get bound to high binding potential locations in the first layer. 0.01 monolayer of ^{3}He was first added at $n_{4He}/n_1 = 1.117$. Initial NMR experiments were performed without annealing the cell following the addition of the ^{3}He. No change in the relaxation times or in the magnetisation was observed outside of the experimental after annealing the cell at 1 mbar for 1 hour.

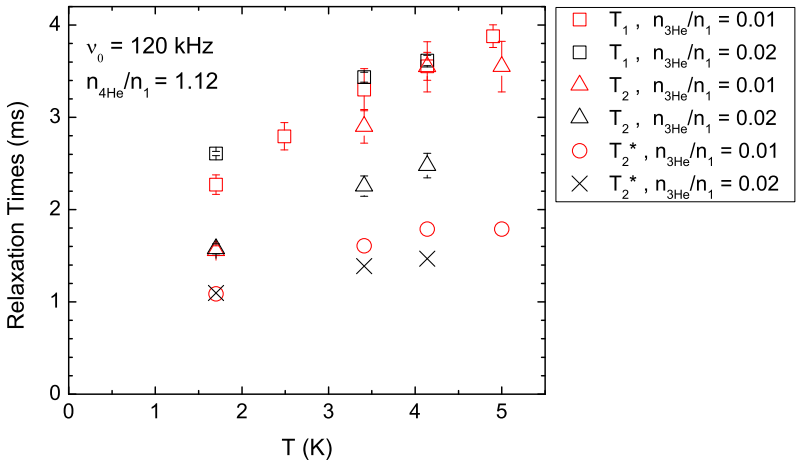

Figure 7.21: Relaxation times vs T for $n_{3He}/n_1 = 0.01$ and 0.02 at $\nu_0 = 120$ kHz. The apparent change in T_2 between the coverages is due to fitting errors occurring due to the small signal size.

Measurements of T_1, T_2^* and the magnetic susceptibility, χ, were taken for $n_{4He}/n_1 = 1.12$ and $n_{3He}/n_1 = 0.01$ over the accessible range of T and ν_0. Since both T_1 and T_2^* increase on warming, the system is on the "fast" side of a T_1 minimum. Figures 7.21 and 7.22 show T_1 and T_2 both increasing with temperature. As at the $T_1^{(\min)}$ we find $\tau_c = \omega_0^{-1}$ we can constrain the correlation time as $\tau_c < 6.6 \times 10^{-7}$ s. Figure 7.23 shows the frequency dependence of the relaxation times where the increase of

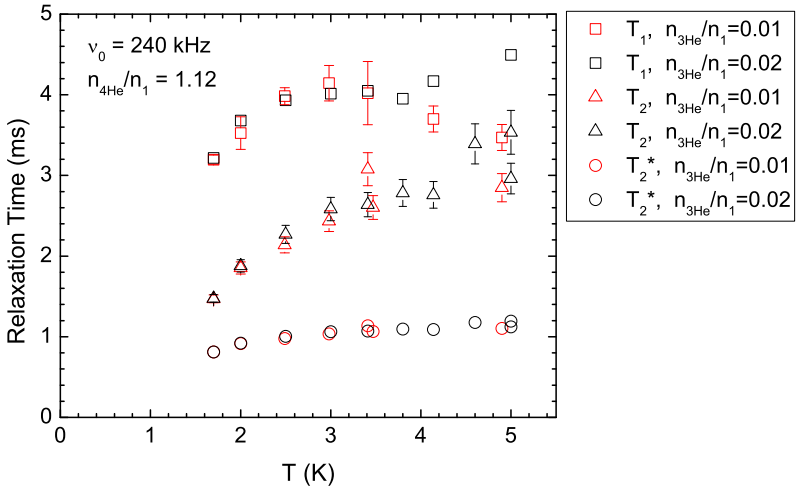

Figure 7.22: Relaxation times vs T for $n_{3He}/n_1 = 0.01$ and 0.02 at $\nu_0 = 240\,\text{kHz}$. It is believed that the change in T_1 between the coverages is due to a different relaxation mechanism dominating at high temperatures where there is a significant vapour pressure in equilibrium with the film.

T_1 with frequency suggests relaxation via 2D diffusive motion in the local magnetic fields [20]. The response to transmitter pulses was a greater problem than for the bare case due to an increase in the ringing and a decrease in signal size. It was not possible to begin data capture so close to the NMR readout pulse without changing the input range of the scope to an unacceptable level. However in general the T_2^* relaxation times were longer than in the bare case and the FID envelope was exponential making data capture close to the pulse less of an issue.

There was no resolvable change in T_2^* observed when doubling the ^{3}He coverage from $n_{3He}/n_1 = 0.01$ to 0.02. T_1 appears to increase slightly beyond the experimental error, however in this region T_1 also found to increase with increasing ^{4}He coverage. The signal magnitude increased by a factor of 2 as expected.

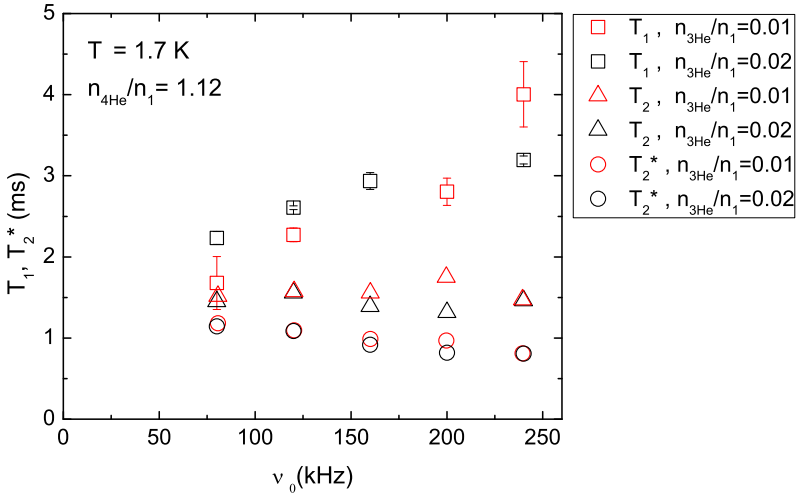

Figure 7.23: Relaxation times vs ν_0 for $n_{3He}/n_1 = 0.01$ and 0.02. The frequency dependence of T_1 suggests that relaxation is via 2D diffusive motion in the local magnetic fields

7.4.5 Relaxation as a Function of Coverage

The T_1 and T_2 relaxation times have been measured as a function of ^{4}He preplating for coverages above $n_{4He}/n = 1.117$. Between each coverage the cell was annealed at a pressure slightly above 1 mBar for an hour before slowly decreasing the temperature to 1.7 K. At the highest coverages the pressure approached 11.28 mBar, the saturated vapour pressure for bulk ^{4}He at 1.7 K and hence the cell was self annealing.

The resultant isotherm is shown in figure 7.24, where relaxation times were measured at $\nu_0 = 240$ kHz and a temperature $T = 1.7$ K. In general the T_2 relaxation time were obtained by subtracting a magnet contribution from T_2^* however at the highest coverage, $n_{4He}/n_1 = 1.84$, it was possible to observe spin echoes, described in section 7.4.2.

Increasing the ^{4}He coverage in the region $1 < n_{4He}/n_1 < 1.4$ is equivalent to making the system more compressible, which should increase the diffusion in the system,

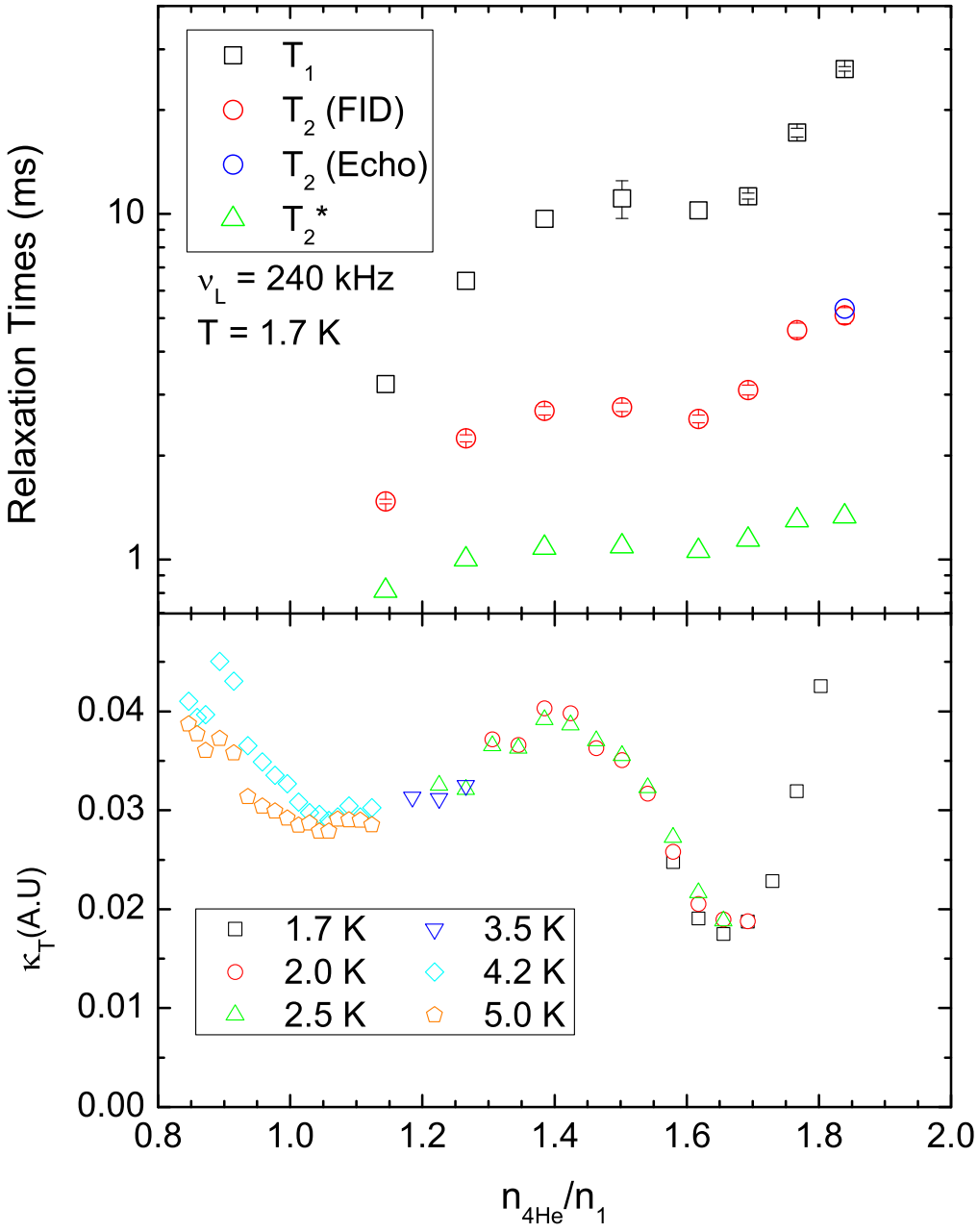

Figure 7.24: T_1, T_2 and T_2^* as a function of ^{4}He preplating coverage. Here the ^{3}He coverage was held constant at $n_{3He}/n_1 = 0.02$. At the highest coverage T_2 was obtained from the T_2^* subtracting a magnet contribution and also directly by spin echo measurement. κ_T is the isothermal compressibility

decreasing the correlation time τ_c. Here we observe both T_1 and T_2 increasing with coverage, suggesting that we are on the "fast" side of the T_1 minimum, $T_1^{(\min)}$, although no minimum was directly observable within our accessible parameter space.

For this system the second minimum in the compressibility corresponds to full pores and not to second layer completion as for 2D adsorbed systems on homogeneous planar substrates. At coverages above the second minimum at $n_{4He}/n_1 = 1.65$ the pressure rapidly approaches SVP with increasing coverage. The relaxation rates in this case have a contribution coming from relaxation on the surface of the powder grains where spins are in the gas and the vapour phases. T_1 and T_2 are also both increasing in this case however the relaxation process will be different from that at a lower coverage.

The T_1 measurements as a function of temperature for a number of coverages are shown in figure 7.25. For the lowest coverage T_1 increases with T which is as expected for the "fast" side of the $T_1^{(\min)}$ as τ_c increases with decreasing temperature. For higher coverages T_1 is increasing with T, whilst T_1 is still increasing with n_{4He}/n_1. We believe this to be due to a change in relaxation mechanism due to the existence of a finite vapour pressure. At higher temperatures T_1 values appear to be converging to a single value independent of preplating coverage. This may be due to a large fraction of the ^{3}He atoms existing in the vapour phase. This effect is briefly quantified in section 7.4.6.

The Intrinsic T_2

The echo measurements showed that T_2 increases slightly with frequency. By comparing T_2 and T_2^* the frequency dependence was found to be approximately an order

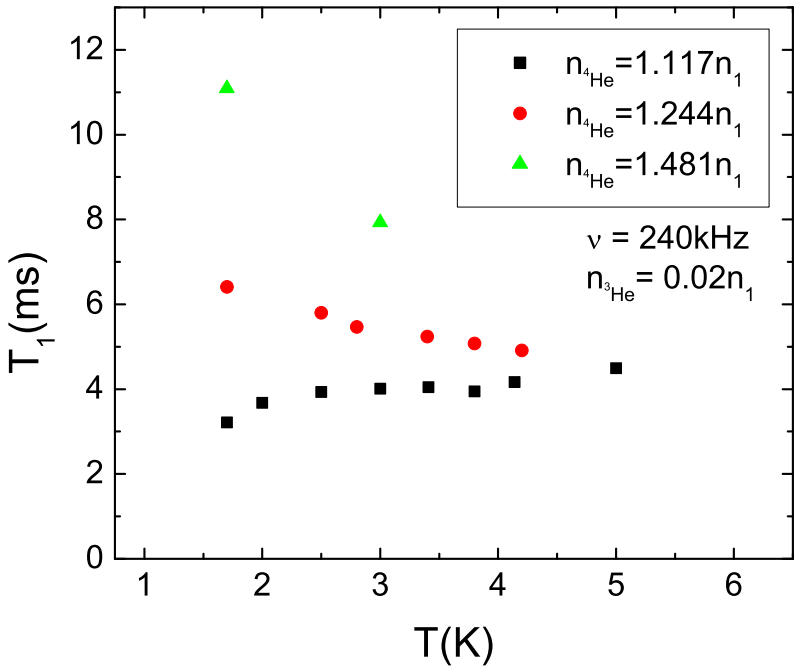

Figure 7.25: T_1 vs T for a range of n_{4He}/n_1 coverages. At low temperatures T_1 increases with coverage as the compressibility of the system increases. At the lowest coverage T_1 increases with temperature whilst at higher coverages it decreases. This is probably due to a different relaxation process becoming dominant and may be related to the finite vapour pressures observed. At the highest temperatures the relaxation times appear to be converging to a single value.

of magnitude smaller than the magnet broadening and hence this cannot be responsible for the observed reduction in the field homogeneity from the pure ^{3}He case.

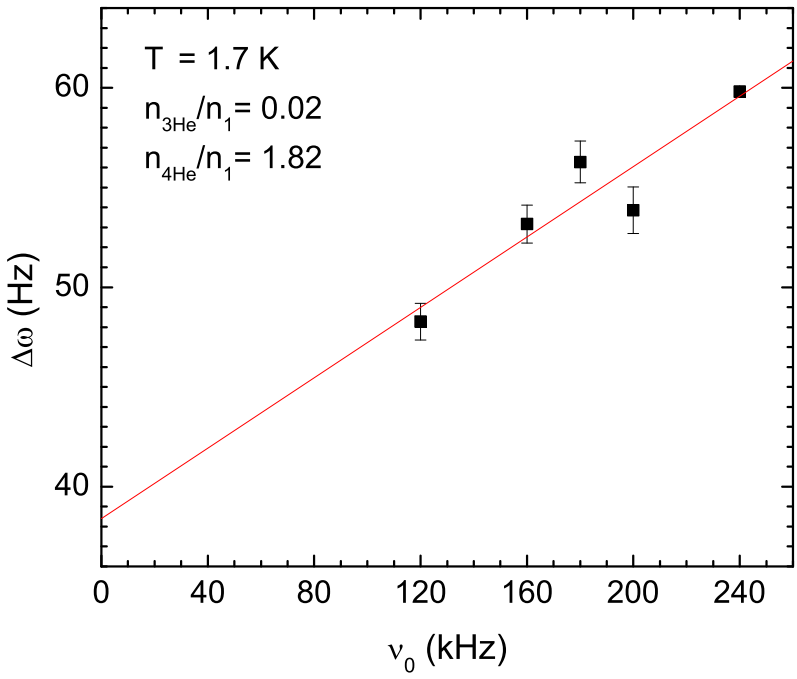

Figure 7.26: The intrinsic linewidth as a function of frequency. This appears to be proportional to frequency with a zero field intercept of $\Delta\nu = (38 \pm 4)$ Hz.

7.4.6 Effects of Finite Pressures

For the base temperature of 1.7 K a finite vapour pressure is observed for a range of coverages and temperatures, as shown in figure 6.7. For this ^{3}He-^{4}He mixture system the ^{4}He is preferentially adsorbed, and we would expect a significant amount of ^{3}He to desorb first. Due to the relatively small population of ^{3}He in this system the effect of the vapour is much stronger than in the pure ^{3}He case.

To try and better quantify this effect the temperature and size of each section of the

dead volume has been calculated. The volume is dominated by the cell and pressure gauge volumes which are at the cell temperature. Table 7.1 shows the number of atoms in the gaseous phase required for 1 mbar for a given cell temperature.

Table 7.1: Number of gaseous atoms per mBar for a given cell temperature.

T(K)	N/P(atoms/mbar)
1.7	8.0×10^{18}
3	5.0×10^{18}
4.2	3.8×10^{18}
5	3.3×10^{18}

For $n_{3He}/n_1 = 0.02$ there are 2.48×10^{19} ^{3}He spins, so that at 1.7 K a pressure of 3.1 mBar is equivalent to a number of atoms, equal to the entire ^{3}He population, being in the gaseous state. This pressure is observed for $n_{4He}/n_1 = 1.72$. For higher temperatures this occurs at lower coverages so that for our lowest ^{4}He coverage, $n_{4He}/n_1 = 1.117$, the number of gaseous atoms is equal to the number of ^{3}He spins for $T \sim 5$ K.

Figure 6.8 shows that at the highest coverage the vapour pressure is tending toward the saturated vapour pressure (SVP) of ^{4}He. However at 1.7 K the SVP is 11.28 mbar and at this pressure the number of atoms in the gaseous phase is 3.6 times larger than the number of ^{3}He in the system.

For the future low temperature experiment, the effect of the finite vapour pressure at higher temperatures will be irrelevant as at the low temperatures necessary the vapour pressure will be very small.

7.5 Summary of NMR Results

Frequency Dependence and the Magnet Homogeneity

For the pure ^{3}He case there was an insufficient separation of time scales for T_2 and T_2^* to observe spin echoes. A small frequency dependence of T_2^* was observed and attibuted to inhomogeneous broadening due to the magnet. The intrinsic contribution to the frequency dependence was assumed to be small compared with the magnet homogeneity contribution. For a future experiment a gradient coil could be added to decrease T_2^* and aid in observing spin echoes.

An increased T_2^* frequency dependence was observed for the preplated case. This was found to be independent of coverage and temperature. At the highest coverage T_2 was sufficiently long to observe spin echoes. The magnet homogeneity was derived using the measured values of T_2 and T_2^*. A small intrinsic frequency contribution to T_2 was observed, however this was an order of magnitude small than the magnet contribution. It appears that changes made to the cryostat between the two runs affected the magnet homogeneity either occuring due to a change in grounding to the overlapping shield or the addition of the pressure gauge in close proximity to the coil set. It should be noted that NMR measurements and pressure measurements were not performed simultaneously and grounding the capacitive plates of the pressure gauge made no observable difference. The NMR cell was also annealed to temperatures above the T_c of Nb in order to remove trapped flux from the overlapping shield during the run. This also did not effect the magnet homogeneity.

The frequency dependence of T_1 was observed for the preplated experiment. T_1 was found to increase with frequency on the fast side of the T_1 minimum. For a 3D

system T_1 is expected to be frequency independent in this regime. The frequency dependence is consistent with relaxation via 2D diffusive motion in the local substrate fields.

Temperature Dependence

In the pure ^{3}He case there was no independent measurement of the cell temperature, the only thermometer being the germanium mounted at the cell plate. For the preplated run at high coverages the cell pressure approached the SVP of ^{4}He. The associated temperature values obtained from using the ITS-90 temperature [21] scale agreed with the temperature measured by the germanium. It is believed that the cell was cooling to the cell plate temperature in both cases and that any observed deviation from Curie type behaviour was due to fitting errors. In both cases T_1 was observed to be changing down to the lowest temperatures.

The base temperature of the cell plate increased for the preplated measurement. This is probably due to the additional heatload and heatleak due to the pressure gauge.

Non-Exponential Decay

In general the decays observed for the pure ^{3}He experiment were non-exponential for both T_1 and for T_2^*, which is attributed to the existence of two relaxation processes affecting different parts of the system. The T_1 relaxation was fitted by a stretched exponential, and the exponential became more stretched with decreasing temperatures.

For the helium mixture experiment the relaxation rates were due to single particle effects and the relaxation was found to be exponential in all cases.

Inequality of T1 and T2

In all cases T_2 was found to be smaller than T_1, this inequality of T_1 and T_2 on the fast side of the T_1 minimum is a characteristic of 2D motion in local magnetic fields.

Coverage Isotherm

For the pure ^{3}He experiment the relaxation times were approximately constant above monolayer completion. This has been observed previously for systems of ^{3}He adsorbed on grafoil. For the preplated case the relaxation times initially increase through the second layer as the compressibility of the system increases indicating that we are on the fast side of the T_1 minimum. At higher coverages other effects become important as the number of atoms in the gaseous phase becomes comparable with the number of spins in the cell and the pores become completely filled. A future experiment capable of attaining lower temperatures would be needed to improve upon the preplating isotherm at higher coverages.

7.6 Conclusions

In the pure ^{3}He adsorbed system a weak minimum was observed in T_2 measured as a function of coverage, as is observed at monolayer completion on grafoil. This was

coincident with the first minimum in the isothermal compressibility showing that the two independent measurements of monolayer completion were in agreement.

In the measurement of relaxation times as a function of temperature the inequality of T_1 and T_2 found on the fast side of the T_1 minimum is a characteristic of diffusive 2D motion in local magnetic fields. At low temperatures T_2 is independent of temperature. In this regime the relaxation times measured are much longer than $M_2^{-1/2}$ implying significant motional narrowing of the NMR line due to quantum tunnelling.

The observed deviation from the expected Curie susceptibility suggests that we may not be sensitive all of the spins at low temperatures. This may be due to the presence of a subsystem whose magnetisation has decayed before data capture had begun. The observed magnetisation was proportional to the number of spins in all cases implying that the fraction of spins forming this subsystem would have to be proportional to coverage.

We have shown that using our sensitive detection method it is possible to observe NMR decays from extremely low ^{3}He densities in thin films consisting of isotopic helium mixtures. In the helium mixtures experiment the relaxation times were unchanged and the magnetisation increased by a factor of 2 when the number of ^{3}He spins was doubled. This suggests that spin-spin relaxation is not the dominant relaxation mechanism in this regime. The observation of a frequency dependence of T_1 on the fast side of the T_1 minimum indicates relaxation via 2D diffusive motion in the local substrate fields.

The change in sign of the temperature dependence of T_1 with increasing ^{4}He cov-

erage, shown in figure 7.25, is not fully understood. Here T_1 is found to increase with temperature for preplating a little over monolayer, where for slightly higher preplating coverages it decreases with temperature. This could be explained by a change in the correlation time such that we have crossed a T_1 minimum, however for this to be the case we would also expect the dependence of T_1 on preplating coverage to change and this was not observed. Another possibility is that the relaxation for the lower preplating coverages is dominated at low temperatures by relaxation sites on the substrate, where ^{4}He is preferentially adsorbed to these sites as the coverage is increased. At higher temperatures this data is suggestive that T_1 may be approaching a single temperature independent T_1 value. This may be due to a change in relaxation mechanism due to the presence finite vapour pressures in the cell.

The observed magnetisation and relaxation times suggest that a further experiment at lower temperatures involving a smaller surface area should be possible. In general T_2^* was long compared to the recovery time of the spectrometer following an NMR readout pulse, so that the signal had not decayed by a significant amount before data capture could begin. Also the T_1 relaxation rate is short enough that the repeat rate for averaging should be determined by the thermal recovery of the system and not the longitudinal recovery of the magnetisation.

Chapter 8

Summary of Achievements and Future Work

8.1 Summary of Achievements

A system has been developed to perform high sensitivity nuclear magnetic resonance and pressure measurements and characterisation of ^{3}He adsorbed in the mesopores of MCM-41 zeolite.

The low temperature pressure gauge is sensitive to μbar pressure changes allowing detailed pressure and compressibilty measurements without thermomolecular pressure effects.

Compressibility data shows that the measured pore sizes are consistent with work previously published, for example see reference [7].

The pulsed NMR spectrometer system is capable of applying a range of high precision coherent NMR pulses with different pulse lengths. The discrete nature of the pulse creation prevents any feed-though at the Larmor frequency, as can happen in conventional systems.

The sensitivity of the NMR detection method allows measurements of extremely low spin densities up to relatively high temperatures.

Two independent measures of monolayer completion and full pores have been shown to be valid for this system in the isothermal compressibility and the observed minima in the T_2 relaxation time.

The inequality of T_1 and T_2 on the fast side of the T_1 minimum and frequency dependence of T_1 in the preplated experiment suggest 2D motion.

8.2 Considerations for Continuation of the Experiment

1D systems are typified by power law rather than exponential behaviour. It would therefore be advantageous to be able to cover a large range of parameter space so that powers can be determined accurately. We are limited in temperature by how low a substrate temperature we can achieve, and by how far we can drive up the dimensional crossover temperature by varying the ^{3}He and ^{4}He coverages. The range of Larmor frequencies is determined by the static field NMR magnet, where the maximum field is determined by the field-current ratio and the critical current. Increasing the number of layers on the magnet will increase the field-current ratio of

the magnet but decrease the field homogeneity. As the critical current of the magnet circuit is determined by the critical current of the superconducting spot welds it may be advantageous to have the spot welds in the helium bath. A static gradient coil may be added to decrease T_2^* and facilitate the observation of spin echoes.

It would be interesting to vary the line density of ^{3}He to explore the strong and weak coupling limits. In 1D the coupling becomes stronger as the interparticle spacing increases, however this also decreases the number of spins per pore and may make finite size effects more important. We expect larger magnetic susceptibilities with smaller coverages in 1D due to the n_{1D} dependence of $T_F^{(1D)}$.

We would preferably be able to observe an NMR signal from 1/100 monolayer under the stringent conditions of $\nu_0 = 100\,\mathrm{kHz}$ at 200 mK. This should realistically allow us to cover a decade in frequency and perform experiments above and below the dimensional crossover. It is important that the system is cooled to as low a temperature as possible, although the accessible base temperature will be dependent on how effectively the substrate can be cooled. Building a magnet with a higher field-current ratio should allow us to perform NMR at 1 MHz

We have experienced regimes where $1/T_2^* \approx 1/T_2$ and $1/T_2 \gg 1/T_2^*$. In the first case it is appropriate to measure T_2^* in the frequency domain from $90° -$ FID and subtracting a magnet contribution. For the second case it is possible to observe T_2 directly using a $90° - \tau - 180° - \tau -$ echo pulse sequence. It is important to consider the signal-to-noise implications of both of these regimes when designing an experimental cell to continue this experiment to the lower temperatures needed to observe a dimensional crossover from 2D to 1D.

At the lowest temperatures measured for the pure case a temperature independent quantum tunnelling regime was observed with T_2 of a few hundreds of microseconds. We expect relaxation times of this order to continue to millikelvin temperatures.

Some initial fabrication for the low temperature cell has begun. A new coil set is partly machined. The outer superconducting shield, magnet former and transmitter former have been fabricated to the same design as the present coilset, and it is this new coil set which is shown in figure 4.7(f). The cell plate is designed to be compatible with an existing dilution refrigerator with a base temperature 20 mK. A new pressure gauge has also been constructed and is ready calibrate.

8.2.1 Signal-to-Noise

The expected signal flux coupled to the SQUID is given by equation 7.4 as

$$\phi_{SQ} = \frac{M_{\mathrm{i}}}{(L_{\mathrm{i}} + L_{\mathrm{r}})} \frac{\hbar^2 \gamma B_{1,\mathrm{c}} \kappa}{4 k_{\mathrm{B}}} \frac{N_{\mathrm{V}} \omega_0}{T}$$

which can be used in considering the signal size of a future cell designed to be coolable to lower temperatures. In the time domain the SNR is simply $\phi_{\mathrm{SQ}}/\phi_{\mathrm{N}}$. In the frequency domain the SNR is frequently defined as the ratio of peak signal to peak noise, and is given by

$$\left(\frac{S_{\mathrm{p}}}{N_{\mathrm{p}}}\right) = \frac{A}{K_{\mathrm{N}}^{\mathrm{f}}} \sqrt{\frac{T_2^*}{2 K_{\mathrm{T}} < P_{\mathrm{N}>}}} \tag{8.1}$$

where $K_{\mathrm{N}}^{\mathrm{f}}$ is a constant factor relating the peak to the RMS noise and is taken to be 2.5 and $K_{\mathrm{T}} T_2^* = t_{\mathrm{cap}}$ is the capture time. We need $K_{\mathrm{T}} \geq 5$ to avoid distorting

the NMR line.

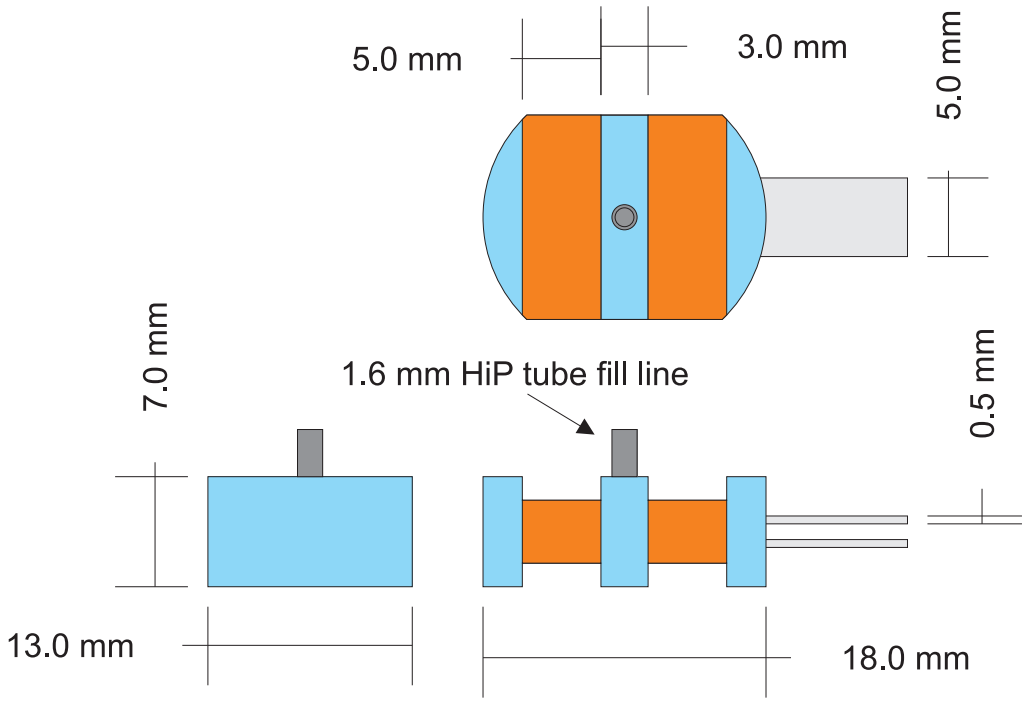

Figure 8.1: A possible cell design for a future experiment designed to be coolable to low temperatures. This geometry is based on the cell described in [68]

For the remainder of the chapter in considering the possible signal-to-noise of a future experiment I will focus on one particular cell design used previously for superfluid thin film experiments described in the thesis of H. Dyball [68]. This cell was designed in a coin geometry from two Stycast 1266 halves, silver plates were mounted at the top and bottom of the cell to aid the heat transfer. The receiver coil is wound directly onto the cell in a split solenoidal geometry, consisting of two superconducting coils of 5 mm length with a 3 mm gap for the fill line to exit.

This cell design offers an increased coupling to the sample spins due to the geometry of the receiver coil although this may cause practical problems in sample preparation as the receiver coil will have to be wound after the sample substrate is loaded in the

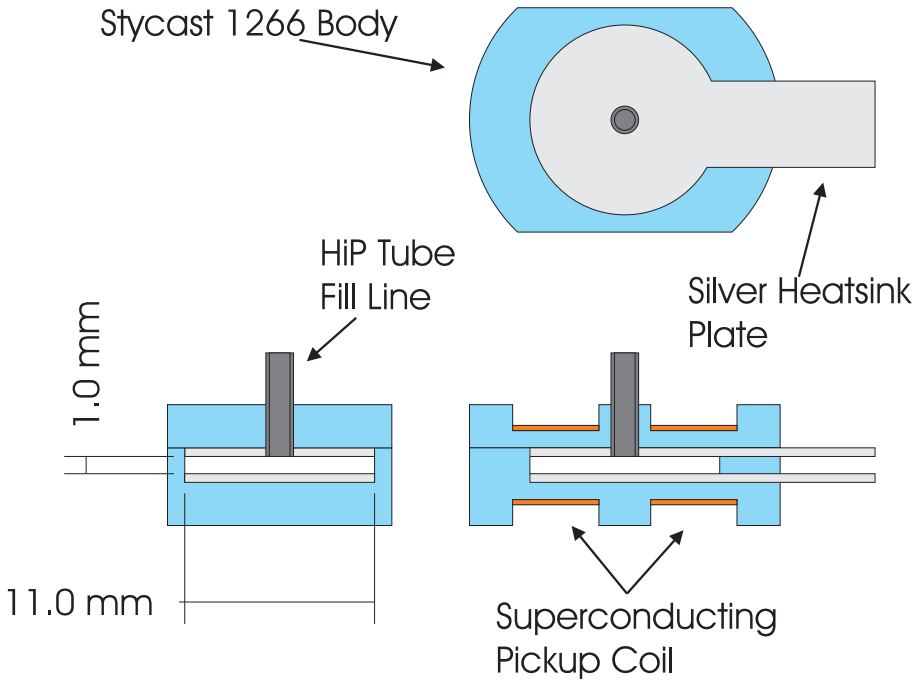

Figure 8.2: A Cut Through of the cell shown in figure 8.1

cell.

Upgrading the DC SQUID

The C5 SQUID used for the preplated experiment is similar to the front end of a 2-stage SQUID also developed by PTB [49]. Here the first stage acts in the same way as our SQUID and is coolable. A 2-stage SQUID device mounted at 700 mK heat sunk to the still of a dilution unit is described in the thesis of A. Shibahara [69]. This has a coupled energy sensitivity $\varepsilon_c \sim 8\,\mathrm{h}$. The flux noise is reduced compared to the SQUID described in this thesis, and the second stage is used amplify the signal and the noise such that the SQUID noise remains the dominant noise source. Operating a 2-stage SQUID necessitates changing from Magnicon SEL-1 electronics to their XXF electronics. This also includes a lower noise amplifier to take advantage of the

lower flux noise of the SQUID.

As the front end of the two SQUID's are similar M_{i} and L_{i} are the same. The averaging time needed for a given SNR is proportion to ε_{c}, so changing to this generation of SQUID would reduce the averaging time by $29.3/8 = 3.7$ or alternatively a reduction in the intrinsic flux noise of 1.92. The SQUID noise is presently not improved by cooling to lower temperatures for a number of technical reasons.

Field-Current Ratio for the Receiver Coil

The receiver coil used for the experiments described in this thesis was designed to provide easy loading access for the sample cell at the expense of optimum coupling of flux. This would be improved by adopting a receiver coil with broken solenoidal geometry described in [68]. For optimum flux coupled to the SQUID by the flux transformer we need to match the inductances of the receiver coil and the SQUID. The C5 SQUID used in the preplated experiment had $L_{\mathrm{i}} = 1.8\,\mu\mathrm{H}$ and the measured inductance of the receiver coil was $2.16\,\mu\mathrm{H}$ and had a theoretical field current ratio of $(B/I)^{\mathrm{th}} = 384\,\mu\mathrm{T/A}$. The Dyball cell had $2\,\mu\mathrm{H}$ and had an increased field current ratio of $(B/I)^{\mathrm{th}} = 1.933\,\mathrm{mT\,A^{-1}}$ offering a possible improvement factor of 5.0 .

Decreased Sample Volume

To provide adequate cooling we wish to minimise the maximum distance from the substrate to the silver heat sink plates. The cell must fit inside the self-contained NMR coil set. The bore of the transmitter coil is 20 mm and to avoid coupling acoustic resonances to the receiver during transmitter pulse there must be a physical

separation from the transmitter coil, and hence the maximum diameter for the cell is $\sim 18\,\mathrm{mm}$. The cell in figure 8.2 has a 11 mm diameter and is 1 mm in height. This gives a sample volume of $0.095\,\mathrm{cm}^3$, which is a factor of 12 smaller than the current cell.

New Magnet

To increase the experimental range we would like to increase the accessible frequency range to $\sim 1\,\mathrm{MHz}$. This would be possible using the existing magnet former by adding additional layers to the magnet. As the proximity of the magnet former is close to the superconducting shield subsequent layers would have a diminished contribution to the field-current ratio. This would decrease the homogeneity of the magnet and the magnet contribution to the linewidth must be considered before finalising a magnet design. In particular in the case that the transverse relaxation is dominated by the magnet the T_2^* relaxation time must be considered in terms of signal-to-noise in the frequency domain and suitability for spin echo measurements.

8.3 Future Cell Summary

Considering the factors of the previous section for a given spin density, temperature and Larmor frequency the initial signal magnitude A_0 would decrease by a factor of 2.4 compared to the present setup. However it would increase by a factor of ~ 3.5 by cooling to 200 mK compared to the present base temperature of 1.7 K. If it were possible to cool the sample to 50 mK at $\nu_0 = 1\,\mathrm{MHz}$ this increases to ~ 140 times larger than the present signal for $\nu_0 = 240\,\mathrm{kHz}$.

Bibliography

[1] T. Bergeman, M. G. Moore, and M. Olshanii. Atom-atom scattering under cylindrical harmonic confinement: Numerical and analytic studies of the confinement induced resonance. *Phys. Rev. Lett.*, 91(16):163201, 2003.

[2] M. Hilke, D. C. Tsui, M. Grayson, L. N. Pfeiffer, and K. W. West. Fermi liquid to Luttinger liquid transition at the edge of a two-dimensional electron gas. *Phys. Rev. Lett.*, 87(18):186806, 2001.

[3] O. M. Auslaender, H. Steinberg, A. Yacoby, Y. Tserkovnyak, B. I. Halperin, K. W. Baldwin, L. N. Pfeiffer, and K. W. West. Spin-charge separation and localization in one dimension. *Science*, 308(5718):88–92, 2005.

[4] Junko Taniguchi, Akira Yamaguchi, Hidehiko Ishimoto, Hiroki Ikegami, Taku Matsushita, Nobuo Wada, Silvina M. Gatica, Milton W. Cole, Francesco Ancilotto, Shinji Inagaki, and Yoshiaki Fukushima. Possible one-dimensional ^{3}He quantum fluid formed in nanopores. *Phys. Rev. Lett.*, 94(6):065301, 2005.

[5] Yuki Matsushita, Junko Taniguchi, Akira Yamaguchi, Hidehiko Ishimoto, Hiroki Ikegami, Taku Matsushita, Nobuo Wada, Silvina M. Gatica, Milton W. Cole, and Francesco Ancilotto. Dimensional-crossover of ^{3}He gas formed in one-dimensional nanometer tunnel. *J. Low Temp. Phys.*, 138(1):211–216, 2005.

[6] Hiroki Ikegami, Yoji Yamato, Tomohisa Okuno, Junko Taniguchi, Nobuo Wada, Shinji Inagaki, and Yoshiaki Fukushima. Superfluidity of ^{4}He in nanosize channels. *Phys. Rev. B*, 76(14):144503, 2007.

[7] Hiroki Ikegami, Tomohisa Okuno, Yoji Yamato, Junko Taniguchi, Nobuo Wada, Shinji Inagaki, and Yoshiaki Fukushima. Film growth of ^{4}He adsorbed in mesopores. *Phys. Rev. B*, 68(9):092501, 2003.

[8] Ryo Toda, Mitsunori Hieda, Taku Matsushita, Nobuo Wada, Junko Taniguchi, Hiroki Ikegami, Shinji Inagaki, and Yoshiaki Fukushima. Superfluidity of ^{4}He in one and three dimensions realized in nanopores. *Phys. Rev. Lett.*, 99(25):255301, 2007.

[9] J. Taniguchi, A. Yamaguchi, H. Ishimoto, H. Ikegami, and N. Wada. Influence of ^{4}He preplating on ^{3}He fluid formed in one-dimensional 28Å pores. *J. Low Temp. Phys.*, 138(1):165–170, 2005.

[10] Ryo Toda, Junko Taniguchi, Ryota Asano, Taku Matsushita, and Nobuo Wada. Adsorption potentials and film growths of ^{4}He in nanometer pores of FSM-16 (2.8 nm) and HMM-2 (2.7 nm). *J. Low Temp. Phys.*, 138(1):177–182, 2005.

[11] Nobuo Wada, Taku Matsushita, Mitsunori Hieda, and Ryo Toda. Fluid states of helium adsorbed in nanopores. *J. Low Temp. Phys.*, 157(3):324–351, 2009-11-01.

[12] J. S. Beck, J. C. Vartuli, W. J. Roth, M. E. Leonowicz, C. T. Kresge, K. D. Schmitt, C. T. W. Chu, D. H. Olson, and E. W. Sheppard. A new family of mesoporous molecular sieves prepared with liquid crystal templates. *JACS*, 114(27):10834–10843, 1992.

[13] C. T. Kresge, M. E. Leonowicz, W. J. Roth, J. C. Vartuli, and J. S. Beck. Ordered mesoporous molecular sieves synthesized by a liquid-crystal template mechanism. *Nature*, 359(6397):710–712, 1992.

[14] K. S. W Sing, D. H Everett, R. A. W Haul, L. Moscou, R. A. Pierotti, J. Rouquerol, and T. Siemieniewska. Reporting physisorption data for gas/solid systems with special reference to the determination of surface area and porosity. *Pure Appl. Chem*, 57(4):603–619, 1985.

[15] George Stan and Milton W. Cole. Low coverage adsorption in cylindrical pores. *Surf. Sci.*, 395(2-3):280–291, 1998.

[16] M. Boninsegni. Thin helium film on a glass substrate. *J. Low Temp. Phys.*, 159(3):441–451, 2010.

[17] E. Cheng and M.W. Cole. Retardation and many-body effects in multilayer-film adsorption. *Phys. Rev. B*, 38(2):987–995, 1988.

[18] A. Abragam. *Principles of Nuclear Magnetism*. International Series of Monographs on Physics. Oxford University Press, USA, reprint edition, 1983.

[19] Charles P. Slichter. *Principles of Magnetic Resonance*. Springer-Verlag, Berlin ; New York :, 3rd enl. and updated ed. edition, 1990.

[20] B.P Cowan. *Nuclear Magnetic Resonance and Relaxation*. Cambridge University Press, 1997.

[21] R.L. Rusby. The international temperature scale of 1990 at low temperatures. *Physica B: Condensed Matter*, 165-166(Part 1):35–36, 1990.

[22] High Pressure Equipment Company, P.O. Box 8248, 1222 Linden, Erie, Pennsylvania 16505, United States - `http://www.highpressure.com`.

[23] Swagelok Company, 29500 Solon Rd., Solon, OH, 44139-2764 United States - http://www.swagelok.com.

[24] Hoke, 405 Centura Court, Spartanburg, SC 29303, United States - http://www.Hoke.com.

[25] Pfeiffer Vacuum GmbH, Berliner Strasse 43, 35614 Asslar, Germany - http://www.Pfeiffer-vacuum.com.

[26] J.B. Condon. *Surface area and porosity determinations by physisorption: Measurements and theory.* Elsevier Science Ltd, 2006.

[27] GC Straty and ED Adams. Highly sensitive capacitive pressure gauge. *Rev. Sci. Inst.*, 40:1393, 1969.

[28] J.S. Souris and T.T. Tommila. *Experimental Techniques in Condensed Matter Physics at Low Temperatures*, chapter 4.7 Pressure Measurements, pages 245–266. Addison-Wesley, 1998.

[29] Dow Corning Corporation, Corporate Center, PO Box 994, Midland MI 48686-0994, United States - http://www.dowcorning.com.

[30] Apeizon, Hibernia Way, Trafford Park, Manchester, M32 0ZD, UK - http://www.apiezon.com.

[31] Cambridge Magnetic Refrigeration Ltd, Britannia House, 19-21 Godesdone Rd, Cambridge, CB5 8HR - www.cmr.uk.com.

[32] Andeen-Hagerling, 31200 Bainbridge Road , Cleveland, Ohio 44139-2231 U.S.A. - www.andeen-hagerling.com/ah2550a.htm.

[33] Paroscientific, 4500 148th Ave., N.E. Redmond, WA, 98052, United States - http://www.paroscientific.com.

[34] T.R. Roberts and S.G. Sydoriak. Thermomolecular pressure ratios for ^{3}He and ^{4}He. *Phys. Rev.*, 102(2):304–308, 1956.

[35] C.P. Lusher, J. Li, M.E. Digby, R.P. Reed, B. Cowan, J. Saunders, D. Drung, and T. Schurig. Broadband nuclear magnetic resonance using DC SQUID amplifiers. *IEEE trans. Appl. Supercon.*, 6(10-12):591–601, 1999.

[36] D. Drung, C. Assmann, J. Beyer, M. Peters, F. Ruede, and T. Schurig. DC SQUID readout electronics with up to 100 MHz closed-loop bandwidth. *IEEE trans. Appl. Supercon.*, 15:777–780, 2005.

[37] Magnicon GmbH, Lemsahler Landstr. 171, 22397 Hamburg, Germany http://www.magnicon.com/squid-electronics/sel-1/.

[38] Computer program: modified by Michael Boegl, Experimental Physics 5, University of Bayreuth, Germany, based on original program from Helsinki University, Finland.

[39] G.K. White. *Experimental Techniques in Low Temperature Physics*, chapter Vacuum Techniques and Materials, page 327. Oxford University Press, 1968.

[40] D. Hechtfischer. Generation of homogeneous magnetic fields within closed superconductive shields. *Cryogenics*, 27(9):503–504, 1987.

[41] R.J. Köerber. *Low Field DC SQUID Nuclear Magnetic Resonance on single crystal* UPT_3. PhD thesis, Royal Holloway, University of London, 2005.

[42] D. I. Hoult and R. E. Richards. The signal-to-noise ratio of the nuclear magnetic resonance experiment. *J. Magn. Reson.*, 24(1):71–85, 1976.

[43] F.W. Grover. *Inductance calculations: working formulas and tables.* Dover Pubns, 1962.

[44] Whatman - `www.whatman.com/GlassMicrofiberBinderFree.aspx`.

[45] D. Drung. Advanced SQUID read-out electronics. In H. Weinstock, editor, *SQUID Sensors: Fundamentals, Fabrication and Applications*, pages 63–116. Kluwer Academic Publishers, Dordrecht, 1996.

[46] J.C. Gallop. *SQUIDs, the Josephson Effects and Superconducting Electronics.* Adam Hilger, 1991.

[47] J. Clark and A.I. Braginski, editors. *The SQUID Handbook, Vol. 1, Fundamentals and technology of SQUIDs and SQUID systems.* Wiley-VHC, Weinheim, 2004.

[48] J. Clarke. Superconducing electronics. In H Weinstock and M pp. 87148. Nisenoff, editors, *SQUID Concepts and Systems*, number 59 in NATO ASI Series. Springer, Berlin/Heidelberg, 1989.

[49] D. Drung, C. Assmann, J. Beyer, A. Kirste, M. Peters, F. Ruede, and T. Schurig. Highly sensitive and easy-to-use SQUID sensors. *IEEE trans. Appl. Supercon.*, 17:699–704, 2007.

[50] M.H.W. Chan. Private communication providing sample characterisation of the BC1 and BC2 MCM-41 samples characterised by N_2 isotherm and XRD.

[51] M. Bretz, J. G. Dash, D. C. Hickernell, E. O. McLean, and O. E. Vilches. Phases of ^{3}He and ^{4}He monolayer films adsorbed on basal-plane oriented graphite. *Phys. Rev. A*, 8(3):1589–1615, 1973.

[52] G. Zimmerli, G. Mistura, and M. H. W. Chan. Third-sound study of a layered superfluid film. *Phys. Rev. Lett.*, 68(1):60–63, 1992.

[53] P. A. Crowell and J. D. Reppy. Superfluidity and film structure in ^{4}He adsorbed on graphite. *Phys. Rev. B*, 53(5):2701–2718, 1996.

[54] J. G. Dash. *Films on Solid Surfaces*. Academic, New York, 1975.

[55] P. Selvam, S.K. Bhatia, and C.G. Sonwane. Recent advances in processing and characterization of periodic mesoporous MCM-41 silicate molecular sieves. *Ind. Eng. Chem. Res*, 40(15):3237–3261, 2001.

[56] S Brunauer, P. H. Emmett, and E Teller. Adsorption of gases in multimolecular layers. *JACS*, 60(2):309–319, 1938.

[57] Mietek Jaroniec, Michal Kruk, James P. Oliver, and Stefan Koch. A new method for the accurate pore size analysis of MCM-41 and other silica based mesoporous materials. In G. Kreysa K.K. Unger and J.P. Baselt, editors, *Characterisation of Porous Solids V, Proceedings of the 5th International Symposium on the Characterisation of Porous Solids (COPS-V)*, volume 128, pages 71–80. Elsevier, 2000.

[58] Elliott P. Barrett, Leslie G. Joyner, and Paul P. Halenda. The determination of pore volume and area distributions in porous substances. I. Computations from nitrogen isotherms. *JACS*, 73(1):373–380, 1951.

[59] R Feile, H. Wiechert, and H.-J. Lauter. Neutron scattering study of melting of ^{3}He surface layers. *Phys. Rev. B*, 25(5):3410–3412, 1982.

[60] M. Boninsegni, N. V. Prokof'ev, and B. V. Svistunov. Worm algorithm and diagrammatic monte carlo: A new approach to continuous-space path integral monte carlo simulations. *Phys. Rev. E*, 74(3):036701, 2006.

[61] P Horowitz and W Hill. *The Art of Electronics*. University Press, 1989.

[62] J.C. Lindon and A.G. Ferrige. Digitisation and data processing in Fourier transform NMR. *Prog. Nucl. Magn. Reson. Spectrosc.*, 14:27–66, 1980.

[63] J.R. Owers-Bradley. *The Properties of Helium Adsorbed on Graphite: An NMR Study*. PhD thesis, University of Sussex, 1978.

[64] C. P. Lusher, J. Nyèki, Dm. Shvarts, B. P. Cowan, J. Saunders, and D. E. W. Vaughan. NMR study of ^{3}He adsorbed in zeolite pores. *J. Low Temp. Phys.*, 134(1):619–624–624, 2004.

[65] M.G. Richards. In j. Ruvalds J.G. Dash, editor, *Phase Transitions in Surface Films*, volume 51 of *NATO Advanced Study Institute Series B*, page 165. Plenum, 1980.

[66] M. Bretz, G. B. Huff, and J. G. Dash. Solid phase of ^{4}He monolayers: Debye temperatures and "melting" anomalies. *Phys. Rev. Lett.*, 28(12):729–731, 1972.

[67] Kōzō Satoh and Tadashi Sugawara. Pulsed NMR study of submonolayer and multilayer ^{3}He films adsorbed on grafoil. *Journal of Low Temperature Physics*, 38:37–77, 1980.

[68] H. Dyball. *A Study of* ^{3}He *Films Using SQUID NMR*. PhD thesis, Royal Holloway, University of London, 2001.

[69] A Shibahara. *Low Field DC SQUID NMR on Room Temperature Samples and Single Crystal* UPt_3. PhD thesis, Royal Holloway, University of London, 2010.